Adaptive Transmission and Distribution Modeling and Simulation Tools for Supporting Integration and Operation of High Penetration of DERs

Final Project Report

S-107

Power Systems Engineering Research Center

Empowering Minds to Engineer
the Future Electric Energy System

Adaptive Transmission and Distribution Modeling and Simulation Tools for Supporting Integration and Operation of High Penetration of DERs

Final Project Report

Project Team

Qiuhua Huang, Project Leader
Colorado School of Mines

Venkataramana Ajjarapu
Iowa State University

Meng Wu
Arizona State University

Graduate Students

Owen Cornmesser
Colorado School of Mines

Aditya Shankar Kar
Iowa State University

Zeming Zhou
Arizona State University

PSERC Publication 25-06

December 2025

For information about this project, contact:

Qiuhua Huang
Colorado School of Mines
Electrical Engineering Department
1500 Illinois St., Golden, CO 80401
Phone: 303-273-3960
Email: qiuhuahuang@mines.edu

Power Systems Engineering Research Center

The Power Systems Engineering Research Center (PSERC) is a multi-university Center conducting research on challenges facing the electric power industry and educating the next generation of power engineers. More information about PSERC can be found at the Center's website: http://www.pserc.org.

For additional information, contact:

Power Systems Engineering Research Center
Arizona State University
527 Engineering Research Center
Tempe, Arizona 85287-5706
Phone: 480-965-1643
Fax: 480-727-2052

Notice Concerning Copyright Material

PSERC members are given permission to copy without fee all or part of this publication for internal use if appropriate attribution is given to this document as the source material. This report is available for downloading from the PSERC website.

©2025 Colorado School of Mines. All rights reserved.

Acknowledgments

We acknowledge the technical feedback from project advisors.

Executive Summary

This project is motivated by the growing integration of utility-scale and distributed energy storage resources (DER) in both transmission and distribution (T&D) systems. As the implementation of FERC Order 2222 is coming and DER proliferate, it is imperative to adequately model and efficiently analyze the dynamic impacts of DER on T&D systems, capture and leverage full capabilities of DER to facilitate large-scale DER integration and T&D system operation. Integrated T&D modeling and co-simulation tools have been developed by reusing existing simulators. One fundamental issue is that existing transmission and distribution system simulation tools are modeling-fidelity-agnostic, i.e., they solve dynamic simulation problems with all the details in the input system models regardless of system conditions and contingencies. As a result, they are computationally inefficient and inadequate to deal with complex, large-scale T&D systems, and engineers must manually perform model reduction or simplification for almost every study, which is ad-hoc, time-consuming and error-prone. All these contribute to renewable integration queue backlog problems in many independent system operators (ISOs) and utilities.

Our project goals are 1) to help ISOs and utilities address these issues by transforming the model reduction and selection from a manual, ad-hoc and out-of-simulation-loop process into a systematic, automated, and AI-enhanced process within a suite of new T&D modeling and simulation tools; and 2) to help the industry tap into the var flexibility offered by DERs to enhance T&D system voltage stability as well as renewable integration.

To achieve the goals above, this project develops an adaptive, multi-fidelity and AI-accelerated T&D co-simulation tool to improve the computational efficiency of dynamic simulation for large-scale T&D systems, and make transient stability simulation and dynamic contingency analysis of large-scale T&D systems on laptops and servers feasible and practical. The research is presented in four chapters (Chapters 2-5).

Chapter 2 — Aggregate DER Reactive-Power Capability Curve: Develops a TSO–DSO framework that aggregates feeder-level inverter VAR flexibility via D-OPF, feeds it to a T-OPF during contingencies, then dispatches VAR setpoints back to effective DERs; in the 9-bus/37-node tests this keeps voltages within limits under generator and line outages and reduces feeder reactive losses from 3.94 to 3.69 MVAr with sensitivity-aware dispatch.

Chapter 3 — Data-Driven and LLM-Assisted Distribution Modeling: Identifies reduced-order, globally linear dynamics from partial POI measurements using delay embeddings and DMD

(Koopman-style), accurately reconstructing responses even with FIDVR; also introduces a fine-tuned LLM assistant for PSCAD Python automation (mitigating hallucinated APIs) and a "Grid-Scout" field-to-model pipeline (Flutter app + AWS/MySQL) that updates OpenDSS models from QR/GPS-tagged equipment data.

Chapter 4 — Screening for T&D Multi-Fidelity Modeling: Shows that short-circuit analysis provides an accurate and generally conservative estimator of minimum voltage during three-phase faults—robust to aggregation, DER penetration, and dynamic loads—validated on IEEE-9 and -300 systems and in T&D co-simulation; this supports fast identification of where detailed distribution models are actually needed.

Chapter 5 — Automated & Adaptive Distribution Modeling for Contingency Analysis: Automates case building by thresholding short-circuit voltages to "high-impact" regions (disaggregate there, aggregate elsewhere), achieving more than 4 times lower runtime than fully disaggregated simulation while cutting average RMSE by 10 times and max voltage error by more than five times versus a fully aggregated model; it also analyzes accuracy–runtime tradeoffs as the voltage threshold varies.

Project Publications

[1] A. Alkhonain, A. Singhal, A. K. Bharati, and V. Ajjarapu, "Sensitivity-aware reactive power dispatch of DERs to support transmission grid during emergency," in 2023 North American Power Symposium (NAPS), 2023, pp. 1–6.

[2] A. S. Kar, K. K. Challa, A. K. Bharati, A. Singhal, and V. Ajjarapu, "Robust VAR Capability curve of DER with Uncertain Renewable Generation," accepted, IEEE Power and Energy Society General Meeting (PESGM), Seattle, 2024

[3] O. Cornmesser and Q. Huang, "Identification of Impact Regions for Adaptive Distribution System Modeling in Transmission-Level Dynamic Contingency Analysis," accepted and presented at CIGRE Grid of the Future Symposium, Raleigh, NC, Nov. 2024

[4] Gareth Calkins, Carlos Desio, Musheer Gorani, J. Scott McCain, Seth Palkki, Jose Manuel G. Dolot, and Meng Wu, "Undergraduate Research on A Smart Field Data Collection and Model Updating Tool for Distribution Power Systems," *57th North American Power Symposium (NAPS)*, Hartford, CT, USA, Oct 2025.

[5] A. S. Kar, K. K. Challa, A. K. Bharati, and V. Ajjarapu, "Harnessing Flexibility of Distribution System With Uncertain Loads and DERs," submitted to IEEE trans. on power system, Dec, 2024.

[6] O. Cornmesser and Q. Huang, “Contingency-aware multi-fidelity modeling and simulation for dynamic contingency analysis under high penetration of distributed energy resources”, under preparation.

Student Theses:

[1] Owen Cornmesser, “Adaptive transmission and distribution dynamic contingency analysis with high penetrations of distributed energy resources.” Master thesis, Colorado School of Mines, Golden, Colorado, May, 2025 .

Industry Advisors

Panitarn (Joseph) Chongfuangprinya	Hitachi America Ltd.
Bo Gong	Salt River Project
Mingguo Hong	ISO New England
Akshay Korad	Midcontinent Independent System Operator
Weijia Liu	National Renewable Energy Laboratory
Zhongxia Zhang	Dominion Energy
Parag Mitra	Electric Power Research Institute
Deepak Ramasubramanian	Electric Power Research Institute
Evangelos Farantatos	Electric Power Research Institute
Alberto Del Rosso	Electric Power Research Institute
Harvey Scribner	Southern Power Pool
Mohit Singh	ComEd
Sid Suryanarayanan	Eaton

Table of Contents

1. Introduction 1
   - 1.1 Motivation 1
   - 1.2 Background 1
     - 1.2.1 Power System Dynamic Simulation 2
     - 1.2.2 Dynamic Contingency Analysis 3
     - 1.2.3 Short-Circuit Analysis 3
     - 1.2.4 Distributed Energy Resources and Dynamic Load Coupling With Voltage 5
   - 1.3 Project outcomes 6
     - 1.3.1 Aggregrate DER reactive power capability curve 6
     - 1.3.2 Data-driven and LLM-assisted dynamic modeling approaches for deep-DER-penetrated distribution systems 7
     - 1.3.3 short-circuit-based screening method for automated, multi-fidelity modeling 8
     - 1.3.4 Automated, multi-fidelity T&D dynamic simulation engine and case study 9
     - 1.3.5 T&D test cases 9
   - 1.4 Report Organization 10

2. Aggregate DER Reactive Power Capability curve 11
   - 2.1 Objective & Introduction 11
   - 2.2 Framework 11
   - 2.3 Estimation of aggregated reactive power capability 12
     - 2.3.1 Description of inverter limits 12
     - 2.3.2 Linear model of D-system 12
     - 2.3.3 DSO-OPF for reactive power capability calculation (DSO-1) 14
   - 2.4 TSO OPF 15
   - 2.5 Reactive power set point dispatch for participating DERS (DSO-2) 15
   - 2.6 Test case & results 16
   - 2.7 Key takeaways and future work 20

3. Data-driven and Large-Language-Model-Assisted Modeling Approaches for Deep-DER-Penetrated Distribution Systems 22
   - 3.1 Introduction 22
   - 3.2 Data-driven reduced-order dynamic modeling approach for deep-DER-penetrated distribution grids 22
     - 3.2.1 Related work 23
     - 3.2.2 Overview of proposed framework 24
     - 3.2.3 Formulation of the data-driven model identification problem 25
     - 3.2.4 Delayed embedding for partially observed distribution systems 26
     - 3.2.5 Dynamic mode decomposition (DMD) for reduced-order globally linear dynamic modeling 26
     - 3.2.6 Case studies 27
   - 3.3 LLM-based EMT model creation assistant for deep-DER-penetrated distribution grids 30

3.3.1 Related work 30
3.3.2 Fine-tuning LLM as the PSCAD modeling and simulation assistant 31
3.3.3 Case studies 32
3.4 Smart field data collection and model updating tool for DER-penetrated distribution power systems 33
3.4.1 Summary of contribution 33
3.4.2 Related work 34
3.4.3 Overview of the software application 35
3.4.4 Software implementation 38
3.5 Key takeaways and future work 41

4. Screening Method for Supporting T&D Multi-fidelity Modeling 45
4.1 Desired Behavior of Short-Circuit Analysis 45
4.2 Results in Various Test Systems 45
4.2.1 Results in a Generic Dynamic Simulation 49
4.2.2 Results in a Transmission and Distribution Co-Simulation 50
4.2.3 Results in a Transmission and Distribution Co-Simulation With DER Penetration 51

5. Automated and Adaptive Distribution Modeling for Dynamic Contingency Analysis 53
5.1 Motivation 53
5.2 Introduction 54
5.3 Proposed Methodology 55
5.4 Three-Phase Fault on Three-Hundred Bus Transmission System with 50% DER Penetration 58
5.5 Contingency List Using Three-Hundred Bus Transmission System with 50% DER Penetration 68

6. Conclusions and Future Work 71

Appendices 73

A. Implementation of Advanced Distributed Energy Resource Dynamic Model (DER_A) 74
A.1 Background of Distributed Energy Resource Models 74
A.2 Power System Dynamic Modeling Algorithm 75
A.3 DER_A Model Subsystems 77
A.3.1 Voltage-Based Adjustable Reactive Power Control 78
A.3.2 Frequency-Based Adjustable Active Power Control (Droop Control) 80
A.3.3 Active Current Injection Control 80
A.3.4 Reactive Current Injection Control 81
A.3.5 Voltage Source Calculation 82
A.3.6 Voltage and Frequency Tripping Protocols 82
A.3.7 Maximum Current Values in P and Q Priority 83
A.4 Implementation of DER_A Model into the InterPSS Dynamic Simulation Algorithm 84
A.4.1 Implementation of `getOutputObject()` Method 84

A.4.2 Implementation of `nextStep()` Method 86
A.4.3 Implementation of `updateAttributes()` Method 87
A.4.4 Implementation of `afterStep()` Method 87
A.4.5 Test 1.1a Plots 90
A.4.6 Test 1.1b Plots 91
A.4.7 Test 1.2a Plots 92
A.4.8 Test 1.2b Plots 93
A.4.9 Test 2.1a Plots 94
A.4.10 Test 2.1b Plots 95
A.4.11 Test 2.2a Plots 96
A.4.12 Test 2.2b Plots 97
A.4.13 Test 2.3a Plots 98
A.4.14 Test 2.3b Plots 99
A.4.15 Test 1.1a Discussion 100
A.4.16 Test 1.1b Discussion 100
A.4.17 Test 1.2a Discussion 100
A.4.18 Test 1.2b Discussion 100
A.4.19 Test 2.1a Discussion 100
A.4.20 Test 2.1b Discussion 101
A.4.21 Test 2.2a Discussion 101
A.4.22 Test 2.2b Discussion 101
A.4.23 Test 2.3a Discussion 101
A.4.24 Test 2.3b Discussion 101

B. DER_A Functions and Code Implementation 102
B.1 Deadband Code Implementation 102
B.2 Volt/VAR Control Code Implementation 102
B.3 Droop Control Code Implementation 102
B.4 Active Current Control Code Implementation 103
B.5 Reactive Current Control Implementation 104
B.6 Voltage Source Calculation 105
B.7 Fractional Voltage Tripping Code Implementation 106
B.8 Frequency Tripping Code Implementation 108
B.9 Active and Reactive Power Priority Code Implementation 109
B.10 Ramp Rate Updating Code Implementation 109

C. Final Proposed Method Test System Model Parameterization 111
C.1 Single-Phase Induction Motor Parameterization 111
C.2 DER_A Model Parameterization 111

D. Select Test System Diagrams and Contingency Analysis Results 115
D.1 IEEE 300 Bus Test System Dynamic Load Locations 115
D.2 IEEE 300 Bus Test System Impact Zone Diagram 115
D.3 Contingency Analysis Locations Across IEEE 300 Bus Test System Impact 116
D.4 Contingency Analysis Statistics for Other Fault Locations 116

List of Figures

Figure 1.1 An example device tripping protocol for voltage-ride-through, set forth by IEEE 1547 [1] 6

Figure 2.1 TSO-DSO interaction framework for incorporating reactive power flexibility from distribution system into TSO operation 12
Figure 2.2 Reactive power capability of a DER inverter as mandated by the IEEE 1547-2022 standard & the device flexibility domain of individual PV inverter 13
Figure 2.3 (a) IEEE 37 node distribution system, (b) Normalized daily load profile and solar PV generation profile 17
Figure 2.4 6 Day-ahead aggregated capability curves and flexibility region of distribution 18
Figure 2.5 TSO-DSO test system description 18
Figure 2.6 Voltage profile with reactive power support only from generators 18
Figure 2.7 Voltage profile with reactive power support from both the generators and DER 19
Figure 2.8 Voltage profile with reactive power support only from generators 20

Figure 3.1 Overview of the proposed data-driven reduced-order dynamic modeling approach. 23
Figure 3.2 Overview of the proposed technical framework. 25
Figure 3.3 Integrated transmission-distribution test system and fault locations 28
Figure 3.4 Test results for Scenario 1. 29
Figure 3.5 Test results for Scenario 2. 30
Figure 3.6 Test results for Scenario 3. 31
Figure 3.7 Test results for Scenario 4. 32
Figure 3.8 Overview of the LLM-based PSCAD EMT assistant. 33
Figure 3.9 Fake PSCAD Python script generated by the general-purpose ChatGPT. 34
Figure 3.10 Flowchart of fine-tuning Llama for building the PSCAD modeling and simulation assistant. 35
Figure 3.11 PSCAD Python script generated by the fine-tuned Llama model. 36
Figure 3.12 The application flow for integrating GridScout into utility practices. 37
Figure 3.13 Overall software design flow. 38
Figure 3.14 Screenshots of the mobile application design. 43
Figure 3.15 Screenshot of the Streamlinedally generated OpenDSS Python script. 44

Figure 4.1 An ideal estimate compared to the dynamic simulation voltage response. Short-circuit is less than the dynamic simulation voltage sag, although close to the minimum voltage value 46
Figure 4.2 Feeder used to represent distribution systems in the dynamic T&D co-simulation .. 46
Figure 4.3 Method of verifying the similarity between short-circuit analysis and the dynamic simulation voltage sag 48
Figure 4.4 The standard IEEE 9 Bus System 49
Figure 4.5 Differences between short-circuit analysis and dynamic simulation minimum voltage 49

Figure 4.6 IEEE 9 Bus System with radial distribution feeders The loads in each are scaled based on the aggregated load they are representing 50
Figure 4.7 Differences between short-circuit analysis and dynamic simulation minimum voltage in a transmission and distribution co-simulation 51
Figure 4.8 Differences between short-circuit analysis and dynamic simulation minimum voltage with DER penetration 52

Figure 5.1 Example multi-fidelity system when utilizing short-circuit analysis to anticipate voltage 56
Figure 5.2 Flowchart of proposed algorithm for dynamic contingency analysis with selective system building 57
Figure 5.3 Composite load model (CMPLDWG) oneline [2] 58
Figure 5.4 Areas of aggregated vs. disaggregated modeling areas for separate contingencies, and switching between them 59
Figure 5.5 A zoomed-in plot of the impact zones found through short-circuit analysis due to a fault at Bus 45 60
Figure 5.6 Select internal states of the single DER underneath Bus 47 in the aggregated modeling approach immediately after (a) and many seconds (b) after the fault 61
Figure 5.7 Select internal states of the DER at Bus 6 on the feeder underneath Bus 47 in the disaggregated and multi-fidelity approach immediately (a) and several seconds (b) after the fault 61
Figure 5.8 Active power from the single DER underneath Bus 47 compared to the combined active power from all DERs in the disaggregated feeder underneath Bus 47 62
Figure 5.9 Reactive power from the single DER underneath Bus 47 compared to the combined active power from all DERs in the disaggregated feeder underneath Bus 47 62
Figure 5.10 The immediate (a) and prolonged (b) voltage responses for the three separate simulation methods at Bus 47 due to a three-phase fault located at Bus 45 63
Figure 5.11 Active power from the single DER underneath Bus 71 compared to the combined active power from all DERs in the disaggregated feeder underneath Bus 71 64
Figure 5.12 Reactive power from the single DER underneath Bus 71 compared to the combined active power from all DERs in the disaggregated feeder underneath Bus 71 64
Figure 5.13 The prolonged voltage response (b) and the immediate response (a) for the three separate simulation methods at Bus 71 due to a three-phase fault located at Bus 4565
Figure 5.14 Simulation time increase found when compared to the aggregated modeling approach to the disaggregated approach and the multi-fidelity approach 66
Figure 5.15 Error introduced when comparing the disaggregated modeling approach to the aggregated approach and the multi-fidelity approach, in terms of average RMSE (a) and maximum voltage difference (b) 67
Figure 5.16 Sensitivity analysis associated with adjusting the threshold delineating between areas of disaggregation and aggregation for the multi-fidelity modeling approach .. 67
Figure 5.17 Error introduced when comparing the disaggregated modeling approach to the aggregated approach and the multi-fidelity approach in terms of average RMSE (a), and maximum voltage difference (b) due to a fault at Bus 38 69

Figure 5.18 Simulation runtime increase when comparing the aggregated modeling approach to the disaggregated approach and the multi-fidelity approach due to a fault at Bus 38 70
Figure 5.19 Error introduced when comparing the disaggregated modeling approach to the aggregated approach and the multi-fidelity approach (b), and simulation runtime increase when comparing the aggregated modeling approach to the disaggregated approach and the multi-fidelity approach (a) due to a fault at Bus 24670

Figure A.1 The algorithm used by InterPSS for dynamic simulation 77
Figure A.2 The subsystems of the DER_A model 78
Figure A.3 Generic Volt/VAR curve used in DERs 79
Figure A.4 Block Diagram of Volt/VAR Control 80
Figure A.5 Block diagram of droop control 80
Figure A.6 Block diagram for control of active current injection 81
Figure A.7 Block diagram for control of reactive current injection 82
Figure A.8 Block diagram for the interface between the DER_A model and the rest of the system 83
Figure A.9 Behavior of voltage tripping protocol in the DER_A model 84
Figure A.10 Active and Reactive Currents, along with Active and Reactive Power outputs from the DER_A model during an over-voltage scenario 90
Figure A.11 Filtered (measured) voltage and the voltage multiplier (fraction of unit tripped) of the DER_A model during an over-voltage scenario 90
Figure A.12 Active and Reactive Currents, along with Active and Reactive Power outputs from the DER_A model during an under-voltage scenario 91
Figure A.13 Filtered (measured) voltage and the voltage multiplier (fraction of unit tripped) of the DER_A model during an under-voltage scenario 91
Figure A.14 DER_A model states of Active Current and Power, PI Control, Ordered Change in Power, and Ordered Power during an over-frequency scenario 92
Figure A.15 DER_A model terminal frequency during an over-frequency scenario 92
Figure A.16 DER_A model states of Active Current and Power, PI Control, Ordered Change in Power, and Ordered Power during an under-frequency scenario 93
Figure A.17 DER_A model terminal frequency during an under-frequency scenario 93
Figure A.18 Active and Reactive Currents, along with Active and Reactive Power outputs from the DER_A model during an over-voltage scenario which trips the model 94
Figure A.19 Filtered (measured) voltage and the voltage multiplier (fraction of unit tripped) of the DER_A model during an over-voltage scenario which trips the model 94
Figure A.20 Active and Reactive Currents, along with Active and Reactive Power outputs from the DER_A model during an under-voltage scenario which trips the model 95
Figure A.21 Filtered (measured) voltage and the voltage multiplier (fraction of unit tripped) of the DER_A model during an under-voltage scenario which trips the model 95
Figure A.22 Active and Reactive Currents, along with Active and Reactive Power outputs from the DER_A model during an over-voltage scenario which partially trips the model 96

Figure A.23 Filtered (measured) voltage and the voltage multiplier (fraction of unit tripped) of the DER_A model during an over-voltage scenario which partially trips the model 96
Figure A.24 Active and Reactive Currents, along with Active and Reactive Power outputs from the DER_A model during an under-voltage scenario which partially trips the model 97
Figure A.25 Filtered (measured) voltage and the voltage multiplier (fraction of unit tripped) of the DER_A model during an under-voltage scenario which partially trips the model 97
Figure A.26 DER_A model states of Active Current and Power, PI Control, Ordered Change in Power, and Ordered Power during an over-frequency scenario which trips the model 98
Figure A.27 DER_A model terminal frequency during an over-frequency scenario which trips the model 98
Figure A.28 DER_A model states of Active Current and Power, PI Control, Ordered Change in Power, and Ordered Power during an under-frequency scenario which trips the model 99
Figure A.29 DER_A model terminal frequency during an under-frequency scenario which trips the model 99

Figure D.1 The IEEE 300 Bus System. Nine bus distribution feeder locations are marked with blue dots. Image adopted from [3] 115
Figure D.2 High and low impact zone areas based on a fault located at Bus 45 118
Figure D.3 The fault locations tested in the contingency analysis. All buses boxed in red are tested with a three-phase fault applied to each one 119

List of Tables

Table 2.1 reactive power generation in different contingencies with and without DER support 20

Table A.1 Varying DER Models 75
Table A.2 Varying Tests Conducted on the DER_A Model 89

Table C.1 Single-Phase AC Induction Motor Parameters 112
Table C.2 DER_A Model Parameters 113
Table C.3 DER_A Model Parameters Cont. 114

Table D.1 Statistics due to a Three-Phase Fault at Bus 76 116
Table D.2 Statistics due to a Three-Phase Fault at Bus 122 116
Table D.3 Statistics due to a Three-Phase Fault at Bus 4 116
Table D.4 Statistics due to a Three-Phase Fault at Bus 182 117
Table D.5 Statistics due to a Three-Phase Fault at Bus 323 117

1. Introduction

1.1 Motivation

As the implementation of FERC Order 2222 is coming and DER proliferate, it is imperative to adequately model and efficiently analyze the dynamic impacts of distributed energy resource (DER) on transmission and distribution (T&D) systems, capture and leverage full capabilities of DER to facilitate large-scale DER integration and T&D system operation. Integrated T&D modeling and co-simulation tools have been developed by reusing existing simulators. One fundamental issue is that existing transmission and distribution system simulation tools are modeling-fidelity-agnostic, i.e., they solve dynamic simulation problems with all the details in the input system models regardless of system conditions and contingencies. As a result, they are computationally inefficient and inadequate to deal with complex, large-scale T&D systems, and engineers must manually perform model reduction or simplification for almost every study, which is ad-hoc, time-consuming and error-prone. All these contribute to renewable integration queue backlog problems in many independent system operators (ISOs) and utilities. One of our goals is help ISOs and utilities address these issues by transforming the model reduction and selection from a manual, ad-hoc and out-of-simulation-loop process into a systematic, automated, and AI-enhanced process within a suite of new T&D modeling and simulation tools. Another goal is to help the industry tap into the var flexibility offered by DERs to enhance T&D system voltage stability as well as renewable integration.

To achieve the goals above, this project develops an adaptive, multi-fidelity and AI-accelerated T&D co-simulation tool to improve the computational efficiency of dynamic simulation for large-scale T&D systems, and make transient stability simulation and dynamic contingency analysis of large-scale T&D systems on laptops and servers feasible and practical. Moreover, to address the issues of lack of multi-fidelity distribution system models and inconsistent modeling among different studies, the project focuses on developing an automated modeling tool to create a multi-fidelity model library for distribution systems and DERs based on their full or detailed models. A short-circuit anslysis based automated, multi-fidelity model selection approach is developed to intelligently select and compose T&D models of suitable fidelity from the model library to create study cases for contingencies being considered. This can significantly reduce the manual work for model data preparation and study case setup, while significantly enhancing computational efficiency. In addition, this project investigates methods for aggregating DER reactive power capability at the T&D interface to generate aggregated Q-capability curves, and leveraging them to enhance composite load models and support short-term and long-term voltage stabilities.

1.2 Background

This section introduces the main concepts and topics related to T&D dynamic modeling and simulation. The mathematics and implications of short-circuit analysis, a transmission and distribution dynamic co-simulation, dynamic contingency analysis, and dynamic behaviors tied to voltage of DERs and dynamic loads are presented. In subsequent chapters, these tools and techniques are utilized for use in the final, proposed method.

1.2.1 Power System Dynamic Simulation

There are varying ways in which a dynamic simulation is conducted in system studies. One of the main methods is the partitioned approach, where the system is separated into a set of differential equations alongside a set of nonlinear algebraic equations. Namely, the system is represented by two groups of equations, comprising a total set of differential and algebraic equations as follows [4]:

$$\dot{x} = f(x, y, u) \tag{1.1}$$

$$0 = g(x, y, u) \tag{1.2}$$

At each timestep, the algebraic equation is solved via eq. 1.2, where x is a set of state variables, y is a set of algebraic state variables, and u is a set of external inputs. This equation must be solved iteratively until convergence, mainly due to current injections being a function of system voltages (each new set of system voltages produces new current injections, which in turn produce new system voltages, and this process continues until convergence). Following convergence, the dynamic devices within the system are modeled through eq. 1.1. This step performs numerical integration with the voltages found via the network equation (eq. 1.2), producing a state vector x that is in turn used in eq. 1.2. This process repeats itself for all time steps in the simulation.

A dynamic simulation conventionally solves this set of differential and algebraic equations for the whole system in a singular, uniformly modeled manner. In other words, there are no subsystems, but rather a single consistently modeled system. A co-simulation differs from this, as distribution systems are solved alongside the transmission system in a separated fashion. Methods for co-simulation have been a large topic of recent research, as the different representations of distribution and transmission systems introduce challenges in boundary conflicts. For example, the majority of transmission system modeling is done with sequence components (usually only positive sequence), whereas distribution simulations are often done in a three-phase manner. The conflicting representations at boundaries between these systems make synchronization a difficult task. Also, if they are modeled in a decoupled manner, convergence is not guaranteed. One method to combat this issue is the Multi-Area Thevenin Equivalent (MATE) approach [5]. This approach utilizes the theory of superposition to its advantage for each of these separate subsystems (each distribution system). The bus voltages at the boundaries of distribution and transmission systems can be found via:

$$V_{i,tot} = V_{i,int} + V_{i,ext} \tag{1.3}$$

Where $V_{i,int}$ is the voltage at subsystem boundary i considering *only* internal sources of the subsystem, $V_{i,ext}$ is the voltage subsystem boundary i due to the influence of exterior subsystems *only*, and $V_{i,tot}$ is the final realized subsystem boundary voltage. The voltages due to exterior subsystems are computed through the link branches (lines) connecting all subsystems, with each system represented by a thevenin equivalent. Here, 1.2 is broken down into 1.3. These voltages are solved for iteratively, in the same manner as before, therefore not introducing any additional convergence issues. More information on the MATE approach can be found in [6]. InterPSS [7], an open-source

simulation engine, implements this approach and is chosen as the dynamic co-simulation tool for this study.

1.2.2 Dynamic Contingency Analysis

Dynamic contingency analysis is a critical part of power system studies, used to evaluate the system's behavior and stability under a range of potential disturbances, such as faults, line outages, or generator trips. Unlike static contingency analysis, which focuses on steady-state conditions, dynamic analysis simulates the time-dependent response of the power system, capturing the interaction of generators, loads, and control systems over seconds and/or minutes following a disturbance. Particularly for systems with high penetrations of motor loads and DERs, the time following a contingency can trigger device tripping, grid control schemes, and other unique dynamic behaviors that static contingency analysis cannot capture. Therefore, dynamic contingency analysis is vital for numerous system studies, and is necessary for the modernization of the power grid.

In bulk power systems, the number of contingencies, n, to examine grows linearly (the number of contingencies to examine increases linearly with the growth of the number of devices and buses to model). In a dynamic contingency analysis, each separate contingency is simulated to verify system stability under the current state of the system. Sometimes, system operators simulate multiple contingencies at once, where k the number of contingencies in a single simulation. In total, this kind of contingency analysis is called $n - k$ contingency analysis. It verifies that if k contingencies out of n possible contingencies occur, the system will or will not be stable.

This study offers results and verification of the proposed method in an $n - 1$ dynamic contingency analysis format, where the individual contingency under study is a three-phase to ground transmission level fault. While this a subsection of the total contingencies to analyze in a dynamic contingency analysis (it does not include generator outages, line outages, etc.), computational savings are substantial and can provide significant time savings for utilities overall. Application of the proposed method to various types of faults and other contingencies are discussed, however their verification lies in future research.

1.2.3 Short-Circuit Analysis

The retained voltage levels across a system due to a fault is a pivotal metric for varying system studies. One such method of understanding the steady state voltage profile of the system due to a fault is short-circuit analysis. Generically, this is a algebraic, phasor based solution that obtains steady state post-fault voltages at all buses in a system. This analysis relies on the theory of superposition, by stating the bus voltages prior to the fault, plus the bus voltages due to *only* the fault (all generation sources are omitted), equals the total realized bus voltages. Mathematically, this is expressed by:

$$\tilde{V}_{tot} = \tilde{V}_{pre} + \tilde{V}_{fault} \tag{1.4}$$

Where $\tilde{V}_{tot}$ is the vector of all bus voltages in the system with the fault applied, $\tilde{V}_{pre}$ is the vector of all bus voltages in the system without the fault applied, and $\tilde{V}_{fault}$ is the vector of all bus voltages in the system with *only* the fault applied (all sources of generation are omitted). The tilde above the voltages represent that these are phasor quantities.

To find $\tilde{V}_{pre}$, one simply uses a conventional power flow technique, such as Newton-Raphson. To find $\tilde{V}_{fault}$, one can first write:

$$\begin{bmatrix} \tilde{V}_{1,fault} \\ \tilde{V}_{2,fault} \\ \vdots \\ \tilde{V}_{F,fault} \\ \vdots \\ \tilde{V}_{n,fault} \end{bmatrix} = \begin{bmatrix} \tilde{Z}_{11} & \tilde{Z}_{12} & \cdots & \tilde{Z}_{1F} & \cdots & \tilde{Z}_{1n} \\ \tilde{Z}_{21} & \tilde{Z}_{22} & \cdots & \tilde{Z}_{2F} & \cdots & \tilde{Z}_{2n} \\ \vdots & \vdots & \ddots & \vdots & \ddots & \vdots \\ \tilde{Z}_{F1} & \tilde{Z}_{F2} & \cdots & \tilde{Z}_{FF} & \cdots & \tilde{Z}_{Fn} \\ \vdots & \vdots & \ddots & \vdots & \ddots & \vdots \\ \tilde{Z}_{n1} & \tilde{Z}_{n2} & \cdots & \tilde{Z}_{nF} & \cdots & \tilde{Z}_{nn} \end{bmatrix} \cdot \begin{bmatrix} \tilde{I}_{1,fault} \\ \tilde{I}_{2,fault} \\ \vdots \\ \tilde{I}_{F,fault} \\ \vdots \\ \tilde{I}_{n,fault} \end{bmatrix}$$

Where F denotes the fault bus and n denotes the number of buses in the system. In generic short-circuit analysis, it is assumed that fault current injections are zero at all non-fault buses. Thus, the matrix equation is simplified:

$$\begin{bmatrix} \tilde{V}_{1,fault} \\ \tilde{V}_{2,fault} \\ \vdots \\ \tilde{V}_{F,fault} \\ \vdots \\ \tilde{V}_{n,fault} \end{bmatrix} = \begin{bmatrix} \tilde{Z}_{11} & \tilde{Z}_{12} & \cdots & \tilde{Z}_{1F} & \cdots & \tilde{Z}_{1n} \\ \tilde{Z}_{21} & \tilde{Z}_{22} & \cdots & \tilde{Z}_{2F} & \cdots & \tilde{Z}_{2n} \\ \vdots & \vdots & \ddots & \vdots & \ddots & \vdots \\ \tilde{Z}_{F1} & \tilde{Z}_{F2} & \cdots & \tilde{Z}_{FF} & \cdots & \tilde{Z}_{Fn} \\ \vdots & \vdots & \ddots & \vdots & \ddots & \vdots \\ \tilde{Z}_{n1} & \tilde{Z}_{n2} & \cdots & \tilde{Z}_{nF} & \cdots & \tilde{Z}_{nn} \end{bmatrix} \cdot \begin{bmatrix} 0 \\ 0 \\ \vdots \\ \tilde{I}_{F,fault} \\ \vdots \\ 0 \end{bmatrix}$$

Therefore, it can be seen that for a three phase fault at bus F, the voltage at bus k due to only the fault itself can be expressed as:

$$\tilde{V}_{k,fault} = \tilde{Z}_{kF}\tilde{I}_{F,fault}$$

And from this, the bus voltages across the system due to the fault itself can be written as:

$$\begin{bmatrix} \tilde{V}_{1,fault} \\ \vdots \\ \tilde{V}_{F,fault} \\ \vdots \\ \tilde{V}_{n,fault} \end{bmatrix} = \begin{bmatrix} \tilde{Z}_{1F}\tilde{I}_{F,fault} \\ \vdots \\ \tilde{Z}_{FF}\tilde{I}_{F,fault} \\ \vdots \\ \tilde{Z}_{nF}\tilde{I}_{F,fault} \end{bmatrix} \tag{1.5}$$

Finally, the total realized bus voltages across the system are computed via:

$$\begin{bmatrix} \tilde{V}_{1,tot} \\ \vdots \\ \tilde{V}_{n,tot} \end{bmatrix} = \begin{bmatrix} \tilde{V}_{1,pre} \\ \vdots \\ \tilde{V}_{n,pre} \end{bmatrix} + \begin{bmatrix} \tilde{Z}_{1F}\tilde{I}_{F,fault} \\ \vdots \\ \tilde{Z}_{nF}\tilde{I}_{F,fault} \end{bmatrix} \tag{1.6}$$

When the bus voltages prior to the fault are already computed for the system through the power flow results, it is important to note here that the computational complexity of short-circuit analysis is $O(n)$. In other words, the computational complexity increases linearly with the number of buses n are in the system.

As a final point, short-circuit analysis is not time based or a dynamic representation of the system due to a fault. It cannot accomplish the same dynamic analysis of the system as it is a static, phasor solution that ignores the fault current injection from DERs and dynamic loads, as well as their unique voltage-ride-through, stalling, and grid control protocols. However, since it omits these characteristics, the voltage results it obtains are generally lower than those obtained during a dynamic simulation. Hence, short-circuit analysis errors compared to a dynamic simulation conservatively, which is a vital component of an estimation tool and will be discussed in further detail in the body of the thesis.

1.2.4 Distributed Energy Resources and Dynamic Load Coupling With Voltage

As discussed earlier in the introduction, dynamic behaviors of DERs and single phase induction motor loads are highly voltage-sensitive. For example, IEEE 1547 [1] declares that all new DERs shall be equipped with dynamic reactive power injection control, based off their point of common coupling (PCC) voltage. This means, based on the connection point of DERs, the varying voltage at that point will introduce reactive power injection. Furthermore, voltage-ride-through behaviors are not only strictly voltage dependent, but also dependent on voltage over a time threshold. Therefore, not only are device protections and grid control techniques coupled with voltage, but they are also coupled dynamically with voltage. This is one of the main necessities of dynamic simulations as opposed to static, non-time based simulations as time thresholds cannot be captured. 1.1 shows the general protocol for voltage-ride-through protocols, dictated from IEEE 1547. As these characteristics are time based, this means that a static contingency analysis cannot capture the possible tripping characteristics presented by devices' protection protocols.

Additionally, motor stalling is a common issue with single and three phase induction motor loads. Stalling occurs when terminal voltages drop below a certain threshold (e.g., 0.5-0.6 pu) for a short period of time (sometimes as fast as 2 cycles). The reactive power consumption and current draw from these devices in a stalled state is extreme, and amplifies voltage differences along a feeder line. In turn, voltages at the end of feeders falls more, creating a deep voltage sag. Voltages at the transmission level often are delayed in their recovery due to this phenomena, taking several seconds to even minutes to return to pre-contingency conditions.

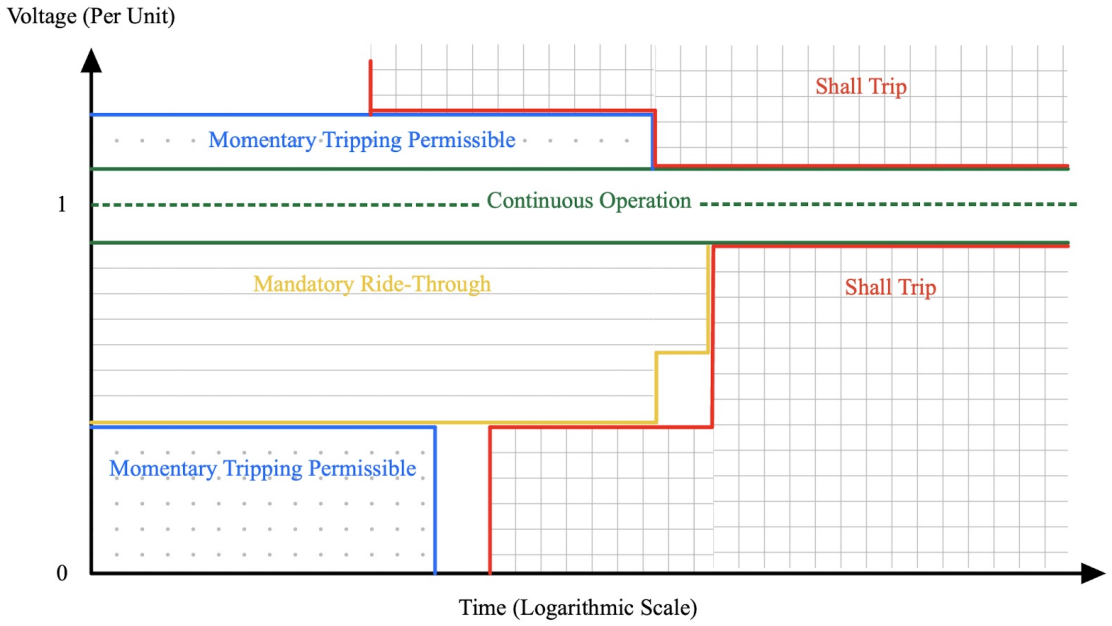


Figure 1.1: An example device tripping protocol for voltage-ride-through, set forth by IEEE 1547 [1]

Shortcomings of the aggregated modeling approach

Because of the potential of voltage drops along a feeder line being exaggerated during certain scenarios, the necessity of disaggregation is vital with the increase prevalence of dynamic grid devices. For example, motor loads and DERs may or may not trip based on their location on a feeder, DERs may or may not injection reactive power based on their location on a feeder, etc. When modeled in an aggregated manner, the dynamic response of voltage drops along a feeder aren't encapsulated. If DERs would trip in the closer to real-world scenario (disaggregation), an aggregated approach would fail to model the dynamic response of the system appropriately. In a future with large amounts of DERs, these dynamic behaviors will be vital as a significant amount of power injection into the system could become misrepresented in dynamic simulations. Therefore, there serves a great need for disaggregated distribution system inclusion into tranmission level studies.

1.3 Project outcomes

The project outcomes and major contributions are summarized below.

1.3.1 Aggregrate DER reactive power capability curve

In chapter 2, an aggregated reactive power capability curve of an unbalanced distribution system is derived and optimal DER Q set-points based on the requested VAR amount at the T & D interface are identified. This is achieved by three steps, starting with an estimate of the capability curve and modeling of the capability curve on the transmission side grid for a contingency scenario, and

ending with dispatching reactive power set points to provide transmission system operator (TSO) with the requested reactive power.

The proposed approach utilizes the aggregated reactive power capability of the DERs to optimally dispatch these resources to rectify voltage violations during contingencies. The aggregation of reactive power from DERs is showcased on IEEE 37-node distribution systems. To utilize the reactive power capability, an IEEE 9 bus transmission system is integrated with several IEEE 37-node distribution systems. The transmission system optimal power flow (OPF) provides the optimal reactive power support required for maintaining the voltage within the allowable limit. The sensitive-aware reactive power dispatch limits the number of DERs in the distribution that support the grid during contingencies. This indirectly reduces the impact of communication issues. The sensitivity-aware reactive power dispatch can also decrease overall reactive power loss in the distribution system. From the above observations, the key takeaway points are listed below.

- A synchronous machine alone may be insufficient to maintain feasible operation during contingencies. However, by leveraging aggregated reactive power support from DERs, these infeasibilities can be mitigated, resulting in improved voltage control. Moreover, local DER-based reactive support is often more effective than contributions from remote generators due to its proximity to the load buses.
- The sensitivity-aware reactive power dispatch can select a set of more effective DERs to provide TSO with its requested amount of reactive power, reducing the number of participating DERs. This indirectly leads to lower communication requirements and lower reactive power losses in the distribution system.

1.3.2 Data-driven and LLM-assisted dynamic modeling approaches for deep-DER-penetrated distribution systems

In chapter 3, we first developed a data-driven reduced-order dynamic modeling approach for accurately representing the deep-DER-penetrated distribution power grids in the transmission-level transient stability assessments. The proposed approach utilizes the recently developed theoretical and computational tools in Koopman operator and delay-embedded dynamic mode decomposition (DMD), which can 1) properly balance the modeling accuracy and modeling complexity; 2) identify reduced-order dynamic models with partial observations; 3) maintain physical interpretability by identifying a globally linear state space dynamic model. We then developed a large language model (LLM) based PSCAD modeling and assistant for creating PSCAD electromagnetic (EMT) dynamic models and running EMT simulations toward representing the accurate EMT dynamics of the deep-DER-penetrated distribution power grids in the transmission-level transient stability assessments. The fine-tuned LLM can effectively reduce hallucinations in general-purpose LLMs which is critical for generating correct PSCAD Python scripts for EMT modeling and simulations in PSCAD. We also developed a smart field data collection and model updating tool for DER-penetrated distribution power systems. The tool allows for streamlined distribution power grid modeling during field equipment installation and maintenance via a mobile device application operated by field technicians and other utility personnel. This tool addresses the substantial need

for distribution utilities to efficiently manage the intensive grid model creation and updating efforts caused by the rapid growth of distributed energy resources (DERs) and aging grid infrastructure.

The developed data-driven reduced-order dynamic modeling approach can be adopted for: 1) identifying model structural deficiency of reduced-order dynamic distribution system models; 2) developing fast dynamic transmission-distribution co-simulation approaches using the reduced-order dynamic models which are globally linear; 3) developing data-driven control algorithms with the reduced-order globally linear dynamic models.

The developed LLM-based PSCAD modeling and simulation assistant can be adopted for developing LLM-assisted power system planning tools. The proposed LLM fine-tuning framework can be adopted for 1) fine-tuning Llama for other power system domain-specific applications; 2) accelerating the DER/IBR interconnection process with LLM-assisted tools.

For the smart field data collection and model updating tool for DER-penetrated distribution systems, future work may include: 1) allowing the tool to directly read an image of the equipment nameplate and parse it into nameplate parameters; 2) extending the software toward supporting more types of equipment, enabling multi-media recordings of equipment installation, replacement, or maintenance logs/notes; 3) enabling metering data management; 4) supporting more distribution system modeling and simulation software.

1.3.3 short-circuit-based screening method for automated, multi-fidelity modeling

In chapter 4, we proposed an automated methodology to construct multi-fidelity transmission and distribution (T&D) dynamic study cases. The approach is built on a short-circuit-based screening that estimates post-fault voltages and identifies high-impact regions of the network that require detailed, disaggregated distribution modeling. Regions outside the high-impact zones are aggregated, thereby reducing model size and computational burden while maintaining sufficient accuracy in critical areas.

The case-building process integrates model selection, thresholding of short-circuit results, and automated feeder assembly, resulting in study cases that balance accuracy and efficiency without requiring extensive manual intervention. This framework enables system operators and planners to quickly construct simulation-ready models across a wide set of contingencies. Key insights from the case studies include:

- The proposed workflow substantially reduces case-building time and manual modeling effort compared to traditional, fully disaggregated approaches.
- Threshold-based identification of high-impact zones ensures that disaggregation is applied only where it is most needed, avoiding unnecessary computational overhead.
- The resulting study cases preserve dynamic fidelity in voltage-sensitive areas while offering computational gains that make large-scale contingency studies more practical.

1.3.4 Automated, multi-fidelity T&D dynamic simulation engine and case study

In chapter 5, we presented the implementation of a multi-fidelity T&D dynamic simulation engine and demonstrated its effectiveness through case studies. The engine couples transmission- and distribution-level models of varying fidelity within a unified simulation environment, allowing simultaneous evaluation of aggregated and disaggregated components. High-impact regions identified by the automated case-building tool are modeled with detailed dynamics, while low-impact regions remain aggregated, ensuring both accuracy and computational efficiency.

Case studies on a large-scale 300-bus transmission system with high DER penetration highlight the advantages of the approach. Compared with fully aggregated simulations, the proposed method reduced average root-mean-square error (RMSE) in bus voltage trajectories by more than an order of magnitude, while compared with fully disaggregated simulations, runtime was reduced by over a factor of four. In addition, overhead from short-circuit screening and system reconstruction was found to be negligible relative to total simulation time.

The results confirm that the multi-fidelity simulation engine provides a scalable and adaptive framework for dynamic contingency analysis in DER-rich T&D systems. This enables operators and planners to conduct high-fidelity studies on practical computational platforms, supporting improved decision-making for system reliability and DER integration.

1.3.5 T&D test cases

This project developed a series of benchmark test cases for test and validation of the developed methods:

- **Chapter 2: Aggregate DER reactive-power capability curves.** A combined test system of the IEEE 9-bus transmission network and multiple IEEE 37-node distribution feeders was used. DER inverter limits were modeled according to IEEE 1547-2020.
- **Chapter 3: Data-driven and AI-assisted distribution modeling.** IEEE 39-bus transmission system with one transmission-level load replaced by a balanced IEEE 13-node feeder system, which generated the dataset for reduced-order dynamic model identification and validate the delay-embedded DMD/Koopman approach.
- **Chapter 4: Short-circuit-based screening.** IEEE 9-bus and IEEE 300-bus transmission systems, both with and without integrated 8-bus distribution feeders, were used to compare short-circuit voltage estimates against dynamic simulation results.
- **Chapter 5: adaptive, multi-fidelity modeling and dynamic contingency analysis.** A new T&D test case comprising 300-bus transmission system and 8-bus feeders with 50% DER penetration was created and employed to evaluate the automated multi-fidelity modeling and dynamic contingency analysis method.

1.4 Report Organization

The report is organized as follows. Chapter 2 presents the approach for obtaining the aggregated DER reactive power capability curve and the key insights observed from integrating the aggregated DER reactive power capability curve into the T&D system operations. Chapter 3 presents the data-driven reduced-order dynamic modeling approach for accurately representing the deep-DER-penetrated distribution power grids in the transmission-level transient stability assessments, the LLM-based PSCAD EMT modeling and simulation assistant, and the smart field data collection and model updating software tool for DER-penetrated distribution power systems. Chapter 4 presents the short-circuit-analysis-based automated multi-fidelity modeling and study case building process. Chapter 5 presents the multi-fidelity T&D dynamic simulation engine and case study results. Chapter 6 provides concluding remarks to this report.

2. Aggregate DER Reactive Power Capability curve

2.1 Objective & Introduction

With high DER penetration, the distribution system (D-system) is no longer a passive network and is capable of providing VAR-related ancillary services to the grid. These geographically distributed DERs can be used in Volt/VAR control mode to provide both inductive and capacitive VAR [8]. As the number of installed DERs in the D-system grows, with appropriate control, DERs can enhance regional VAR availability and positively affect the voltage stability of the electric grid. However, it is a challenge for the transmission system operator (TSO) to directly control the flexibility of DERs because of (a) the higher computational cost to analyze the integrated transmission and distribution (T & D) power system, (b) coordination with distribution system operator (DSO) as DSO is responsible for controlling DER generation.

To utilize the DER for var-related ancillary services, these DERs must be aggregated by DSO/aggregator, and the aggregated capability of the DERs needs to be communicated ahead of time to the transmission side operator(TSO) to be effectively utilized for voltage stability. The aggregated flexibility must be incorporated into the decision-making process of TSO to determine the amount of reactive power required at different locations of the network for maintaining voltage within the prescribed limit.To achieve this objective in this project, an aggregated reactive power capability curve of an unbalanced distribution system is derived and optimal DER Q set-points based on the requested VAR amount at the T & D interface are identified. These tasks can be divided into three steps, starting with an estimate of the capability curve and modeling of the capability curve on the transmission side grid for a contingency scenario, and ending with dispatching reactive power set points to provide TSO with the requested reactive power.

2.2 Framework

In a traditional power system, conventional generators and static VAR compensators (SVCs) are relied upon to supply reactive power for voltage regulation during contingencies that cause voltage violations. However, these devices may quickly reach their operational limits, particularly when large amounts of reactive power must be injected due to the long electrical distance between generation sources and load buses. To address this limitation, the reactive power flexibility of distributed energy resources (DERs) is utilized to support transmission-level voltage control as illustrated in Fig. 2.1. The framework integrates distribution-side optimal power flow (D-OPF) problems for aggregation of reactive power from DER, transmission-side OPF (T-OPF) to decide reactive power requirement for voltage control, and one more D-OPF for reactive power set point dispatch for the participating DERs.

- **DSO-1 OPF:**Estimation of aggregated reactive $[Q_{cap} - Q_{ind}]$ of the distribution system: This process considers the distribution network, load & generation at different nodes, and provides information on the maximum capacitive (Q_{cap}) & inductive (Q_{ind}) flexibility that can be attained by controlling DER set points. The aggregated reactive power flexibility or capability $[Q_{cap} - Q_{ind}]$ is provided as an input to the next module of the transmission system

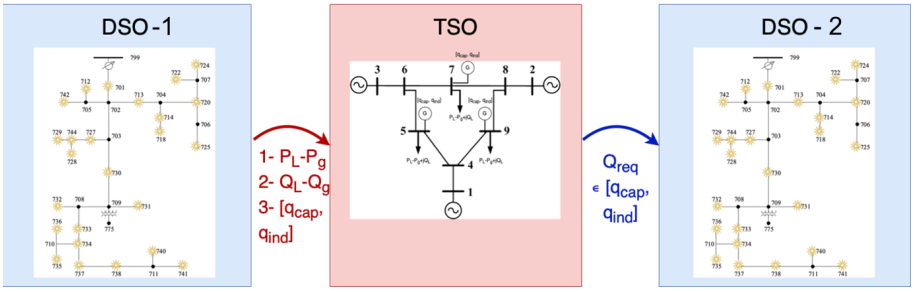


Figure 2.1: TSO-DSO interaction framework for incorporating reactive power flexibility from distribution system into TSO operation

optimization.

- **TSO-optimization** : The proposed TSO optimization utilizes the available aggregated reactive power capability at different locations of the transmission network to determine the minimum (Q_{req}) reactive power support required to improve the voltage during a contingency. The required reactive power support Q_{req} is requested from the DSO, which is obatined by controlling the DERs in the distribution system.

- **DSO-2 OPF:**Finally, the (Q_{req}) reactive power support requested by the TSO is dispatched using sensitivity-aware dispatch to the effective DERs of the distribution system.

2.3 Estimation of aggregated reactive power capability

2.3.1 Description of inverter limits

As inverter-based DERs are geographically distributed, they can be visualized as mini–Static Voltage Compensators (SVC). These Mini SVCs can provide aggregated flexibility for the transmission system by providing local VAR support to the grid as an ancillary service. Also, DER integration standard IEEE 1547- 2018 requires each DER to reserve 44% of its apparent power rating for reactive power management. The flexibility domain of individual PV inverters can be characterized as shown in the Fig. 2.2 and can be written as (2.1). By controlling the real and reactive power set points to the DERs, any operating point can be achieved in the shaded region of the DER operation. However, without curtailing the active power generation, the reactive power capability of individual DERs, is presented as q^{gmax}. It can be observed that reactive power is constrained by the real power generation of DER P^g and inverter rating S^g.

$$q_j^{g2} \leq S_j^{g2} - p_j^{g2} \tag{2.1}$$

2.3.2 Linear model of D-system

The reactive power contributions from DERs cannot be simply summed algebraically, as their dispatch must satisfy distribution-level operational constraints, including node voltage limits. Also,

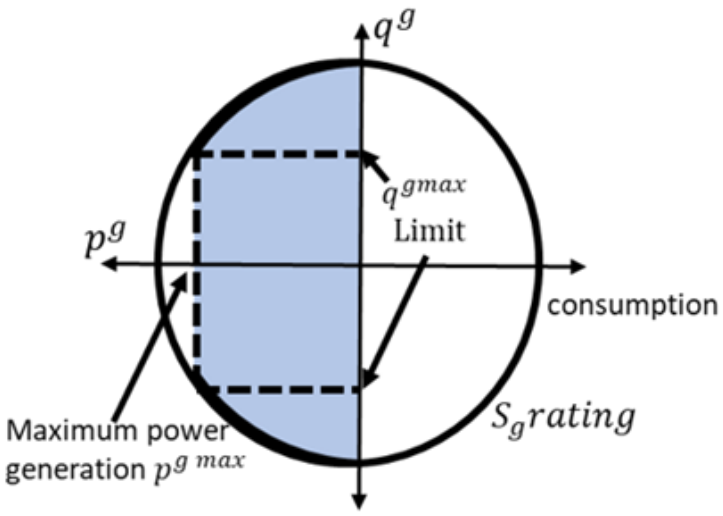


Figure 2.2: Reactive power capability of a DER inverter as mandated by the IEEE 1547-2022 standard & the device flexibility domain of individual PV inverter

the loads in the distribution system can be voltage-dependent. To capture these effects, the distribution system is explicitly modeled and incorporated into the OPF formulation, ensuring that both operational constraints and load–voltage dependencies are preserved. For this purpose, a widely adopted linear representation of the distribution network is employed. Specifically, an extension of the *LinDistFlow* model is used to accommodate unbalanced three-phase circuits, thereby enabling a computationally tractable yet accurate formulation of the D-system within the OPF framework [9, 10]. The goal is to determine a linear relationship between the squared voltage term and power injection at D-system nodes that can be used in linear optimization. Applying KVL & KCL to the adjacent node of the 3phase unbalance network we can write (2.2), where $P_j = [P_a P_b P_c]_j^T$ & $Q_j = [Q_a Q_b Q_c]_j^T$ represent the active and reactive power entering at node j for phase a,b,c and V_j represents the 3phase voltage vector for node j. Z_{ij}^p and Z_{ij}^q are the three-phase impedance coefficient matrices of the line connecting node $i\&j$.

$$V_i V_i^* = V_j V_j^* - Z_{ij}^p P_j - Z_{ij}^q Q_j \tag{2.2}$$

Using the connectivity matrix 'M', we can represent the squared voltages of each node of D-system in compact form given in (2.3). The squared voltage term is written with the variable $Y_i = V_i V_i^*$.

$$\begin{bmatrix} M_0 & M^T \end{bmatrix} \begin{bmatrix} Y_0 & Y \end{bmatrix}^T = -Z_{ij}^p P_j - Z_{ij}^q Q_j \tag{2.3}$$

However the voltage dependencies of the loads add to the complexity of linearized equations. Considering $a_{\phi,j}^0$ & $a_{\phi,j}^1$ are the fraction of load which are constant power and voltage dependent respectively at phase ϕ and node j, the loads at each node can be represented as

$$p_{\phi,j}^l(V_{\phi,j}) = p_{\phi,j}^l(a_{\phi,j}^0 + a_{\phi,j}^1 V_{\phi,j}^2) \tag{2.4}$$

Also the difference in power entering at a node and leaving for connected adjacent node, can be equated to net load demand at that node. Net load is the difference in load and generation at that

node. This power balance is represented in (2.5).

$$\begin{aligned} MP &= p^g - (p^l a^0_{\phi,j} + diag(p^l) Y a^1_{\phi,j}) \\ MQ &= q^g - (q^l a^0_{\phi,j} + diag(q^l) Y a^1_{\phi,j}) \end{aligned} \tag{2.5}$$

Using (2.3) & (2.5) the expression of squared voltage is given in (2.6).

$$Y = K^{-1}[R^{eq}(p^g - p^l a^0_{\phi,j}) + X^{eq}(q^g - q^l a^0_{\phi,j}) - M^{-T} M_o Y_O] \tag{2.6}$$

Where

$$\begin{aligned} R^{eq} &= -M^{-T} Z^P_D M^{-1} \\ X^{eq} &= -M^{-T} Z^q_D M^{-1} \\ K &= I_{3N} + R^{eq} diag(p^l) a^1 + X^{eq} diag(q^l) a^1 \end{aligned} \tag{2.7}$$

2.3.3 DSO-OPF for reactive power capability calculation (DSO-1)

To calculate the available VAR flexibility region F-R at the substation, we need to minimize and maximize the net VAR drawn from the substation. For a given solar generation p^g_j from an inverter, we can use the rest of the VA capacity to generate the q^g_j. Adding the q^g_j at each node algebraically, can potentially violate the D-system constraint. Hence, an OPF is formulated to minimize and maximize the net VAR injection by D-system as given in (2.8a). The objective function (2.8a) is the difference between the VAR generation and demand at the D-system node. In this OPF formulation, the solar power generation, active and reactive power demand of load, are given as input and the reactive power generation q^g_j of individual DER is the output of the optimization module. An OPF formulation is presented below [9].

$$\min_{q^g_j} \quad \sum_{i=1}^{N} q^g_j - \sum_{i=1}^{N} q^l_j \tag{2.8a}$$

$$\text{s.t.} \quad Y = K^{-1}[R^{eq}(p^g - p^l a^0) + X^{eq}(q^g - q^l a^0) + 1 v_0^2], \tag{2.8b}$$

$$\underline{y_j} \le y \le \overline{y_j}, \tag{2.8c}$$

$$p_j = p^g_j - p^l_j (a^0_j + a^1_j y_j), \tag{2.8d}$$

$$q_j = q^g_j - q^l_j (a^0_j + a^1_j y_j), \tag{2.8e}$$

$$q^{g2}_j \le S^{g2}_j - p^{g2}_j, \tag{2.8f}$$

$$v_{tm} \underline{r} \le v_0 \le v_{tm} \bar{r} \tag{2.8g}$$

The 3-phase linearized power flow formulation presented in the previous section 2.3.2 is incorporated as constraint (2.8b) in the optimization model. The upper and lower bound of each nodal voltage is set to 1.05 and 0.95, respectively, in (2.8c). Active and reactive power balance in D-system is presented in (2.8d) & (2.8e). The hardware limits of inverter-based resources are given

in (2.8f) as described in section 2.3.1. The operation of OLTC is incorporated in the optimization formulation via the tap ratio $\underline{r}, \bar{r}$ in (2.8g). The desired optimal secondary voltage can be achieved by adjusting the tap ratio for any value that lies in the decoupling range.

2.4 TSO OPF

With the obtained aggregated Q capability, the next step is to utilize the capability curve on the transmission system side, ensuring the voltage is within the allowable limit during contingency. The primary objective of the transmission-side OPF (T-OPF) is to minimize the overall generation cost while utilizing the aggregated reactive power available from DERS during normal and contingency operations.Such cases may include the normal operation with peak demand or outage of a transmission line due to a fault or the tripping of a synchronous generator, all of which can result in voltage limit violations.

To achieve this objective, the T-OPF formulation minimizes two components: (i) the total generation cost of synchronous generators, denoted as $(c(Pg))$, and (ii) the weighted sum of reactive power generation from DERs, represented by (Q_{gk}). In this study, we have articulated the usage of reactive power under a contingency scenario. Hence, a penalty factor λ, is assigned to the DER reactive power term to discourage the TSO from relying on DER capabilities during normal operating conditions. As a result, DERs are only dispatched when conventional resources alone are insufficient to restore transmission-level voltage stability. The first constraints of the T-OPF in (2.9b) are the power flow equation. The (2.9c) are branch flow limits. Equations (2.9d) to (2.9g), are voltage limits for each transmission bus i, real power generation limits for each synchronous generator g, reactive power generation limits for each synchronous generator g, and reactive power generation limits for each DSO capability k, respectively. The output of the optimization is the power dispatch for each synchronous generator g and each DSO k.

$$\min_{P_g, Q_{gk}} \quad \sum C(P_g) + \sum \lambda Q_{gk}^2 \tag{2.9a}$$

$$\text{s.t.} \quad g(x) = 0, \tag{2.9b}$$

$$h(x) \leq 0, \tag{2.9c}$$

$$Q_{gkmin} \leq Q_g k \leq Q_{gkmax}, \tag{2.9d}$$

$$Q_{gmin} \leq Q_g \leq Q_{gmax}, \tag{2.9e}$$

$$P_{min} \leq P_g \leq P_{max}, \tag{2.9f}$$

$$V_{min} \leq V_i \leq V_{max} \tag{2.9g}$$

2.5 Reactive power set point dispatch for participating DERS (DSO-2)

The final stage of the proposed approach is the dispatch of reactive power set-points to individual DERs, ensuring that the DSO can supply the reactive power requested by the TSO. In contrast to conventional DER dispatch methods, where set-points are typically allocated in proportion to available capacity, the proposed formulation incorporates a weighting factor ω_n for each DER

located at node n. This weight represents the sensitivity of the distribution substation voltage v_{tm} with respect to the reactive power injection of the DER at node n. By assigning such weights, as formulated in (2.10b), the optimization process prioritizes DERs that are electrically closer to the substation [11]. These DERs generally have a higher influence on substation voltage, and therefore their reactive power contributions are dispatched first, before utilizing other DERs further downstream in the feeder. This sensitivity-based prioritization improves the efficiency of reactive power support, as the DERs with the greatest voltage impact are scheduled first. The objective function is designed to minimize the total reactive power generation from DERs, subject to the power flow constraints specified in (2.10b)–(2.10g). In addition to these standard operational constraints, an additional constraint (2.10j) is imposed to prevent further increase in the unbalance of the distribution system. Here,α represents the maximum allowable percentage deviation from the desired unbalance limit, thereby ensuring that the dispatch does not compromise three-phase system balance. Finally, constraint (2.10h) guarantees that the aggregate DER dispatch matches the reactive power request communicated by the TSO. In this manner, the proposed formulation ensures both local operational feasibility at the distribution level and coordinated delivery of voltage support to the transmission system

$$\min_{q_g^n} \quad \sum \omega_n q_n^g \tag{2.10a}$$

$$\text{s.t.} \quad Y = K^{-1}[R^{eq}(p^g - p^l a^0) + X^{eq}(q^g - q^l a^0) + 1v_0^2], \tag{2.10b}$$

$$\underline{y_j} \le y \le \overline{y_j}, \tag{2.10c}$$

$$p_j = p_j^g - p_j^l(a_j^0 + a_j^1 y_j), \tag{2.10d}$$

$$q_j = q_j^g - q_j^l(a_j^0 + a_j^1 y_j), \tag{2.10e}$$

$$q_j^{g2} \le S_j^{g2} - p_j^{g2}, \tag{2.10f}$$

$$v_{tm}\underline{r} \le v_0 \le v_{tm}\bar{r}, \tag{2.10g}$$

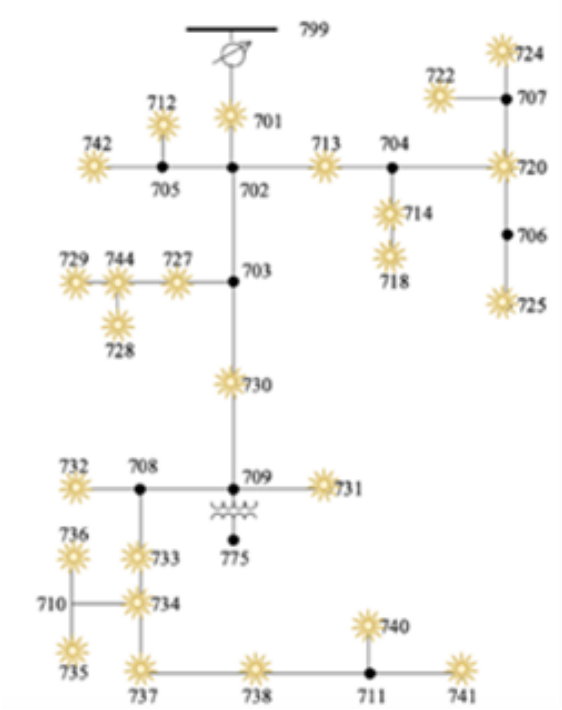
$$Q_{sub} - Q_{TSO} = 0, \tag{2.10h}$$

$$\omega_n = 1 - \frac{dV_{tm}/dq_n^g}{\sum dV_{tm}/dq_n^g}, \tag{2.10i}$$

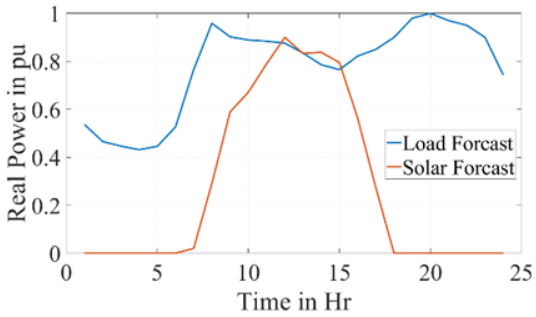
$$-\alpha q_{avg} \le q_m - q_{avg} \le \alpha q_{avg} \tag{2.10j}$$

2.6 Test case & results

IEEE 37-node 3-phase unbalanced distribution system with 3.5 MW demand is considered. Solar generation penetration is considered as 90% of the peak load. The DERs are connected to all nodes. The Normalized Daily load profile and solar PV generation profile is considered as shown in Fig. 2.3. Using the OPF day-ahead capability curves for the next 24 hours, is constructed as shown in Fig. 2.4. The reactive power requirement of the distribution system without any reactive power support from DERS is marked as a baseline. The shaded region in the Fig. 2.4 shows the flexibility in the reactive power that can be obtained with appropriate control of the DERs. It can be observed that as the DERs generate real power, the value for possible reactive power generation decreases, showing a minimum flexibility during peak PV generation.



(a) IEEE 37 node distribution system



(b) Normalized daily load profile and solar PV generation profile

Figure 2.3: (a) IEEE 37 node distribution system, (b) Normalized daily load profile and solar PV generation profile

IEEE 9-bus T-system connected to several IEEE 37-node D-systems is used for the proposed T&D coordination studies. as we replace each load with multiple detailed parallel distribution systems (IEEE37 test system) connected to each load bus as shown in Fig. 2.5. For this test system, 22, 25, and 32 parallel distribution systems are connected to buses 5, 7, and 9, respectively.

The obtained aggregated Q capability is utilized in the next step on the transmission system side to ensure that the voltage is within the allowable limit during contingency. Two contingency scenarios are studied as follows

- Contingency 1: Synchronous generator at bus 2 is out of service, which occurs at t=8 hours. This scenario is simulated with: Case 1, DERs are operated at unity power factor (UPF), while in Case 2, reactive power set points for DERs are dispatched to provide reactive power support as requested by the TSO.

  After the study, the transmission system is restored with the synchronous generator at bus 2, back in service

- Contingency 2: Transmission line between bus 4 and bus 9 is out of service at t=20 hours. Similar to the previous case the contingency 2 is simulated for two cases, case 1, without any DER reactive power support, and case 2 with DER reactive power support.

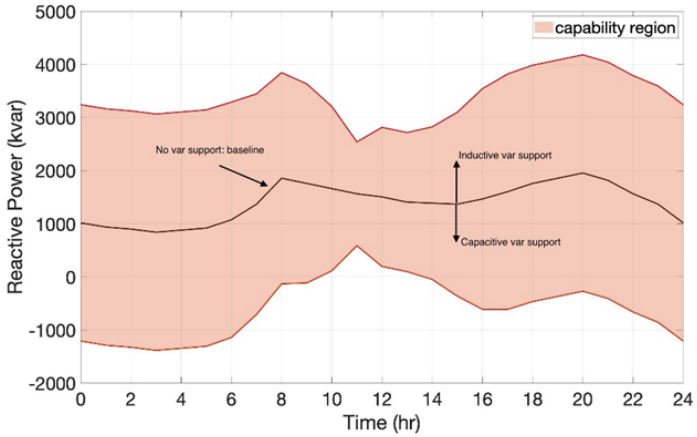


Figure 2.4: 6 Day-ahead aggregated capability curves and flexibility region of distribution

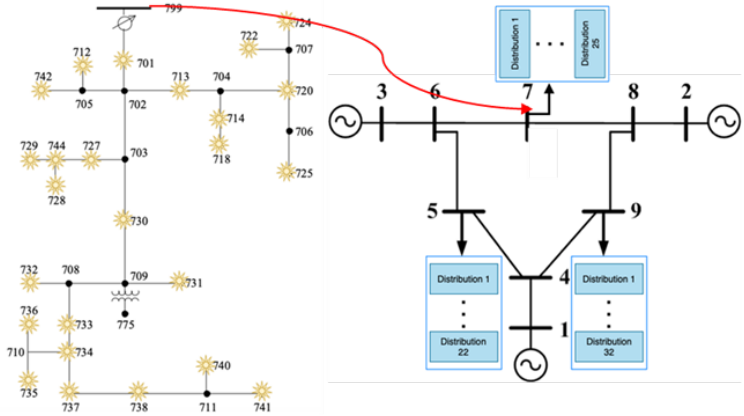


Figure 2.5: TSO-DSO test system description

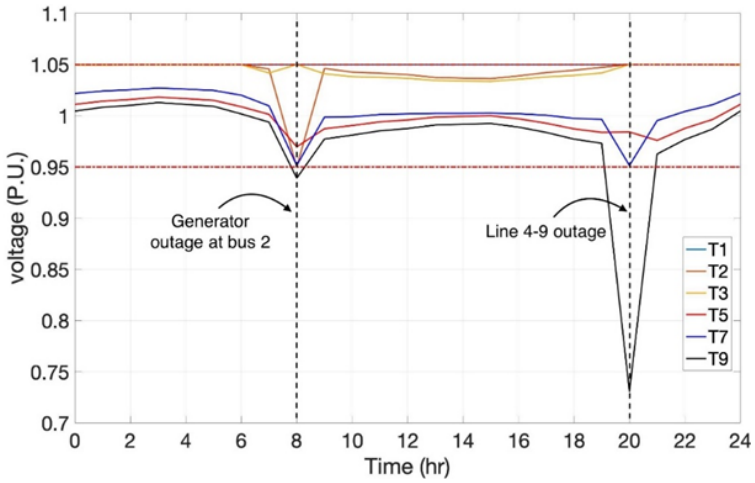


Figure 2.6: Voltage profile with reactive power support only from generators

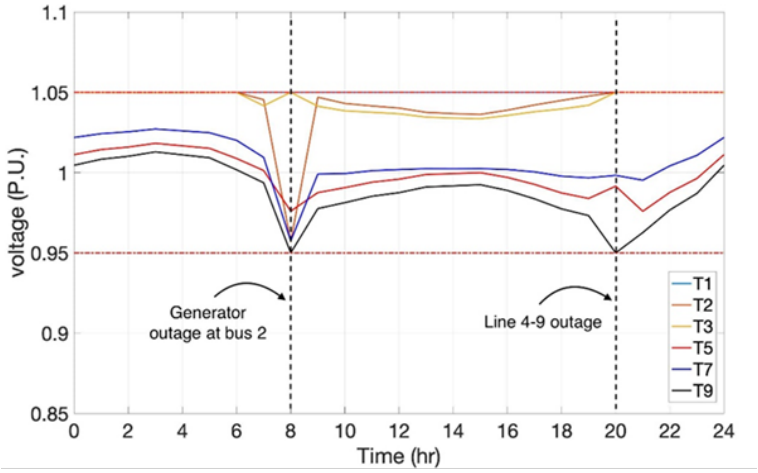


Figure 2.7: Voltage profile with reactive power support from both the generators and DER

As shown in Fig. 2.6, during both contingencies in Case 1, the transmission voltages violate the lower limit of 0.95 p.u., despite each synchronous generator having a maximum reactive power capability of 300 MVAr. This occurs because the synchronous generators are already constrained by the upper voltage limit of 1.05 p.u. At t=8 hours in Case 1, for example, the voltage at bus 9 drops below 0.95 p.u. when DERs do not contribute reactive power, illustrating the inability of transmission-side sources alone to maintain voltage stability (Fig. 2.6). In contrast, when DER flexibility is utilized (Case 2), the voltage at bus 9 remains within acceptable limits (Fig. 2.7), with a lower total reactive power requirement from synchronous generators. This reduction highlights the locational advantage of DERs, whose proximity to load buses provides more effective voltage support.

Similarly, at t=20 hours, when line 4–9 is removed, Case 1 again exhibits voltage violations, whereas in Case 2 the DERs' reactive capability curve ensures that transmission voltages remain within limits (Fig. 2.7). From the transmission OPF, the reactive power requirements during this contingency are calculated to be 66 MVAr, 46 MVAr, and 60 MVAr at load buses 2, 3, and 9, respectively. Table I further summarizes the reactive power contributions of synchronous generators and DERs for both cases, clearly demonstrating the critical role of DER flexibility in mitigating voltage violations during transmission system contingencies.

In order to realize the reactive power support identified in the transmission-level optimization, the corresponding set-points must be allocated and dispatched to the DERs situated at different locations within the distribution system. It can be observed in (2.10a) that the reactive power from DERs are weighed based on how sensitive the distribution substation voltage is to the DER reactive power generation. The weight w_n reflects the effect of reactive power change on the local and neighboring node is higher compared to the same reactive power change of a far-away node. Adding the weights in the objective function ensures that the most effective DERs respond first to TSO var request which will reduce the number of participating DERs.

The requested reactive power is dispatched with two different algorithms for line outage as shown in Fig. 2.8. It can be observed that sensitivity-aware dispatch encourages less number of DERs

Bus number	Generator Outage		Line Outage	
	Case 1	Case 2	Case 1	Case 2
1	97.4	88.5	41	35
2	0	0	159.5	66
3	75.5	69	74.5	46
5	0	0.6	0	0
7	0	5	0	10
9	0	8.7	0	60

Table 2.1: reactive power generation in different contingencies with and without DER support

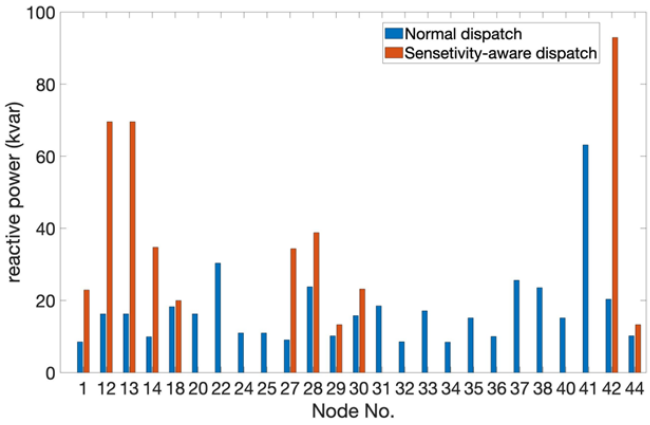


Figure 2.8: Voltage profile with reactive power support only from generators

to participate compared to the normal dispatch to provide the reactive power support required by TSO. Also, our proposed method reduces the reactive power losses. The reactive power loss is reduced from 3.94 Mvar to 3.69 Mvar using the sensitivity-aware reactive power dispatch.

2.7 Key takeaways and future work

The proposed approach utilizes the aggregated reactive power capability of the DERs to optimally dispatch these resources to rectify voltage violations during contingencies. The aggregation of reactive power from DERs is showcased on IEEE 37-node distribution systems. To utilize the reactive power capability, an IEEE 9 bus transmission system is integrated with several IEEE 37-node distribution systems. The transmission system OPF provides the optimal reactive power support required for maintaining the voltage within the allowable limit. The sensitive-aware reactive power dispatch limits the number of DERs in the distribution that support the grid during contingencies. This indirectly reduces the impact of communication issues. The sensitivity-aware reactive power dispatch can also decrease overall reactive power loss in the distribution system. From the above observations, the Key takeaway points are listed below

- A synchronous machine alone may be insufficient to maintain feasible operation during

contingencies. However, by leveraging aggregated reactive power support from DERs, these infeasibilities can be mitigated, resulting in improved voltage control. Moreover, local DER-based reactive support is often more effective than contributions from remote generators due to its proximity to the load buses.

- The sensitivity-aware reactive power dispatch can select a set of more effective DERs to provide TSO with its requested amount of reactive power, reducing the number of participating DERs. This indirectly leads to lower communication requirements and lower reactive power losses in the distribution system.

The future for the part of the work includes

- Uncertainty-aware flexibility: Extend DER flexibility characterization to explicitly incorporate uncertainties in DER output and load demand, ensuring robust and reliable system support.
- DER impact assessment under IEEE 1547 modes: Analyze the role of different IEEE 1547 operating modes to identify the most impactful DERs for reactive power and voltage control.
- Voltage stability margin (VSM) integration: Develop a coordinated T&D optimization framework with explicit VSM constraints to enhance resilience against voltage instability.

3. Data-driven and Large-Language-Model-Assisted Modeling Approaches for Deep-DER-Penetrated Distribution Systems

3.1 Introduction

As numerous DERs are being integrated into the electric transmission and distribution (T&D) systems, DER dynamics will become dominating and can no longer be ignored in system-wide transient stability analysis. Such intensive DER penetration will tremendously transform the dynamic behavior of distribution systems. In fact, the dynamics, control, and transient ride-through behavior of the existing level of DER penetration have already posed significant issues to system stability and reliability (such as the 2020 San Fernando disturbance and 2021 Odessa disturbance [12]). Transmission system planners and operators have expressed their urgent need to adequately model the dynamics of deep-DER-penetrated distribution systems, in order to ensure system-wide dynamic modeling accuracy and transient stability as required by North American Electric Reliability Corporation (NERC) Standard MOD-33. Although dynamic models for transmission systems with fossil fuel generators are well-developed, today's reduced-order dynamic models for distribution systems with massive DERs (such as the WECC composite load model [13] and the 'DER_A' model [14]) are far from adequate. These highly aggregated models are oversimplified which ignore critical dynamic model structures for accurately reproducing important dynamic voltage events (such as the oversimplified dynamic model of 1-phase motors and the ignored steady-state model of feeder-wide voltage variations in the composite load model and DER_A models, which can lead to severe misrepresentation of fault induced delayed voltage recovery (FIDVR) events [15, 16]). Such model deficiency has been identified by both NERC and Federal Energy Regulatory Commission (FERC) [17, 18].

This chapter proposes 1) a data-driven reduced-order dynamic modeling approach for accurately representing the deep-DER-penetrated distribution grids in the transmission-level transient stability assessments; 2) a large language model (LLM) based electromagnetic transient (EMT) model creation assistant for creating PSCAD EMT dynamic models toward representing accurate EMT dynamics of the deep-DER-penetrated distribution grids in the transmission-level transient stability assessments; and 3) a smart field data collection and model updating tool for DER-penetrated distribution power systems.

3.2 Data-driven reduced-order dynamic modeling approach for deep-DER-penetrated distribution grids

As illustrated in Fig. 3.1, in existing transient stability assessments of bulk power systems, the entire distribution grid with numerous dynamic loads and DERs are aggregated as one single dynamic load model at the substation (i.e., the WECC composite load model [13] and the 'DER_A' model [14]). These highly aggregated models are shown to be oversimplified, which can misrepresent the critical impact of massive DERs and dynamic motor loads on the bulk power system dynamic performance [15–18]. For instance, the performance-based single-phase motor model and the ignorance of distribution grid topology and feeder-wide voltage variations in WECC composite load model has been well known to misrepresent the fault-induced delayed voltage recovery

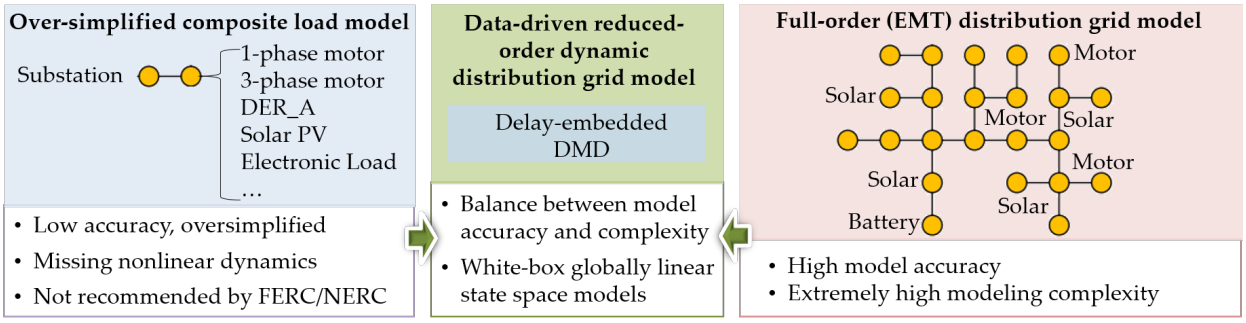


Figure 3.1: Overview of the proposed data-driven reduced-order dynamic modeling approach.

(FIDVR) events [15,16]; and the recently-developed DER_A model, although with lots of adjustable parameters, is only benchmarked against the positive-sequence dynamics (instead of the detailed EMT dynamics) of the full-order distribution grid models (i.e., the OpenDSS models) [19,20]. As recommended by FERC and NERC [17,18], these oversimplified dynamic load models need significant improvements in order to accommodate future distribution grids with deep DER penetration. As fast inverter dynamics will become dominating in future deep-DER-penetrated distribution grids, whether existing positive-sequence dynamic models will be adequate for capturing critical DER inverter dynamics remains an open question. In future carbon-neutral power systems with tremendous DERs and limited fossil fuel generators, the major sources of system dynamics will switch from conventional generators in transmission systems to DERs in distribution systems. Under these future scenarios, today's oversimplified dynamic models for the future distribution systems with extremely high DER penetration could significantly degrade the accuracy and trustworthiness of power system planning and operation outcomes, which will eventually damage the reliability of bulk power systems.

We propose a data-driven reduced-order dynamic modeling approach for deep-DER-penetrated distribution grids. The approach utilizes recently developed theoretical and computational tools in Koopman operator and delay-embeded dynamic mode decomposition (DMD) toward creating reduced-order dynamic models for deep-DER-penetrated distribution grids, which can 1) properly balance the modeling accuracy and modeling complexity; 2) identify reduced-order dynamic models with partial observations; 3) maintain physical interpretability by identifying a globally linear state space dynamic model.

3.2.1 Related work

Existing dynamic modeling efforts (see Fig. 3.1) for deep-DER-penetrated distribution grids can be categorized into: 1) detailed EMT-based distribution grid dynamic modeling and T&D hybrid co-simulations; 2) oversimplified composite load models with DER_A models; 3) learning-based black/grey-box models.

EMT models: These are the most accurate ways of modeling the DER-penetrated distribution grid dynamics, which can be integrated into the transmission system transient stability studies via T&D hybrid co-simulations [21,22]. However, these EMT models are of extremely high modeling and

computation complexities, which makes it difficult for utilities and system operators to adopt these models and the corresponding T&D hybrid simulation platforms.

Composite load models: These are the most commonly used positive-sequence reduced-order dynamic models for DER-penetrated distribution grids, which aggregate the entire distribution grid dynamics as a single composite load at the substation [13, 14]. Although computationally efficient, these oversimplified models suffer from well-known structural deficiencies (for single-phase motor dynamics, fast DER inverter dynamics, etc.) which prevent them from accurately reproducing critical system instabilities (such as FIDVR, fast inverter control instabilities, etc.) [15, 16, 19, 20].

Data-driven models: These models learn the input-output dynamics of an entire distribution grid from measurements or simulation data, and represent these learned dynamics by certain black-box or grey-box models (such as neural networks (NNs)) [23–26]. Unlike the above two types of white-box models which are based on physical governing equations, these learning-based black-box or grey-box models typically lack physical interpretability, which can significantly limit their real-world applicability.

3.2.2 Overview of proposed framework

This section introduces our framework for identifying a globally linear dynamic model for the nonlinear dynamics of DER-penetrated distribution power systems. Based on the theory of Koopman operator, any finite-dimension nonlinear dynamic system can be projected to an infinite dimension space via Koopman operator where its dynamic can be represented by a globally linear dynamic model. However, several technical difficulties exist in applying the above Koopman operator theory toward numerically identifying the globally linear dynamic model for DER-penetrated distribution power systems: 1) while Koopman operator provides a theoretical framework for developing globally linear dynamic models of nonlinear dynamic systems, the developed globally linear dynamic model is infinite-dimensional, which is numerically difficult to be achieved and requires a finite-dimension approximation; 2) the Koopman operator theory requires the underlying nonlinear dynamic system to be fully observable, while the DER-penetrated distribution power grid is typically only partially observable; 3) the Koopman operator theory does not provide an effective approach of finding the appropriate mapping to project the finite-dimension nonlinear dynamic system to the infinite dimension space where a globally linear dynamic model exists.

In order to address the above technical difficulties, in the following sections, we propose 1) delayed embedding to recover full-order nonlinear dynamics from partially observed nonlinear distribution power systems and to project the finite-dimension nonlinear dynamics onto a higher-dimension space with close-to-globally-linear dynamics; and 2) dynamic mode decomposition (DMD) for identifying globally linear dynamic models of the nonlinear distribution power systems. Fig. 3.2 shows an overview of the proposed framework.

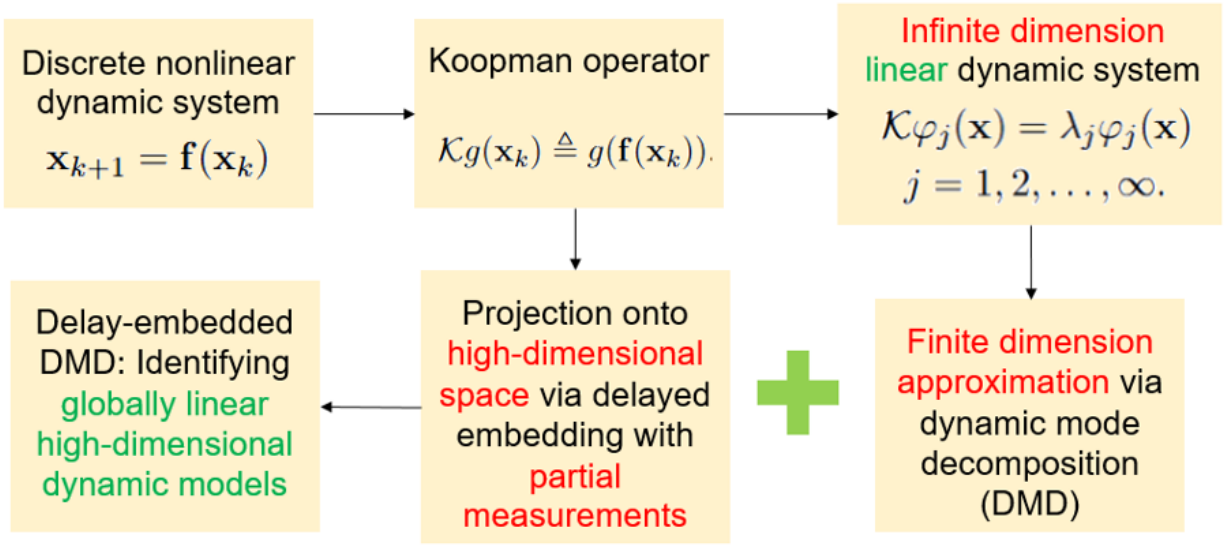


Figure 3.2: Overview of the proposed technical framework.

3.2.3 Formulation of the data-driven model identification problem

Mathematically, the problem of identifying a (discrete) dynamic model from measurement data can be formulated as follows. Let $x(t)$ be the m dimensional time-dependent state vector evaluated at time t. The discrete nonlinear dynamics for the state vector can be represented as:

$$x(t+1) = f(x(t)) \tag{3.1}$$

where f is a nonlinear function governing the nonlinear dynamics of the m dimensional system. Let y be the d dimensional noisy measurements of the system. The nonlinear mapping g between the measurement vector $y(t)$ and the state vector $x(t)$ is given by:

$$y(t) = g(x(t)) + e \tag{3.2}$$

where e is the noise process. The goal is to learn an approximate dynamic system

$$z(t) = \hat{f}(z(t)) \tag{3.3}$$

where $z(t)$ is the new state vector for the approximate dynamic system, which can be a function of the measurement vector $y(t)$:

$$z(t) = \phi(y(t)) \tag{3.4}$$

If the original state vector $x(t)$ is fully observable, then $y(t) = x(t)$ and $z(t) = y(t)$. However, for DER-penetrated distribution power grids, the state vector $x(t)$ is only partially observable (or cannot be directly observed). Therefore, dimension $d < m$.

3.2.4 Delayed embedding for partially observed distribution systems

Time delay embedding (i.e., delayed embedding) is the process of including historical measurements $y(t-1), \cdots, y(t-k)$ into the modeling of nonlinear dynamic systems. According to Takens embedding theorem, by introducing a certain number of historical measurements into the modeling of a partially observed nonlinear dynamic system using the delayed embedding, one can fully reconstruct the full-order nonlinear dynamics of the original system on the projected delay-embedded measurement space. For a particular measurement time series y, the delay-embedded state variable h can be assembled into the following Hankel matrix H.

$$H = \begin{bmatrix} y(t_1) & y(t_2) & \cdots & y(t_q) \\ y(t_2) & y(t_3) & \cdots & y(t_{q+1}) \\ \vdots & \vdots & \ddots & \vdots \\ y(t_n) & y(t_{n+1}) & \cdots & y(t_{n+q+1}) \end{bmatrix} = \begin{bmatrix} h_1, & h_2, & \cdots, & h_q \end{bmatrix} \tag{3.5}$$

where h_i $(i = 1, 2, \cdots, q)$ is the n dimension delay-embedded state vector h evaluated at time i.

Based on Takens embedding theorem, if the embedding dimension $n > 2m$, then the reconstruction of the full-order dynamics of the original nonlinear system $f(x(t))$ can be guaranteed on the new delay-embedded space with delay-embedded vector h. Furthermore, when the embedding dimension $n \gg 2m$, as $n \to \infty$, the reconstructed dynamics in the delay-embeded space with delay-embedded vector h tend to be globally linear. This provides a straightforward way for defining the mapping to project the original finite-dimension nonlinear dynamic system to the infinite dimension space where a globally linear dynamic model can be discovered based on the Koopman operator theory.

3.2.5 Dynamic mode decomposition (DMD) for reduced-order globally linear dynamic modeling

Once the n $(n \gg 2m)$ dimensional delay-embedded state vector h is constructed via the above Hankel matrix H, the infinite dimension space where a globally linear dynamic model can be discovered can be numerically approximated by the finite n $(n \gg 2m)$ dimension space where the projected system dynamics can be approximately globally linear:

$$h(t) \approx Ah(t-1) \tag{3.6}$$

where $h(t)$ is the n dimension delay-embedded state vector; A is the state matrix of the approximately globally linear dynamic system.

This section applies DMD to identify the reduced order state matrix $\tilde{A}$ which can represent the reduced-order globally linear dynamic model in the delay-embeded state space for the original nonlinear dynamic system in the original state space. Let $H(t)$ and $H(t-1)$ be constructed from the historical measurements y via the Hankel matrix H. Based on DMD, the reduced-order approximation of the state matrix A can be constructed via the truncated singular value decomposition of the Hankel matrix H:

$$\tilde{A} = \tilde{U}H(t)\tilde{V}\tilde{\Sigma^{-1}} \tag{3.7}$$

$$H(t-1) = \tilde{U}\tilde{\Sigma}\tilde{V}^{*} \tag{3.8}$$

The reduced-order globally linear dynamic model can then be described as:

$$\tilde{x}(t+1) = \tilde{A}\tilde{x}(t) \tag{3.9}$$

By examining the eigenvalues and eigenvectors of matrix $\tilde{A}$, one can study the stability of the original nonlinear dynamic systems via its global linearization. By reconstructing the original nonlinear measurements y via the inverse process of Hankel matrix construction, one can reconstruct the nonlinear dynamics of the original nonlinear system from its corresponding globally linear dynamics in the delay-embedded space.

3.2.6 Case studies

The proposed approach is tested on an integrated transmission-distribution system with a DER-penetrated IEEE 13-bus distribution test feeder connected to Bus 18 of the IEEE 39-bus transmission test system. The training data contains 20 training cases (i.e., faults applied at 20 different locations in the transmission system) which collect the voltage magnitude, current magnitude, real power, and reactive power measurements at the point of interconnection (POI) between the transmission and distribution systems. Fig. 3.3 shows the test system and the fault locations.

To verify the performance of the identified globally linear dynamic model, two testing scenarios and two fault locations are used as the test cases. These test cases are different from the training cases used for identifying the dynamic model. For each test case, the simulation data (i.e., voltage magnitude, current magnitude, real power, and reactive power measurements at the POI) obtained from the original distribution system and those obtained from the identified data-driven model are compared. As we only collect measurements from the POI bus of the distribution system, the underlying nonlinear dynamic model of this distribution system is not fully observed. The simulation time step is set to be 0.01 sec.

For Testing Scenario 1, we consider the distribution system has 0% DER penetration and 30% single-phase induction motor penetration, for which a transient fault is applied at Bus 2 of the IEEE

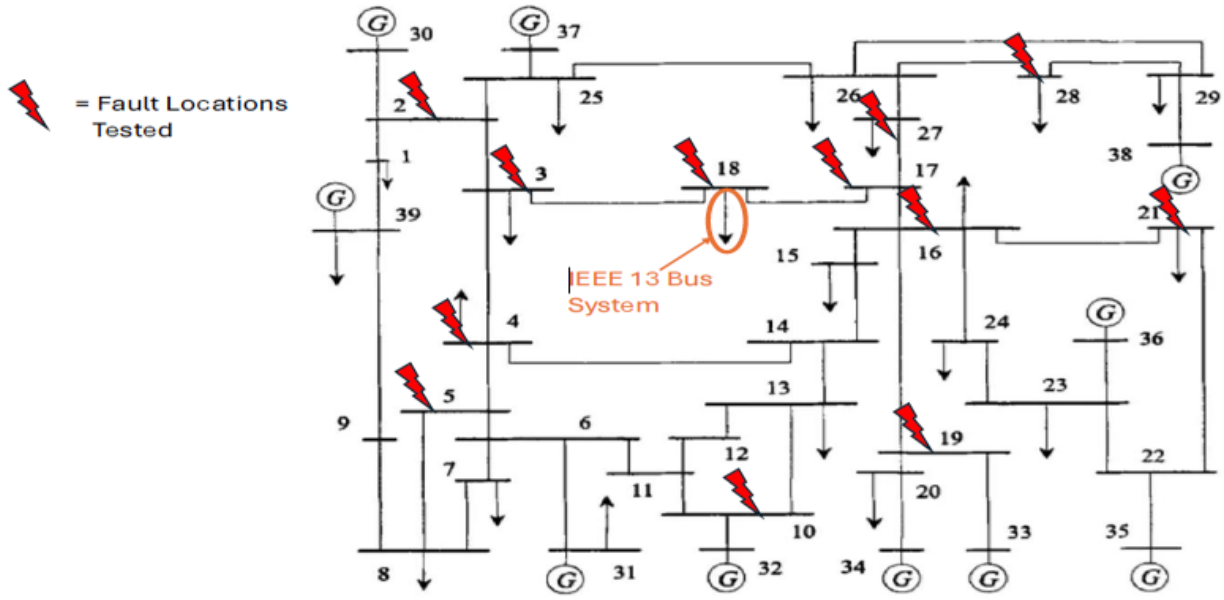


Figure 3.3: Integrated transmission-distribution test system and fault locations.

39-bus transmission system. There is no fault induced delayed voltage recovery (FIDVR) happening in this testing scenario. The Hankel dimension (i.e., the dimension of the delay-embedded state vector h) $n = 350$. Fig. 3.4 shows the comparison between the true POI measurements (i.e., voltage magnitude, current magnitude, real power, reactive power) and the POI measurements reconstructed from the globally linear dynamic model identified by using the historical POI measurements. It is clear that the reconstructed POI measurements align closely with the true POI measurements, which indicates the data-driven globally linear dynamic model is of high accuracy even if the model is identified only with partial observations.

For Testing Scenario 2, we consider the distribution system has 0% DER penetration and 30% single-phase induction motor penetration, for which a transient fault is applied at Bus 3 of the IEEE 39-bus transmission system. FIDVR is observed in this testing scenario. The Hankel dimension (i.e., the dimension of the delay-embedded state vector h) $n = 350$. Fig. 3.5 shows the comparison between the true POI measurements (i.e., voltage magnitude, current magnitude, real power, reactive power) and the POI measurements reconstructed from the globally linear dynamic model identified by using the historical POI measurements. It is clear that, with FIDVR, the reconstructed POI measurements align closely with the true POI measurements, which indicates the data-driven globally linear dynamic model is of high accuracy even if the model is identified only with partial observations.

For Testing Scenario 3, we consider the distribution system has 50% DER penetration and 30% single-phase induction motor penetration, for which a transient fault is applied at Bus 2 of the IEEE 39-bus transmission system. There is no fault FIDVR happening in this testing scenario. The Hankel dimension (i.e., the dimension of the delay-embedded state vector h) $n = 700$. Fig. 3.6 shows the comparison between the true POI measurements (i.e., voltage magnitude, current magnitude, real power, reactive power) and the POI measurements reconstructed from the globally linear

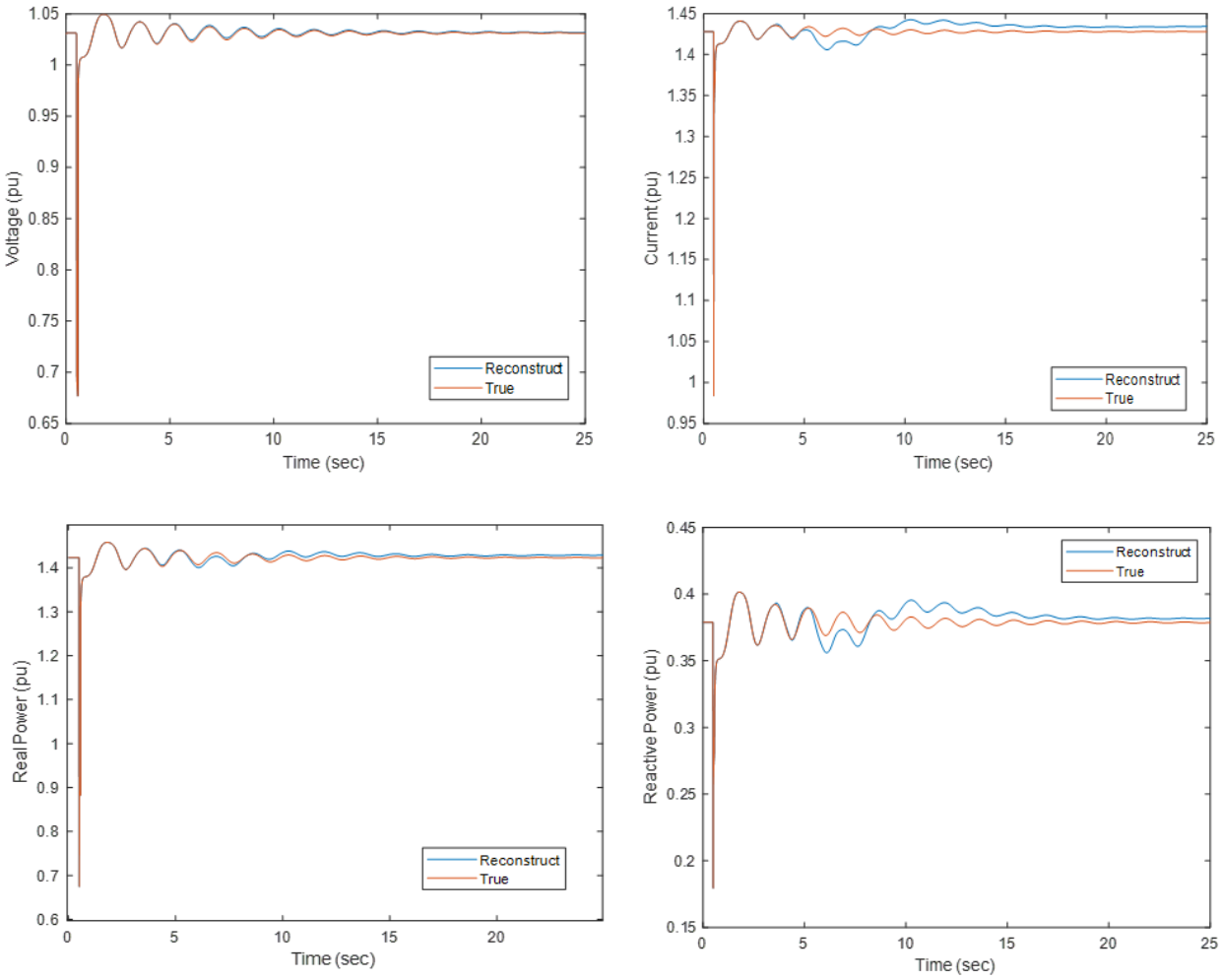


Figure 3.4: Test results for Scenario 1.

dynamic model identified by using the historical POI measurements. It is clear that, with 50% DER penetration, the reconstructed POI measurements align closely with the true POI measurements, which indicates the data-driven globally linear dynamic model is of high accuracy even if the model is identified only with partial observations.

For Testing Scenario 4, we consider the distribution system has 50% DER penetration and 30% single-phase induction motor penetration, for which a transient fault is applied at Bus 3 of the IEEE 39-bus transmission system. FIDVR is observed in this testing scenario. The Hankel dimension (i.e., the dimension of the delay-embedded state vector h) $n = 700$. Fig. 3.7 shows the comparison between the true POI measurements (i.e., voltage magnitude, current magnitude, real power, reactive power) and the POI measurements reconstructed from the globally linear dynamic model identified by using the historical POI measurements. It is clear that, with 50% DER penetration and FIDVR, the reconstructed POI measurements align closely with the true POI measurements, which indicates the data-driven globally linear dynamic model is of high accuracy even if the model is identified only with partial observations.

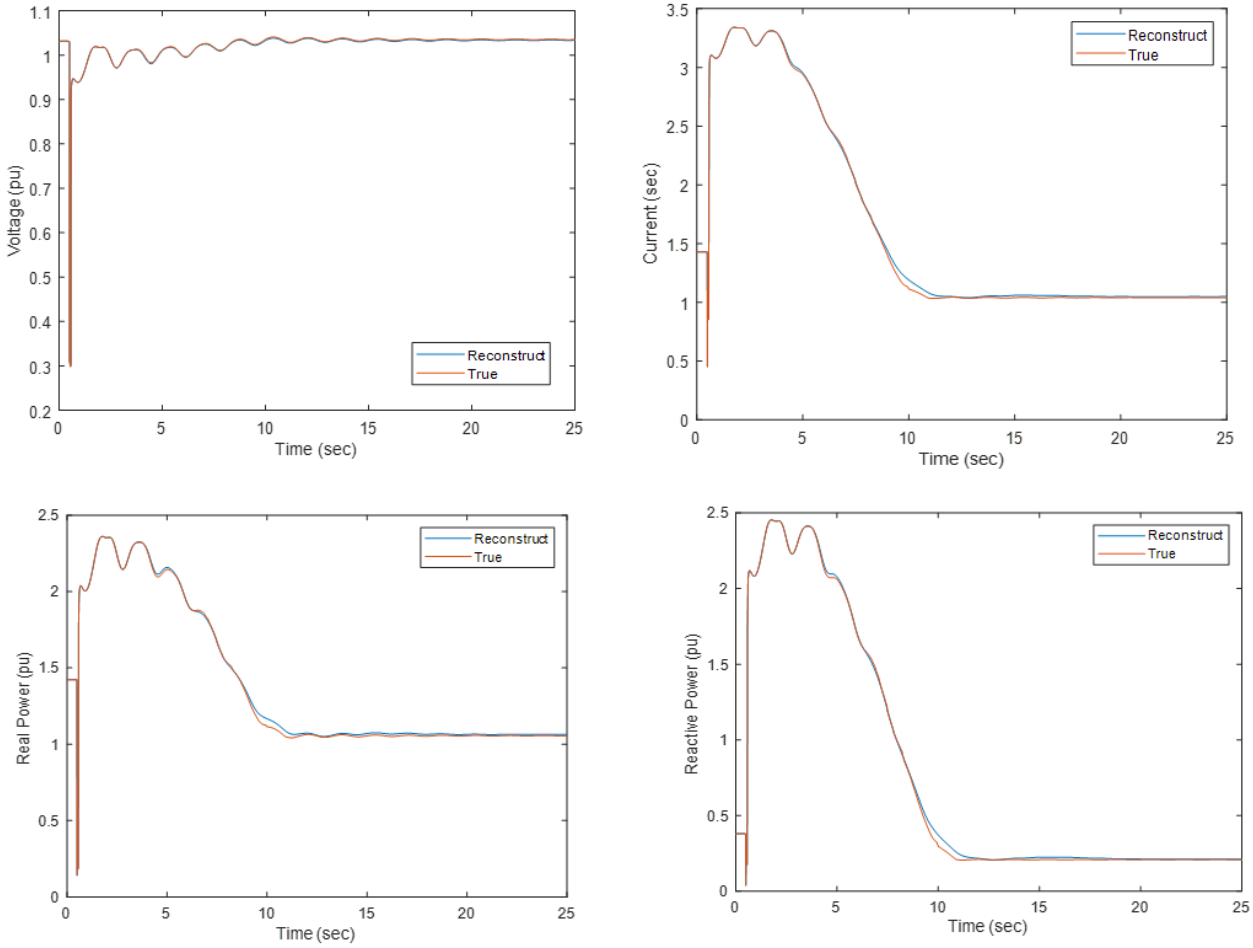


Figure 3.5: Test results for Scenario 2.

3.3 LLM-based EMT model creation assistant for deep-DER-penetrated distribution grids

As the power industry starts to widely adopt EMT dynamic models and and PSCAD EMT simulations for systems with DERs and inverter-based resources (IBRs), the power industry practitioners has spent significant efforts in creating PSCAD EMT dynamic models, performing PSCAD EMT simulations, and training power engineers for PSCAD EMT dynamic modeling and simulations. To reduce the engineering time for manually creating PSCAD EMT dynamic models and running PSCAD EMT dynamic simulations as well as effectively training power engineers toward adopting PSCAD EMT dynamic modeling and simulations, this section develops a LLM-based PSCAD EMT model creation and simulation assistant, which allows a fine-tuned application-specific LLM to generate PSCAD Python automation scripts toward building PSCAD EMT models and running simulations. Fig. 3.8 shows the overview of the proposed LLM-based PSCAD EMT assistant.

3.3.1 Related work

While the general-purpose LLMs (e.g., ChatGPT, Llama, etc.) can understand the general workflow for PSCAD to build EMT models and run simulations with Python scripts, and can generate PSCAD

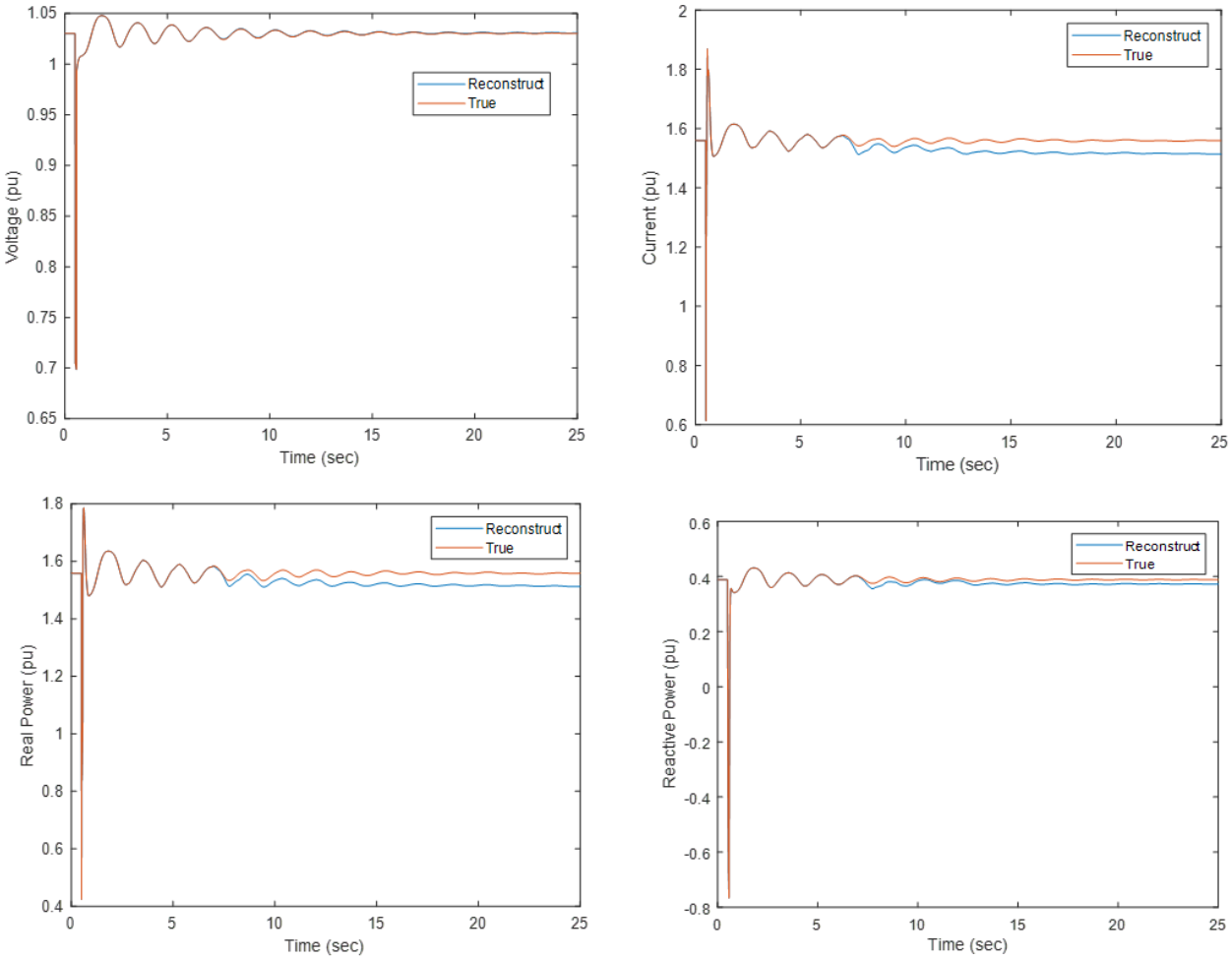


Figure 3.6: Test results for Scenario 3.

Python automation scripts for this workflow, the Python scripts generated by general-purpose LLMs contain lots of fake information (i.e., Python libraries, functions, and grammars that do not exist) due to hallucinations of these LLMs. These fake Python scripts cannot be executed and cannot be used to train power engineers on the correct usage of the PSCAD Python automation libraries for EMT modeling and simulation. Fig. 3.9 shows the fake PSCAD Python script generated by the general-purpose ChatGPT, with Python libraries, functions, and grammars that do not exist.

3.3.2 Fine-tuning LLM as the PSCAD modeling and simulation assistant

We adopt the flowchat shown in Fig.3.10 for fine-tuning Llama toward building the PSCAD modeling and simulation assistant, an open-source general-purpose LLM developed by Meta. The entire fine-tune process contains three phases: data collection, data processing, and fine tuning. During data collection and data processing, we will collect both sensitive industry data and public data. For the sensitive industry data, we manually mask the confidential information. For the publia data, we collect open-access/synthetic power system transient simulation models, PSCAD user manuals, and the source codes of the PSCAD Python automation library. The transient

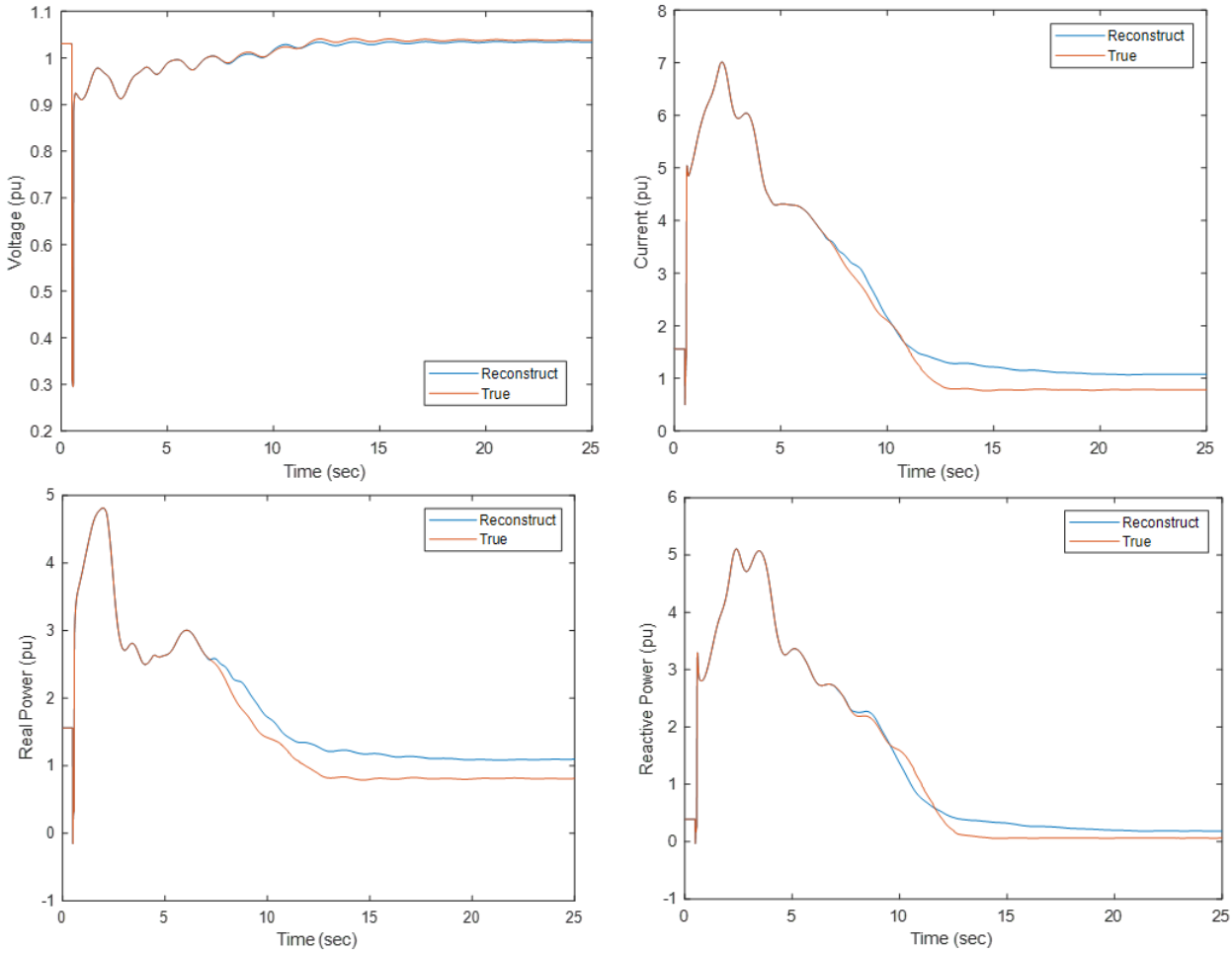


Figure 3.7: Test results for Scenario 4.

simulation models (in PSSE format) are then converted to PSCAD EMT models via E-TRAN. The PSCAD Python scripts for building these PSCAD EMT models are manually recorded via PSCAD's build-in function for recording Python scripts. The final training dataset contains training data in the formats of .txt files converted from the .pdf user manuals as well as Python scripts and source codes. These training data are then organized into the structured JSON data format with paired instruction-code datasets. The fine-tuning process then collects these structured JSON data files and adopts both parameter-efficient fine tuning (i.e., LoRA and QLorA) as well as full fine tuning to train the fine-tuned LLM.

3.3.3 Case studies

In the case studies, we fine tune the Meta Llama 3 70B model on a server with NVIDIA 4090 GPUs. The training time is 35 hour for a full fine tuning process. Fig. 3.11 shows the PSCAD Python script generated by the fine-tuned Llama model for an inquiry of "building a distribution system in PSCAD with 1 feeder, 1 substation, 3 nodes. Each node has 1 solar panel, 1 single-phase motor, 1 battery storage". Unlike the script in Fig. 3.9 which contains lots of fake information and cannot

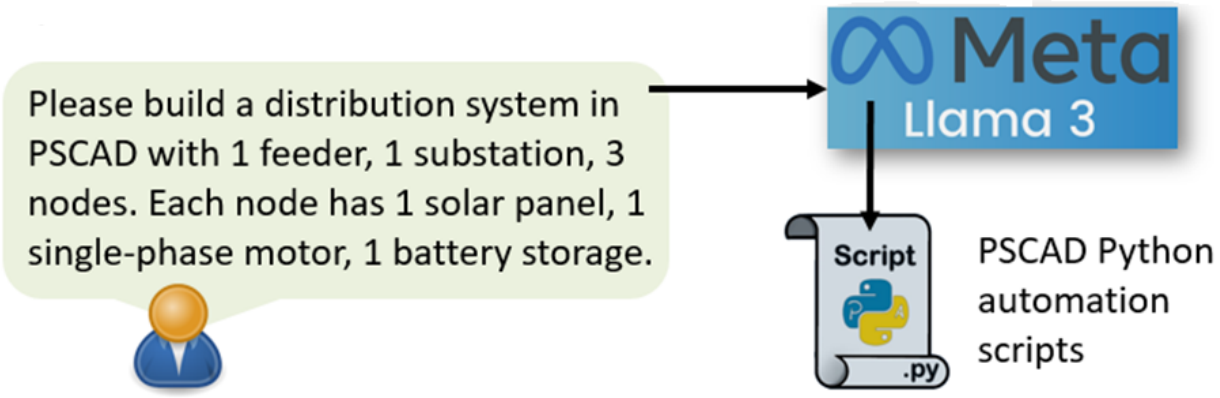


Figure 3.8: Overview of the LLM-based PSCAD EMT assistant.

be executed, this script uses the correct PSCAD Python library, functions, and grammars, resulting in a script which can be executed in PSCAD with minor revisions (i.e., adding the file name/path for saving the developed EMT model and adding the x-y coordinates for each component in this EMT model).

3.4 Smart field data collection and model updating tool for DER-penetrated distribution power systems

As massive distributed energy resources (DERs) are integrated into distribution power systems, utilities face challenges in accurately modeling their networks to ensure the visibility and controllability of their DERs [27]. A common solution is to integrate asset management software and geographic information systems (GIS) [28] [29] [30]. Using Internet of Things (IoT) and smart technologies, this allows them to document, maintain, and service equipment in a timely and accurate manner. However, these software solutions focus primarily on asset, inventory, and work order management and do not provide a way to streamline distribution system modeling that is useful to utility operators and planners.

3.4.1 Summary of contribution

This paper introduces a software prototype developed by a team of undergraduate students at Arizona State University, GridScout, which allows utility workers to use a mobile application on their mobile devices to scan a quick response (QR) code of the electrical equipment during new equipment installation, replacement of existing equipment, and routine equipment maintenance. Scanning the QR code will automatically 1) capture the location data of the equipment under installation, replacement, or maintenance via the Global Positioning System (GPS); and 2) link the equipment with its nameplate parameters stored in a central database. The GPS-based location data and the nameplate parameters will then be linked to the central database and update the OpenDSS-based distribution system model [31] in real time (i.e., during the installation, replacement, or maintenance process of the equipment). A Python script is created which can be run locally to automatically produce OpenDSS simulation models and power flows. Such a data collection and

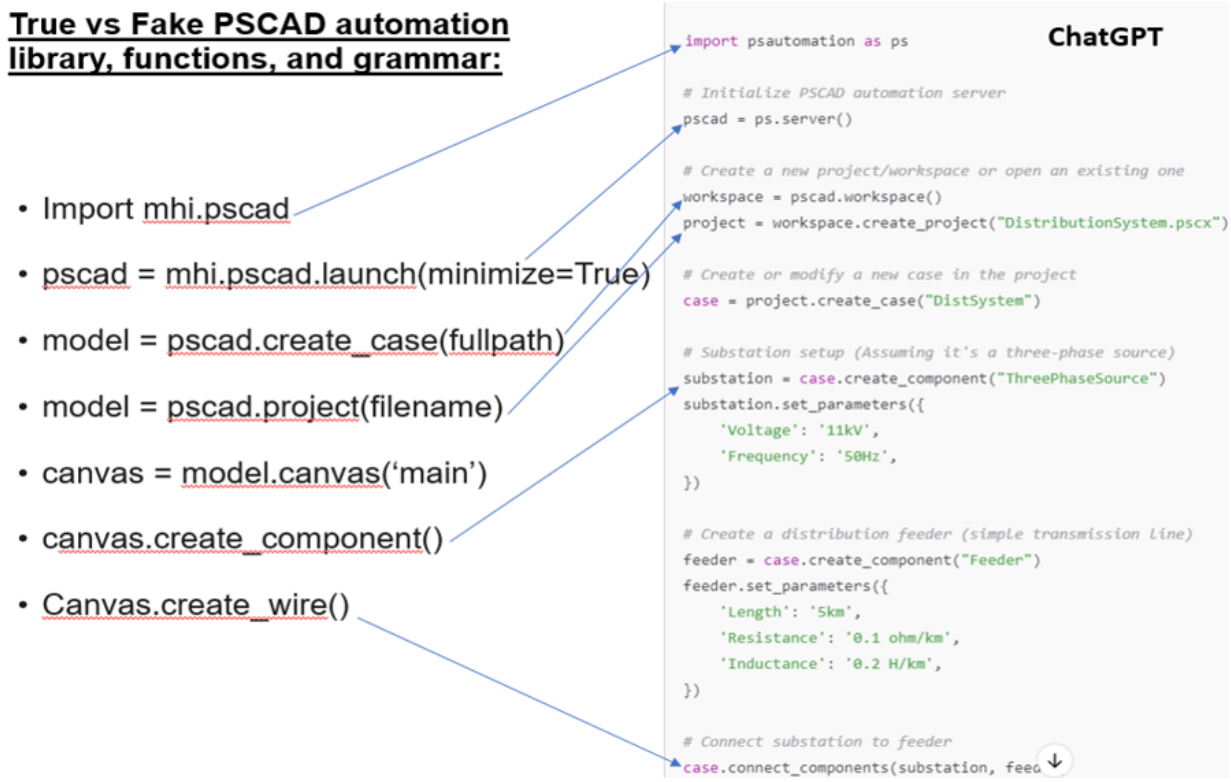


Figure 3.9: Fake PSCAD Python script generated by the general-purpose ChatGPT.

modeling software tool can best ensure distribution system modeling accuracy and reduce the engineering time for creating and updating distribution system models.

3.4.2 Related work

Although existing technologies share certain aspects of GridScout's functionality, to our best knowledge, no existing work combines all the features into one integrated system specifically designed for distribution system model creation and updating during field operations. This positions GridScout as potentially filling a unique niche in the market.

OpenGridMap: OpenGridMap [32] is an open-source project focused on mapping electrical grids using crowd-sourced data. It allows users to contribute information about grid components such as transformers, power lines, and substations, in order to build an open-source map of these electrical infrastructures. However, it does not offer any asset management solution and field data collection that GridScout aims for, such as work order tracking and real-time geolocation integration.

Integrated power system simulation tools: Some existing simulation software solutions integrate with OpenDSS for batch power system modeling and simulations, but these integrations often rely on manual data collection or data imported from other software platforms. Tools such as Cyme [33], DIgSILENT PowerFactory [34], or GridLAB-D [35] offer similar simulation capabilities, but do not automate the field data collection and real-time system model updates that GridScout aims to

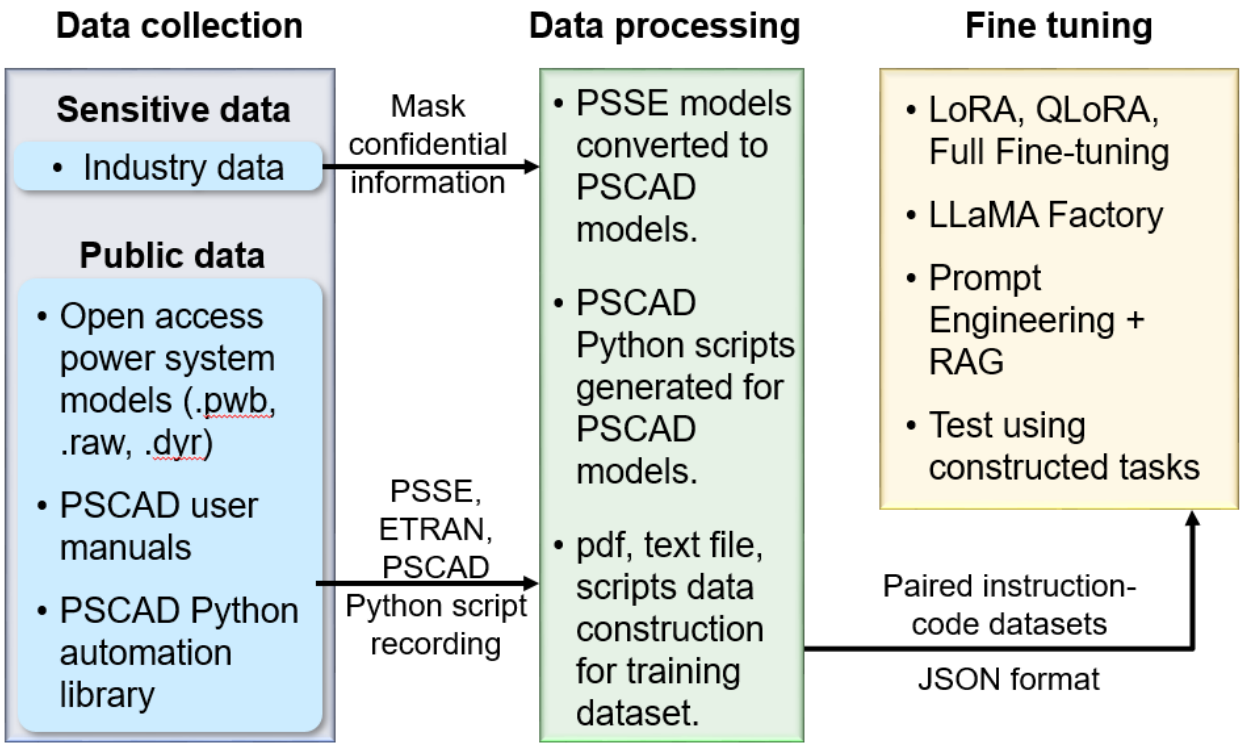


Figure 3.10: Flowchart of fine-tuning Llama for building the PSCAD modeling and simulation assistant.

achieve.

QR codes for asset tracking: Several existing technologies utilize QR codes to track physical assets [36, 37]. Some microgrid developers adopt in-house developed software to map and track the equipment in their microgrids during installation [38]. However, none of these technologies have been integrated into a holistic solution and applied to automate general distribution system field data collection and system model update/creation.

3.4.3 Overview of the software application

Figure 3.12 outlines the general application flow for integrating GridScout into the utilities' existing equipment installation, replacement, maintenance, and system modeling process. The GridScout software manages utility's data and models in three phases: the warehouse phase, the field phase, and the office phase. This allows GridScout to streamline the entire process starting from the creation of a work order for equipment installation, replacement, and maintenance, all the way to field equipment services and distribution system model creation.

```
import mhi.pscad
import os
import math

# Folder path and project name
    filename =
    fullpath =
# Launch PSCAD
    pscad = mhi.pscad.launch(minimize=True)

# Create a new project and canvas setting in the folder
    model = pscad.create_case(fullpath)
    model = pscad.project(filename)
    model.navigae_to()
    model.parameters(time_duration = '10.0')
    model.parameters(time_step = '50.0')
    model.parameters(sample_step = '50.0')
    canvas = model.canvas('Main')
    canvas.parameters(size = '5')

# Create bus
    bus_1 = canvas.create_bus((0,1),(9,1))
    bus_1.location = (X1,Y1)
    bus_1.parameters(['1','BUS_A1_138000','BUS_A1_138000','138','10','20'])
    node_1 = canvas.create_component('master:nodelabel',)
    node_1.location(X1+4,Y1)

    bus_2 = canvas.create_bus((0,1),(9,1))
    bus_2.location = (X2,Y2)
    bus_2.parameters(['1','BUS_A1_138000','BUS_A1_138000','138','10','20'])
    node_2 = canvas.create_component('master:nodelabel',)
    node_2.location(X2+4,Y2)
```

Figure 3.11: PSCAD Python script generated by the fine-tuned Llama model.

The warehouse phase

GridScout's entire process starts in the warehouse where a job number or work order is created for a new installation, replacement, or maintenance task of certain equipment (transformers, lines, capacitors, etc.). Based on the work order, the equipment is pulled from inventory.

Each equipment is assigned a unique QR code containing the serial numbers of the equipment. These serial numbers are used to link the particular equipment to its nameplate parameters stored in a central database. The QR code is then printed and affixed to the equipment before the equipment is deployed to the field.

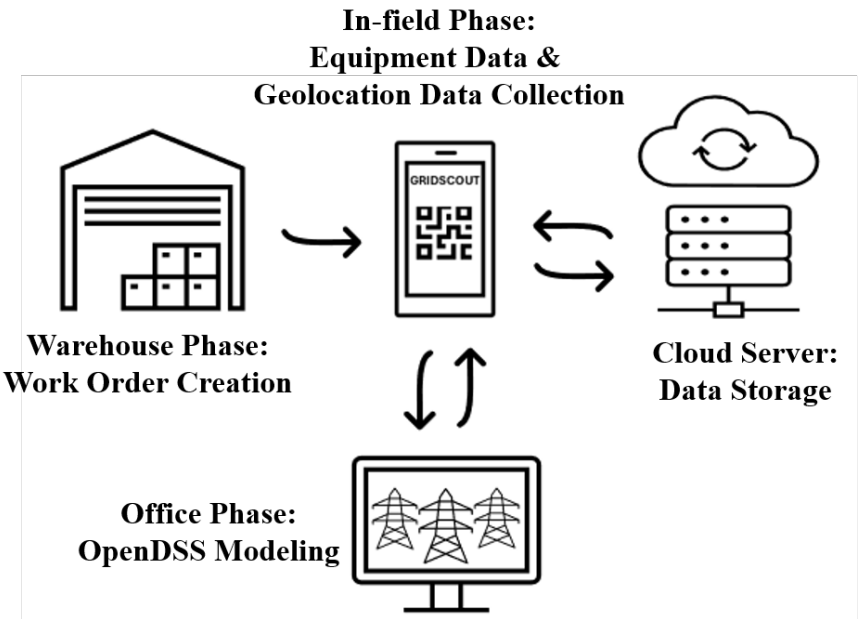


Figure 3.12: The application flow for integrating GridScout into utility practices.

The field phase

Once in the field, utility technicians use the GridScout's mobile application to scan the QR code on the equipment. The mobile application collects the geolocation data along with the scanned equipment serial number. This information is then sent to the central database hosted on a server, and the serial number is used to fetch the equipment nameplate parameters pre-stored in the central database when placing the purchasing order for the equipment.

A confirmation notification is sent back to the mobile application, notifying the field technician of a successful data update, allowing them to proceed with their installation, replacement, or maintenance tasks confidently.

The office phase

The updated equipment data (nameplate parameters and geolocation data) in the central database is then used to update the distribution grid circuit model in OpenDSS. Engineers in the office review the updated circuit model on the server to ensure it accurately reflects the latest field data. The updated model is then used for simulations to analyze load flow, fault detection, system optimization, etc.

The above updated equipment data and OpenDSS model are then used by the office team to further create various uncontrolled copies of models which are used for creating various simulation test cases for internal studies as well as controlled copies of models which are used for real-time operation and control of the distribution grid.

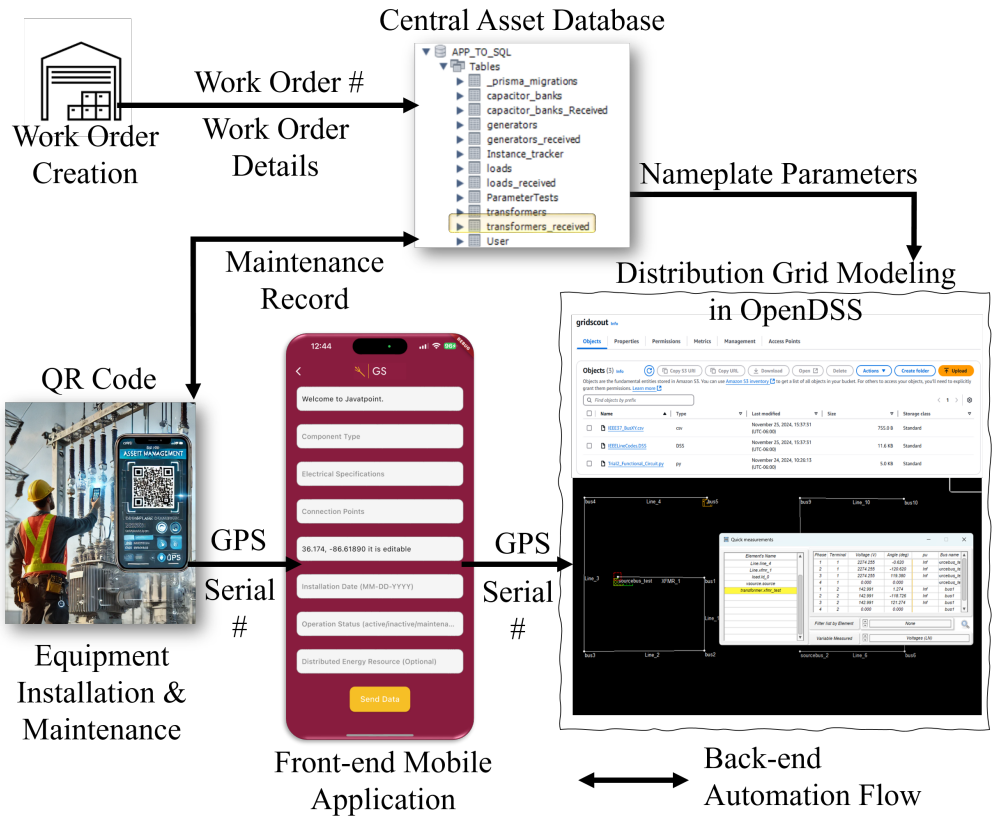


Figure 3.13: Overall software design flow.

Database administrators review the changes in the central database, ensuring that all the component life cycle information such as serial numbers, dates of installation, replacement, maintenance, and field service logs/details are properly recorded.

3.4.4 Software implementation

The Gridscout software is designed and implemented in four modules: 1) the front-end module which contains a mobile application for field data collection; 2) the central database which stores all the related data; 3) the back-end automation module which streamlines the entire data collection, data storage, and model creation process; 4) the OpenDSS modeling module which creates the OpenDSS simulation models by using the field collected data. Figure 3.13 shows the overall design flow of these four modules.

Front-end mobile application

The frond-end mobile application is designed using Flutter [39], a free, open-source framework for building native mobile applications with a single code base for both Android [40] operating system and iPhone Operating System (iOS) [41]. This choice helps keep the project costs low while

providing access to a vast developer community, ensuring plenty of resources for troubleshooting and guidance. Flutter's ability to seamlessly integrate with both Android and Apple [42] devices ensures compatibility across various mobile platforms, making the mobile application accessible to a wide range of users, regardless of their devices. Additionally, Flutter's rich set of pre-designed widgets enables us to create a highly customizable and responsive user interface, which is essential for delivering an intuitive, user-friendly experience for utility workers in the field. The goal of the front-end design is to minimize the training required for users, focusing on the ease of use. With features like QR code scanning, real-time geolocation data collection, and dynamic data entry, the interface will guide technicians through the data collection and model creation process efficiently. This simplicity will streamline workflows and reduce potential errors, improving overall product performance. Figure 3.14 shows the screenshots of the mobile application design.

This mobile application allows field technicians to log in to their utility accounts and access all the work orders assigned to them. When opening a work order, the mobile application will allow field technicians to scan a QR code attached to the equipment (containing the equipment serial number), which will auto-populate all the related data from the central database, the QR code, and the GPS stamp provided by the mobile device. The data includes 1) the equipment serial number; 2) the equipment type; 3) the equipment ID (used in the distribution system model); 4) the equipment nameplate parameters; 5) the equipment geolocation; 6) the circuit ID (for identifying the distribution system model to be updated) for this equipment; 7) the date and time for this installation, replacement, or maintenance; 8) the user ID of the field technician providing the installation, replacement, or maintenance; and 9) the notes/logs of the installation, replacement, or maintenance from the field technician. It also allows technicians to manually enter and edit these data.

Central database

The GridScout central database is a MySQL [43] relational database hosted on the cloud servers of the Amazon Web Services (AWS) [44]. It is designed to store all the information about the field equipment, map the equipment to its OpenDSS model, and automatically update the distribution grid simulation models in OpenDSS.

Once field data collection is completed by using the GridScout mobile application, the mobile application sends the collected data to the central MySQL database. The database then updates the related data tables automatically. The database also maintains a data table for OpenDSS simulation data. This table will also be automatically updated for any new equipment installation or replacement of existing equipment, which will then be used to update the OpenDSS model of the distribution system. If any error happens during this process, an error message is thrown and the field technician will be notified via the mobile application.

The database can support various types of equipment including voltage regulators, transformers, switches, storage devices, shunt elements, reactors, loads, inverters, generators, fuses, energy meters, circuit breakers, and capacitor banks. It can be further extended to support more equipment types depending the needs of the utilities.

Back-end automation

The back-end of GridScout serves as a middle-ware which interacts with the front-end mobile application, the central MySQL database, the AWS cloud servers, and the OpenDSS modeling and simulation.

Database interaction. To interact with the MySQL database, the back-end establishes a persistent connection to the MySQL database at the startup of the server. When the Flutter mobile application sends a work order number to the endpoint, the back-end queries the MySQL database to retrieve the associated Circuit ID (i.e., the ID for identifying the associated distribution system modeled in OpenDSS), Component ID (i.e., the ID for identifying the OpenDSS component model corresponding to the equipement being serviced), and the from-bus and to-bus assignments of the equipment in OpenDSS. It then cross-references the OpenDSS table to determine whether the component already exists in the OpenDSS model. Based on the presence or absence of a matching record, the server classifies the requested action as either a replacement of existing equipment or an installation of a new equipment, returning the result to the mobile application client.

Additionally, for each component replacement or installation, the back-end inserts a record into the MySQL table. This record captures the key meta data including the Equipment ID in the OpenDSS model, the equipment serial number from the manufacturer, the equipment geolocation data collected from the mobile device when scanning the QR code, the user ID of the field technician who scanned the QR code and performed the installation/replacement, and any installation/maintenance notes/logs provided by the field technician. All database transactions are protected with exception handling to ensure data integrity and provide reliable feedback to the client application.

AWS cloud server interaction. To manage the OpenDSS distribution system model, the back-end uses the AWS Software Development Kit (SDK) for Python [45] to interact with the AWS cloud server. When a work order is processed, the back-end downloads the current OpenDSS Python script for the distribution system model being updated to a temporary local directory for modification to include the newly installed/replaced equipment. After editing, the updated script which contains the updated distribution grid OpenDSS model is uploaded back to AWS cloud server under a timestamped file name to maintain a version history and prevent overwriting of prior models.

All AWS cloud server operations are wrapped in structured error handling to ensure that failures in file retrieval or upload are captured and reported appropriately.

Error handling and response management. Throughout all the database, file, and AWS operations, the back-end implements structured exception handling to capture runtime errors, generate descriptive error messages, and return appropriate HTTP status codes [46] to the mobile application. For example, if a database query fails, the back-end responds with a ‘500 Internal Server Error’ and includes the exception message in the response body. If a component is not found during retrieval, a ‘404 Not Found’ status is returned.

This approach ensures high reliability, user transparency, and operational robustness, even in the

presence of incomplete data, network failures, or back-end service disruptions.

System impact

This back-end system bridges the gap between field operations and system simulation models by allowing near-real-time updates to both the MySQL asset database and the OpenDSS distribution system model stored in the AWS cloud server. By automating the model update process and tracking every change through a centralized database, the system improves the accuracy, timeliness, and traceability of utility network data, enabling better operational planning, faster maintenance, and more reliable simulations for power distribution engineering.

OpenDSS modeling

GridScout uses OpenDSS for distribution system modeling and simulation, controlled through a dynamic Python script managed by the application back-end. The OpenDSS Python Application Programming Interface (API) is used for establishing interactions between OpenDSS and the other modules of GridScout. The back-end updates and sends the OpenDSS Python simulation files to the AWS cloud server whenever changes are needed. Operators pull the latest Python script, run it locally, and generate updated OpenDSS.dss modeling files and simulation results. Figure 3.15 shows the screenshot of the developed OpenDSS Python script for updating the OpenDSS model.

The OpenDSS Python script developed by the back-end can automatically perform the following functions:

- Compile the base OpenDSS .dss model file;
- Apply new equipment edits, additions, or deletions;
- Save the updated OpenDSS .dss model file (if applicable);
- Perform load flow analysis for the distribution system in OpenDSS;
- Output simulation results.

3.5 Key takeaways and future work

In this task, we first developed a data-driven reduced-order dynamic modeling approach for accurately representing the deep-DER-penetrated distribution power grids in the transmission-level transient stability assessments. The proposed approach utilizes the recently developed theoretical and computational tools in Koopman operator and delay-embedded DMD, which can 1) properly balance the modeling accuracy and modeling complexity; 2) identify reduced-order dynamic models with partial observations; 3) maintain physical interpretability by identifying a globally

linear state space dynamic model. We then developed a LLM-based PSCAD modeling and simulation assistant for creating PSCAD EMT dynamic models and running EMT simulations toward representing the accurate EMT dynamics of the deep-DER-penetrated distribution power grids in the transmission-level transient stability assessments. The fine-tuned LLM can effectively reduce hallucinations in general-purpose LLMs which is critical for generating correct PSCAD Python scripts for EMT modeling and simulations in PSCAD. We also developed a smart field data collection and model updating tool for DER-penetrated distribution power systems. The tool allows for streamlined distribution power grid modeling during field equipment installation and maintenance via a mobile device application operated by field technicians and other utility personnel. This tool addresses the substantial need for distribution utilities to efficiently manage the intensive grid model creation and updating efforts caused by the rapid growth of distributed energy resources (DERs) and aging grid infrastructure. The tool allows for streamlined distribution power grid modeling during field equipment installation and maintenance via a mobile device application operated by field technicians and other utility personnel. This tool addresses the substantial need for distribution utilities to efficiently manage the intensive grid model creation and updating efforts caused by the rapid growth of distributed energy resources (DERs) and aging grid infrastructure.

For the data-driven reduced-order dynamic modeling approach, future work may include: 1) identifying model structural deficiency of reduced-order dynamic distribution system models; 2) developing fast dynamic transmission-distribution co-simulation approaches using the reduced-order dynamic models which are globally linear; 3) developing data-driven control algorithms with the reduced-order globally linear dynamic models.

For the LLM-based PSCAD modeling and simulation assistant, future work may include: 1) fine-tuning Llama for other power system domain-specific applications; 2) developing LLM-assisted power system planning tools; 3) accelerating the DER/IBR interconnection process with LLM-assisted tools.

For the smart field data collection and model updating tool for DER-penetrated distribution systems, future work may include: 1) allowing the tool to directly read an image of the equipment nameplate and parse it into nameplate parameters; 2) extending the software toward supporting more types of equipment, enabling multi-media recordings of equipment installation, replacement, or maintenance logs/notes; 3) enabling metering data management; 4) supporting more distribution system modeling and simulation software.

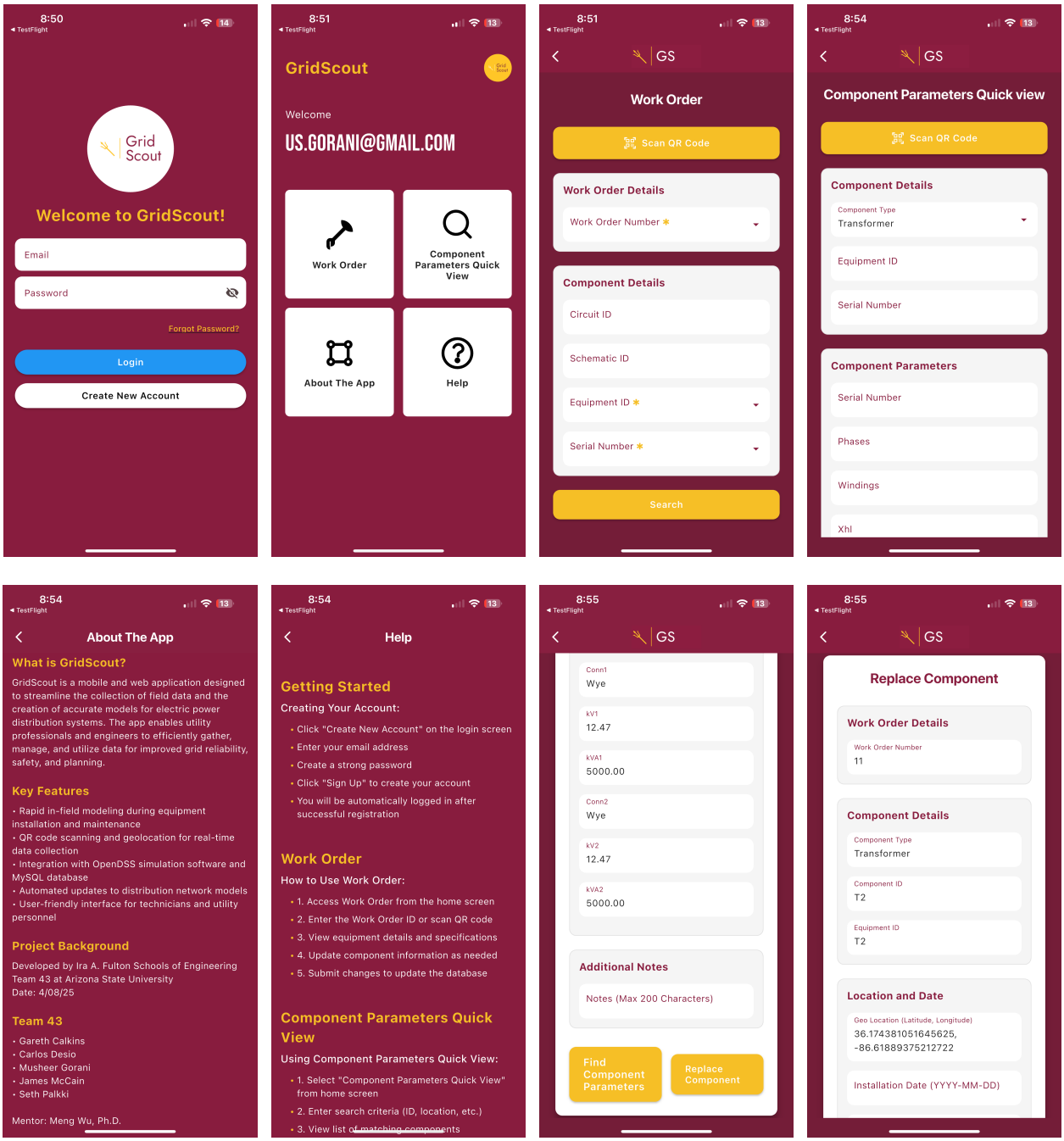


Figure 3.14: Screenshots of the mobile application design.

```python
import py_dss_interface

# Initialize OpenDSS
dss = py_dss_interface.DSS()

# Load the existing circuit
dss.text("Compile DSS_Tassel.dss")

# Add a new transformer
dss.text("New Transformer.T2 Phases=3 Windings=2 XHL=5")
dss.text("~ Wdg=1 Bus=BusF5 kV=12.47 kVA=5000 Conn=Wye")
dss.text("~ Wdg=2 Bus=BusF5r kV=0.48 kVA=5000 Conn=Wye")

# Modify transformer settings
dss.text("Edit Transformer.T1 XHL=6")

# Save the new circuit with the added element
dss.text("Save Circuit As modified.dss")
```

Figure 3.15: Screenshot of the Streamlinedally generated OpenDSS Python script.

4. Short-Circuit-Analysis-based Screening Method for Supporting T&D Multi-fidelity Modeling

The focus of this part of work is the development and verification of short-circuit analysis as a means to estimate the depth of voltage sag at all buses during a fault contingency to support multi-fidelity distribution system modeling for transmission-oriented dynamic contingency analysis. When used as an estimation tool, it should be immune to distribution system aggregation or lack thereof, immune to varying DER penetration levels, and immune to dynamic load penetration. This chapter demonstrates the effectiveness of short-circuit analysis to anticipate the depth of voltage sag in all of the above scenarios.

4.1 Desired Behavior of Short-Circuit Analysis

Generally speaking, bus voltages in a system due to a three-phase fault fall during the event and recover afterward (that is, assuming the system remained stable). The dynamic devices under a transmission bus will have greater excitation during larger voltage sags. In regions with greater excitation, disaggregated and detailed distribution system models will be imperative to capture their dynamic behavior [47–50].Thus, with an effective means to estimate the minimum voltage during a contingency, one naturally obtains a measure of the necessity for distribution system disaggregation/detailed modeling across a transmission system.

As an example, Fig. 4.1 displays an ideal voltage response scenario as some bus. Here, the depth of the voltage sag during dynamic simulation essentially equals the results obtained from short-circuit analysis. Additionally, it is desired that short-circuit analysis errors with over-estimation for the magnitude of voltage sag. In this way, it would serve as a worse case scenario, estimating conservatively with respect to dynamic excitation. In other words, it should be desired that the estimation tool anticipates worse conditions than what actually occur (although relatively close to the actual conditions).

This behavior is natural for short-circuit analysis. Since both dynamic simulation and short-circuit analysis retrieve their results using the exact same network, their results should match appropriately. Additionally, since short-circuit analysis does not capture the contributions from exciters of generators and fault current from loads/DERs, these devices togther contributes to addtional fault currents to help retain voltage levels in a dynamic simulation above those obtained in short circuit analysis.

4.2 Results in Various Test Systems

Several different test cases are examined for the effectiveness of short-circuit analysis. First, results are discussed of short-circuit analysis in a pure transmission-only dynamic simulation (transmission level loads are all aggregated, with no dynamic representation). Then, verification is shown for dynamic simulations where all transmission level loads are disaggregated as simple radial feeders. In this simulation, transmission and distribution systems are modeled separately according to the MATE approach, which was introduced in Chapter 1.2.1. Finally, the method is verified and

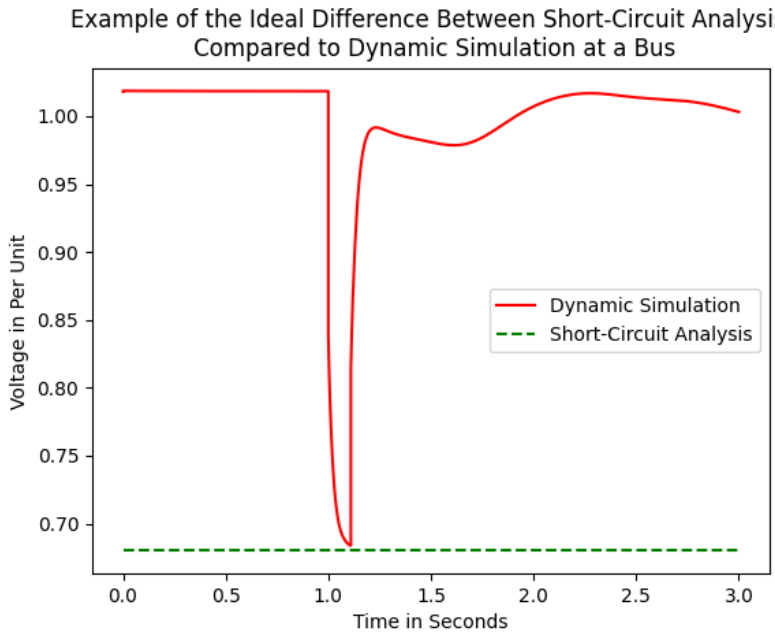


Figure 4.1: An ideal estimate compared to the dynamic simulation voltage response. Short-circuit is less than the dynamic simulation voltage sag, although close to the minimum voltage value

demonstrated in a transmission and distribution co-simulation with high penetrations of DERs.

The radial feeder used for load disaggregation is shown in Fig. 4.2. Nearly all loads at the transmission level are replaced with this feeder in the transmission and distribution test systems. Here, the total load consumption of each feeder is scaled to be equal to the load they are replacing. To accomplish this, all loads and capacitor banks in Fig. 4.2 are scaled to account for this.

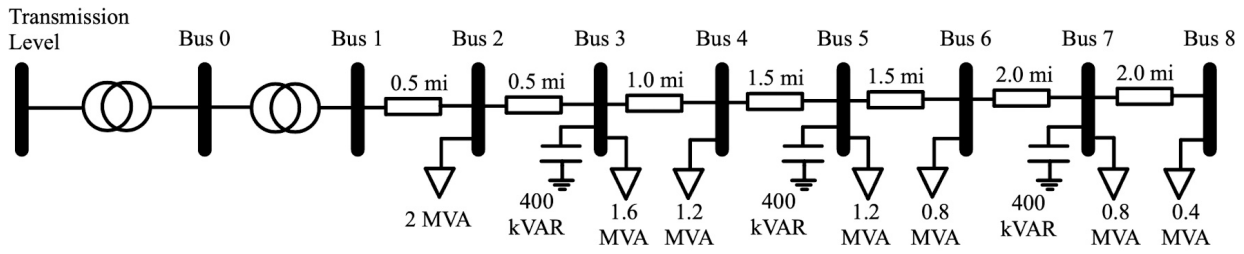


Figure 4.2: Feeder used to represent distribution systems in the dynamic T&D co-simulation

To introduce dynamic behavior into the loads in Fig. 4.2, each load is transformed into separate portions of three-phase induction motors, single-phase induction motors, and constant ZIP loads. In the test systems introduced, 30% of each load is modeled as single-phase induction motors, 30% is modeled as three-phase induction motors, and 40% as constant power (all in terms of power consumption). These percentages are used in this study as a generalization; it should be noted that selection of these parameters is arbitrary and may not reflect actual composition in some systems, especially across different regions and during varying times of year [2]. For example, the percentage

of single-phase induction motor loads would either decrease or increase significantly based on the time of year, as these are usually used for air conditioning units. In general, it should be noted that selection of these parameters can and should be adjusted to best model a utility's expected load composition. Higher percentages of dynamic devices will create greater unique effects, particularly fault-induced delayed voltage recovery (FIDVR) for single-phase and three-phase induction motor loads. This study uses the previously mentioned load composition for testing purposes of the proposed method, and could be easily extended to cover differing system compositions.

In the simulations where DER penetration is modeled, the PVD1 dynamic model is utilized [51]. This model has voltage tripping thresholds and voltage-ride-through behaviors incorporated. This model does not include reactive power injection adjustment based on terminal voltage (Volt/VAR control). However, it is used in this portion of the thesis because Volt/VAR controls will retain voltage levels across the system, so using a model without these controls will further verify the conservative nature of the short-circuit analysis as an estimation tool.

To implement DERs into the system, a model is placed at each load bus in Fig. 4.2. Scenarios of 0%, 30%, and 90% DER penetration are considered. This percentage is considered as the power output of the all the DERs in the distribution feeder, in comparison to the distribution feeder's total load consumption. For example, if the transmission level load is replaced with a feeder that consumes 8 MW, then in a simulation with 90% penetration, a separate DER would be placed at each load bus in Fig. 4.2. Their total combined power reference would be set to 7.2 MW (90% of 8 MW).

Testing results are gathered by placing a three-phase fault at all possible buses and computing the differences that occur between the short-circuit analysis and the dynamic simulation. For each fault scenario, this difference is found as shown in Equation 4.1.

$$\Delta V_{i,k} = V_{i,k}^{dyn,min} - V_{i,k}^{SC} \tag{4.1}$$

Where $V_{i,k}^{dyn,min}$ is the minimum voltage of bus k during the dynamic simulation due to a fault located at bus i, $V_{i,k}^{SC}$ is the voltage obtained at bus k from short-circuit analysis due to a fault at bus i, and $\Delta V_{i,k}$ is the difference between the two. A visual of the testing protocol can be found in 4.3. It should be noted that $\Delta V_{i,k}$ will be negative or positive, dependent upon results from short-circuit analysis. If they are above or below the depth of voltage sag during the dynamic simulation, the difference will be negative or positive, respectively, due to Equation 4.1. From this, desirable results would be that $\Delta V_{i,k}$ has a magnitude of essentially zero, however slightly positive. This would mean that short-circuit analysis is an effective estimator, while providing results conservatively.

Various statistics regarding $\Delta V_{i,k}$ are gathered for all test cases. These metrics include the total average of the average bus differences across each fault scenario, the median value of the average bus difference across each fault scenario, the standard deviation of the average bus difference across each fault scenario, as well as the maximum value of the average bus difference across each fault scenario. These values are calculated as follows, where $\underset{k}{\text{median}}(\Delta V_{i,k})$ denotes the median voltage

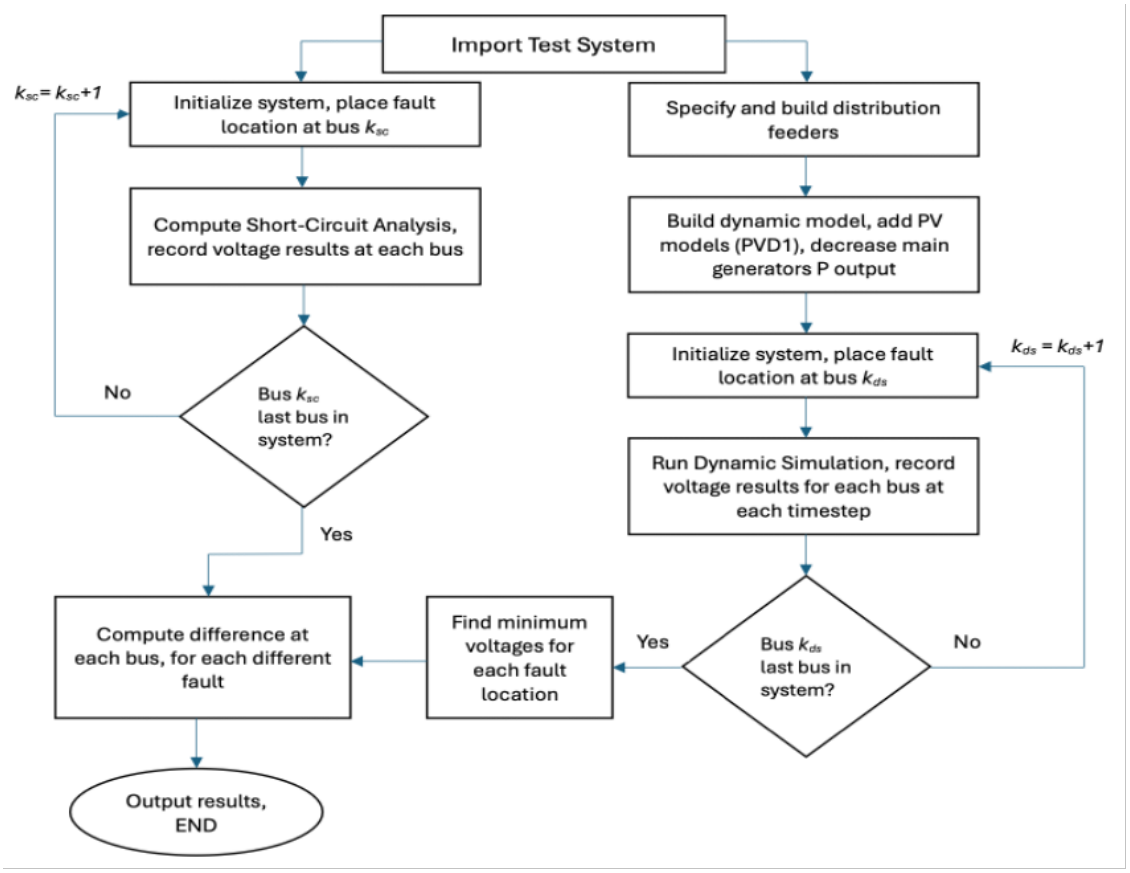


Figure 4.3: Method of verifying the similarity between short-circuit analysis and the dynamic simulation voltage sag

difference under one particular fault i for all buses k, $\underset{k}{\mathrm{STD}}(\Delta V_{i,k})$ denotes the standard deviation of voltage differences under one particular fault i for all buses k, and $\max_{k}(\Delta V_{i,k})$ denotes the maximum voltage difference under one particular fault i for all buses k.

$$Average = \frac{1}{N^2}\sum_{i=1}^{N}\sum_{j=1}^{N}\Delta V_{i,k} \tag{4.2}$$

$$Average\ Median = \frac{1}{N}\sum_{i=1}^{N}\underset{k}{\mathrm{median}}(\Delta V_{i,k}) \tag{4.3}$$

$$Standard\ Deviation = \frac{1}{N}\sum_{i=1}^{N}\underset{k}{\mathrm{STD}}(\Delta V_{i,k}) \tag{4.4}$$

$$Average\ Maximum = \frac{1}{N}\sum_{i=1}^{N}\max_{k}(\Delta V_{i,k}) \tag{4.5}$$

4.2.1 Results in a Generic Dynamic Simulation

First, this study will use the IEEE 9 Bus System and IEEE 300 Bus System as transmission systems, with transmission level loads modeled as constant ZIP loads. The comparison between these two systems will indicate how short-circuit analysis will scale from smaller systems into larger ones. A one-line diagram of the 9 Bus System can be found in Fig. 4.4, and a one-line diagram of the 300 Bus System in Appendix D.1 with all the feeder locations utilized. A three-phase bus fault is applied to each bus, one by one, and the differences at all buses between short-circuit analysis and dynamic simulation are gathered. The difference results for this scenario are displayed in Fig. 4.5.

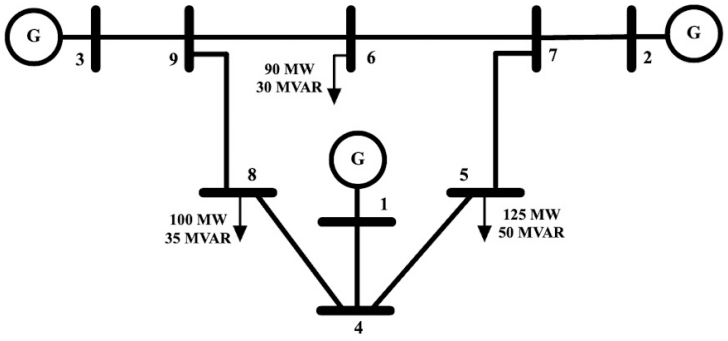


Figure 4.4: The standard IEEE 9 Bus System

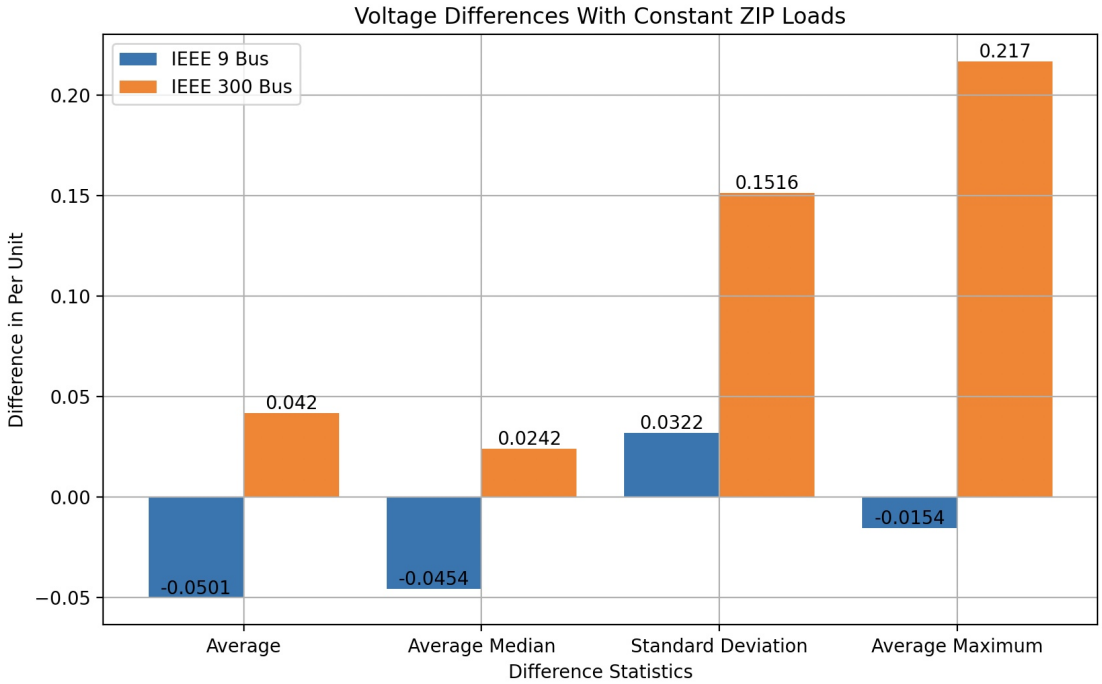


Figure 4.5: Differences between short-circuit analysis and dynamic simulation minimum voltage

It can be seen that the average and average median differences are close to zero, verifying the effectiveness of short-circuit analysis. The average and average median differences in the IEEE 9 bus system are slightly negative values, which is not necessarily desired; however, as the application for short-circuit analysis as an estimation tool lies in large power systems, the more important results are for the IEEE 300 bus system. In this scenario, the differences are close to zero and are positive quantities. This demonstrates that short-circuit analysis can accurately predict the voltage sag during a fault, and error conservatively in larger power systems. Additionally, the transition between smaller systems to larger systems seems to indicate more conservative estimation. This is beneficial for the sake of the estimation tool's applicability.

4.2.2 Results in a Transmission and Distribution Co-Simulation

A transmission and distribution co-simulation offers the system complexity needed to capture unique dynamic effects at the distribution level. This is the scenario in which short-circuit analysis will be used in the final application, thus short-circuit results are now compared to a dynamic co-simulation. Here, the IEEE 9 Bus System and IEEE 300 Bus System are once again used as the transmission systems; however transmission level loads are replaced with the equivalent distribution feeder shown in Fig. 4.2. As previously mentioned, each load in these feeders are represented with dynamic devices to gain insight into how these devices may impact the estimation of short-circuit analysis. Like before, the comparison between these two systems will indicate how short-circuit analysis can scale from smaller systems into larger ones. A one-line diagram of the IEEE 9 Bus System with the incorporated distribution feeders can be seen in Fig. 4.6, and a one-line diagram of the 300 Bus System with locations of distribution feeders can be seen in Fig. D.1. In both systems, a three-phase bus fault is applied to each bus, one by one, and the differences at all buses between short-circuit analysis and dynamic simulation are gathered. The difference results for this scenario are displayed in Fig. 4.7.

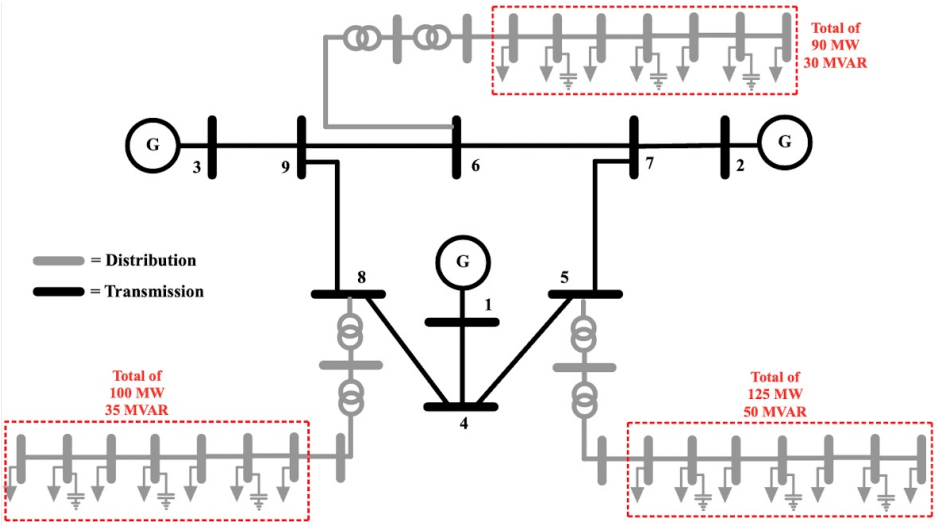


Figure 4.6: IEEE 9 Bus System with radial distribution feeders The loads in each are scaled based on the aggregated load they are representing

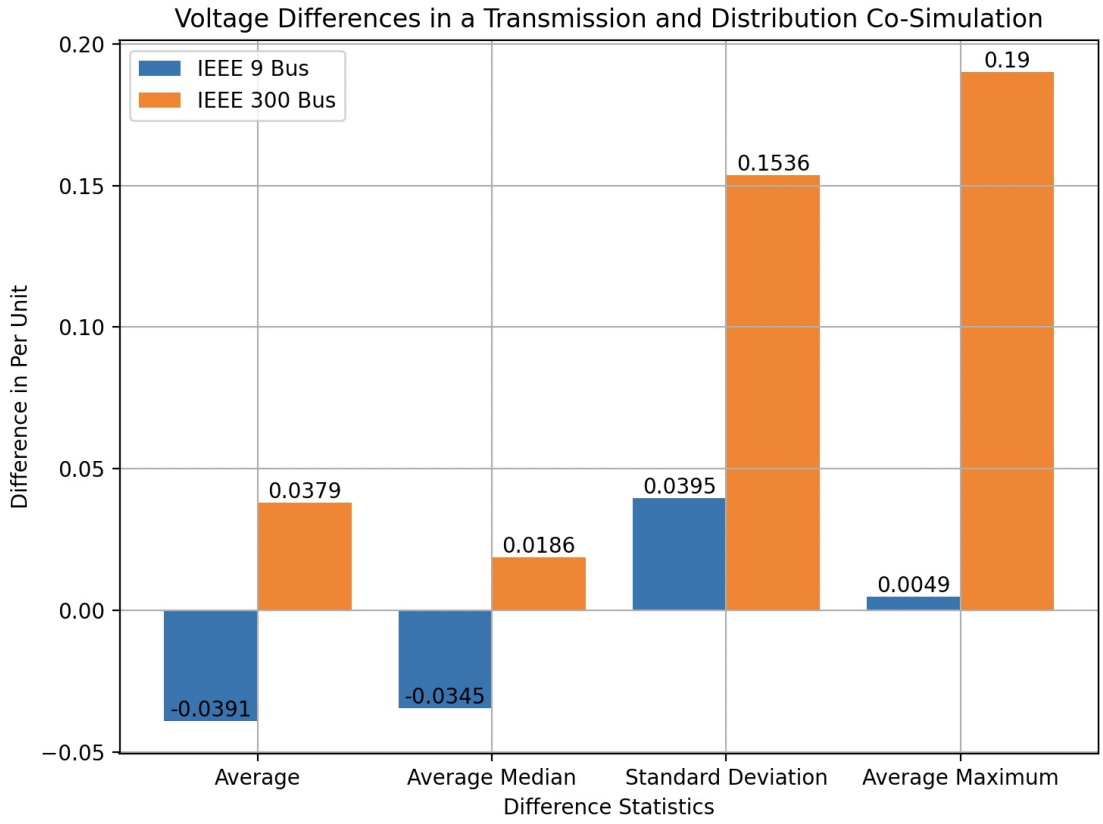


Figure 4.7: Differences between short-circuit analysis and dynamic simulation minimum voltage in a transmission and distribution co-simulation

Similar to the previous scenario, it can be seen that the average and average median differences are close to zero, verifying the effectiveness of short-circuit analysis. The average and average median differences in the IEEE 9 bus system are slightly negative values, which again, is not desired. However, for both systems, short-circuit analysis becomes a better estimation tool in a co-simulation setting compared to a transmission only setting (average increases from -0.0501 to -0.0391 in the IEEE 9 Bus System, and averages decrease from 0.0242 to 0.0186 in the IEEE 300 Bus System). Similar trends are found in the other metrics as well. Again, the application of short-circuit analysis lies in transmission systems with dynamically active distribution systems, so this trend is ideal.

4.2.3 Results in a Transmission and Distribution Co-Simulation With DER Penetration

The dynamic behavior of a system with high penetrations of DERs in response to a fault is not the same as before. Among several reasons, such as the system inertia decreasing, increased fault current injection from downstream locations, the profile will change in a non-negligible way with high DER penetration. This dynamic uniqueness must be captured in a simulation and compared to the results of short-circuit analysis, to verify it's effectiveness in systems with high penetrations of DERs. Here, the IEEE 9 Bus System and IEEE 300 Bus System are once again used as the

transmission systems, however the equivalent distribution feeder shown in Fig. 4.2 now has PVD1 models placed at each load bus. Trials of 30%, and 90% DER penetration are examined. The one-line diagrams of the 9 Bus and 300 Bus Systems are the same as before in Fig. 4.4 and Fig. 4.4 respectively, simply with PVD1 models placed at each distribution system load bus. Like before, a three-phase bus fault is applied to each bus, one by one, and the differences at all buses between short-circuit analysis and dynamic simulation are gathered. The difference results for this scenario are displayed in Fig. 4.8.

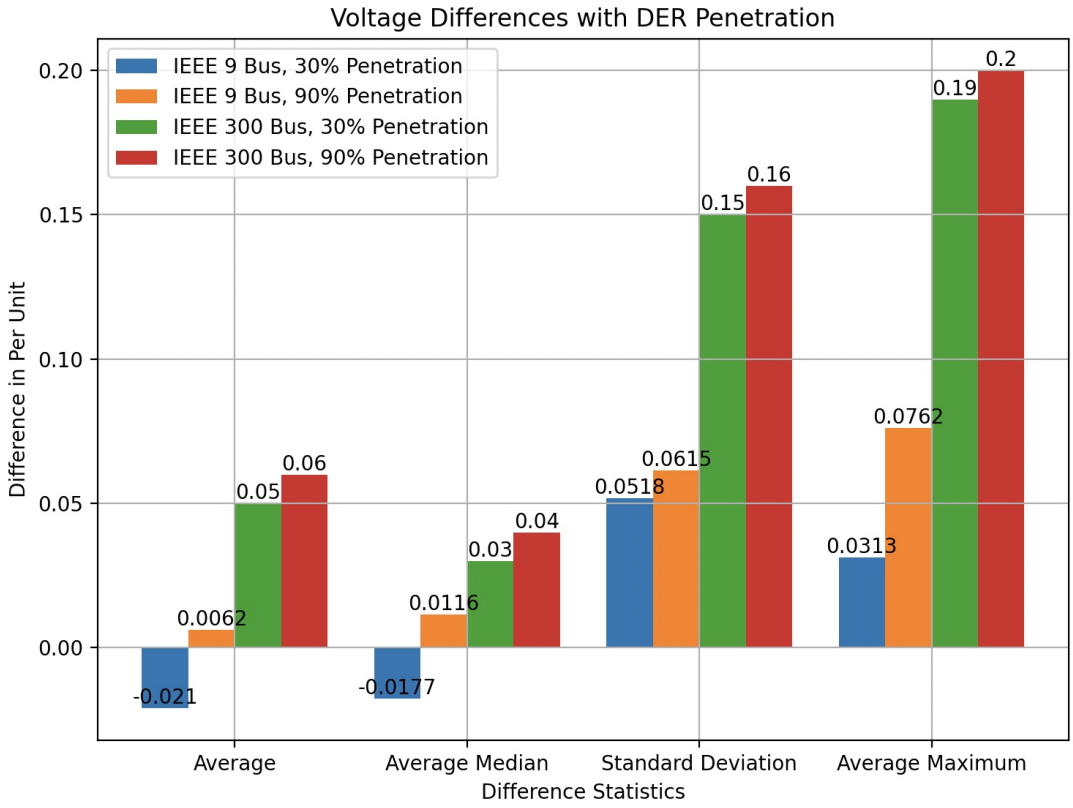


Figure 4.8: Differences between short-circuit analysis and dynamic simulation minimum voltage with DER penetration

In this scenario, it can be seen that the average and average median differences are close to zero, verifying the effectiveness of short-circuit analysis. The main trend to note in this scenario is the voltage retention of the system with higher penetration of DERs. For both systems, the differences become more positive with higher DER penetration. This is ideal, as increasing DER penetration suggests more detailed dynamic modeling; therefore, increasingly conservative estimations with high DER penetration is the characteristic necessary for an effective voltage estimation tool.

5. Automated and Adaptive Distribution Modeling for Dynamic Contingency Analysis

The aim of this chapter is to adaptively and adequately incorporate dynamics of DERs into large-scale, bulk power system dynamic contingency analysis, while significantly reducing the associated computational complexity. This is accomplished through the use of short-circuit analysis, combining it's estimation performance from Chapter 4, into systems containing large amounts of the DERs, where the DERs are modeled with the DER_A model developed in the appendix A. Results demonstrate that by selectively modeling distribution systems with/without detail (disaggregation) across a transmission system via the estimation results of short-circuit analysis, the same dynamic impacts of DERs and unique loads are encapsulated with significantly reduced computational runtime.

5.1 Motivation

The proliferation of DERs are causing rapid changes of the identity and characteristics of power system planning and studies. Their newfound growth and prevalence in distribution systems generate unique dynamic characteristics at the transmission level [52], which have not been previously seen in historical power systems. With this, their adoption into real-time operation and future system planning is increasing, in part due to the recent regulatory measures of FERC Order 2222, IEEE Std. 1547, and more.

FERC Order 2222 mandates that Regional Transmission Operators (RTOs) and Independent Services Operators (ISOs) allow for DERs to participate in wholesale electricity markets. From this, their role in the grand arena of power generation must be deeply understood, particularly the effects on the system in terms of stability if a large amount of DER aggregate's bids are accepted. Additionally, the modeling and monitoring of the system must be detailed enough to have these DERs integrated, without sacrificing the speed necessary for live monitoring (real-time operation). Especially with the addition of detailed DER modeling and the addition of several new buses, computation could drastically increase without a means of reducing modeling runtime that is necessitated by the sheer complexity of these systems.

IEEE Std. 1547 is a standard that regulates the services and functions a DER must exhibit to interconnect to the grid. It sets forth requirements for DERs, such as active voltage regulation and voltage/frequency ride through mandates. As such, DERs now must have the unique grid control techniques as well as dynamic tripping protocols due to voltage and frequency ride through, as mentioned in appendix A for the DER_A model. Thus, their detailed modeling will crucial otherwise these effects will be left out.

With these regulations and the overall need for a grid in which DER penetration is accommodated, the detailed yet low-computationally taxing simulation and modeling of systems are essential in the modern power grid. Therefore, the goal of this research is set. First, the introduction behind the methodology is presented in Section 1. Then, the methodology of the proposed method (termed multi-fidelity method) is outlined in Section 5.3. Subsequently, results are presented for a specific fault contingency, sensitivity analysis is conducted based on the adjustment of the voltage threshold

(delineation between aggregated feeders and disaggregated feeders) alongside statistics of a full list of contingencies in Section 5.4 and Section 5.5. Throughout, both simulation accuracy and runtime of the multi-fidelity method are compared to a fully detailed (disaggregated) simulation and completely aggregated simulation. With this, one can understand the savings of computational complexity and reduced simulation error with respect to these simulations.

5.2 Introduction

Grid modernization brings forth beautiful effects, such as low carbon emissions, low system power losses, and many others; however, if not properly managed these devices can also bring excessive computational complexity and grid instability. Therefore, their detailed modeling is crucial to make sure grid simulations are appropriately demonstrating what will occur in the actual grid.

One example of voltage-dependent dynamic behaviors necessitating detailed modeling are areas with heavy concentrations of air-conditioning motor loads. These areas can significantly delay voltage recovery and have unique fault ride through behaviors [48]. This is because during voltage disturbances, the suppressed voltage can cause stalling of single-phase and three-phase induction motors, consuming a large amount of current and reactive power, worsening the voltage, and this cycle continues. With rising global temperatures, extreme heat events, and overall growth of suburban areas, this issue will continue to grow in frequency and intensity.

Another example is from the previously mentioned high penetration of DERs. Their grid control effects, such as volt/var control, voltage ride through protocols, and many others exhibit dynamic behaviors not seen in bulk previously. Based off each DERs terminal frequency/voltage, these dynamic behaviors become pronounced during large deviating events, further necessitating detailed modeling of these devices. For example, the high amount of grid controls they offer could provide substantial benefit to system health during small but frequent events. However, long-term suppressed voltage from areas with many single-phase induction motors may trip DERs due to voltage ride through thresholds, causing scenarios that are crucial to study as they could possibly lead to system collapse.

Therefore, it is within system operators and planners best interests to model modern systems in a highly detailed manner, when compared to previous methods. For example, it is common to aggregate all DERs and loads underneath the transmission level as one equivalent, as typically done with a composite load model [47]. However, given the true dispersed nature of distribution systems with large voltage drops along them, the previously mentioned dynamic effects will be misrepresented if individual locations on a feeder line are not taken into account. On this note, it should also be emphasized that during voltage-suppressing dynamic events, current injection for DERs and current consumption from dynamic loads increase; this causes larger voltage drops along a feeder line, further exacerbating dynamic grid effects such as reactive power injection, delayed voltage recovery, and device ride through behaviors.

On the other side, the difference between disaggregation and aggregation can be neglected during small voltage sags. When studying a contingency far away from some location, the disaggregation at that location, or lack thereof, will not provide meaningful differences as the voltage differences

along the lines will not be worsened due to a rise in current and unique grid control behaviors.

With this in mind, naturally one sees that modeling areas in the periphery region of a fault or contingency with disaggregation and high detail is crucial for accuracy, however modeling areas outside of the periphery is negligible to results, simply worsening system complexity. In other words, the areas far away from the fault or contingency (outside of some high voltage impact zone) are not in need of disaggregated feeder models (aggregated models suffice), whereas areas close to a fault or contingency (inside some high voltage impact zone) are indeed in need of disaggregated feeder models. If the system were to be modeled in such a manner, the unique dynamic effects of high-voltage deviating regions would be encapsulated, while maintaining some level of modest system computational complexity by leaving low voltage deviating areas aggregated.

The main contributions of the proposed method can now be introduced. First, short-circuit analysis is presented to estimate the voltage across the system for use in a multi-fidelity distribution system construction for each fault contingency. This linear computation allows for the creation of a customized multi-fidelity system by comparing the result of short circuit analysis at each transmission level bus to a predetermined threshold. Buses falling underneath or above these thresholds have their loads replaced with corresponding distribution system fidelity. Second, this process's effectiveness when used in multiple contingencies in succession, is demonstrated due to its ability to automate system construction/building on the fly. Each successive, new multi-fidelity system is customized to the fault under study, while at the same time requiring no added input from the user. Lastly, the proposed method is able to accomplish the multi-fidelity system simulation process through simple parameterization of the user-defined system composition. This means that the user can use the proposed method in any kind of system composition since the constructed system will have the exact composition as dictated by the user, allowing for this proposed method's use in a changing/highly-fluctuating system composition.

5.3 Proposed Methodology

With short-circuit analysis utilized as the estimator of system voltages in anticipation of a fault contingency, an adaptable, reliable, and conservative estimator is obtained based on the discussions from Chapter 4. The short-circuit analysis is performed in between each successive contingency, building a selectively and fully customized system representation based on the next contingency to analyze each time. This allows for a multi-fidelity system to be used in all scenarios, optimizing accuracy with simulation runtime across all three-phase fault contingencies. An example of a multi-fidelity system can be seen in Fig. 5.1, based on a three-phase fault located at Bus 28 in the IEEE 39 Bus System.

The process of system building is itself a linear task, iterating through each bus in the transmission system and replacing it's load amount with an equivalent feeder. The decision on the level of disaggregation is based on a comparison to a predetermined voltage threshold. The algorithm iterates through all transmission level buses, compares the short-circuit analysis result to this threshold, and constructs a dynamic feeder according to this rule. A flowchart of this process is found in Fig. 5.2. The proposed method attaches the loops on the left to general dynamic contingency analysis

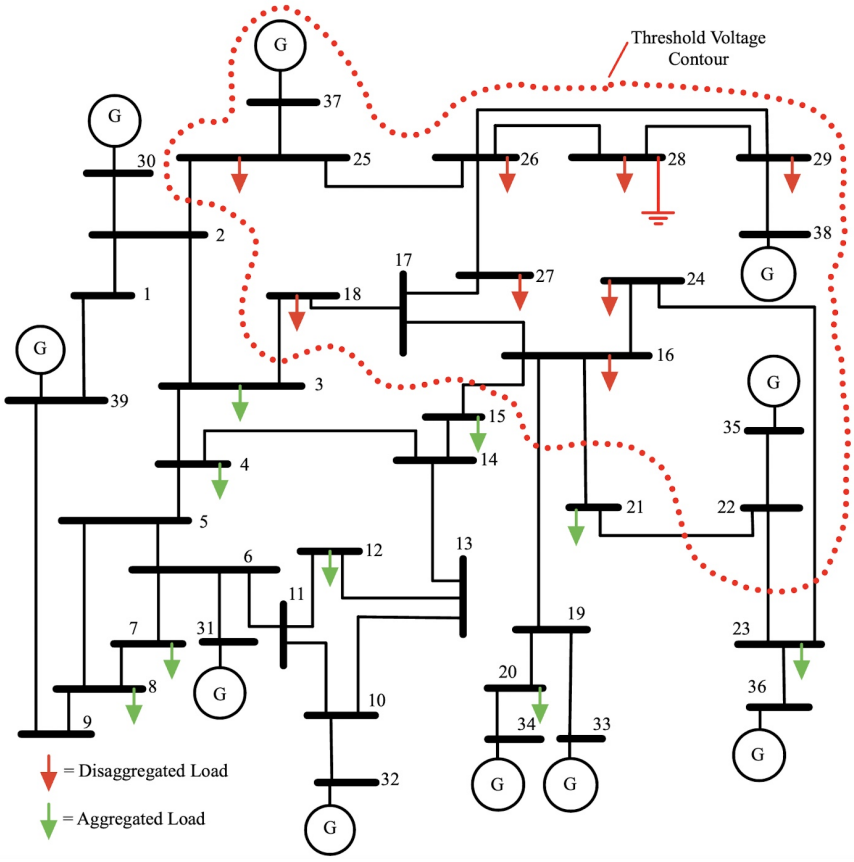


Figure 5.1: Example multi-fidelity system when utilizing short-circuit analysis to anticipate voltage

In order to replace a transmission level load with an equivalent feeder, this study uses predetermined feeder topologies. The loads in each of these feeders are scaled to make the total composition of the feeder from the transmission level perspective the same as before. The two predetermined feeders for this study are the composite load model with distributed generation (CMPLDWG) [2], and the simple disaggregated radial feeder shown previously in Fig. 4.2. The modified CMPLDWG, shown in Fig. 5.3, is modeled in a positive sequence representation which properly mirrors current transmission level studies (normally conducted in a positive or three-sequence domain). The disaggregated feeder is modeled as a separate subsystem from the transmission system, mirroring how a typical transmission and distribution system co-simulation would be conducted (distribution systems are modeled in a three-phase domain). For both feeders, a predetermined portion of the loads are set to be represented by single-phase induction motors (labeled 'M' in Fig. 5.3). Note the radial feeder in 4.2 has these as well at each disaggregated bus. The rest of the portion of each load is modeled via constant power loads (the arrows in feeder figures). Additionally, at each load bus a DER_A model (labeled 'DG' in Fig. 5.3) is placed for penetration of DERs into the system. The portion of loads served by DERs is also a predetermined value, which sets the power rating of the DER during system construction.

As an example, the scenario shown in Fig. 5.1 would use the radial 9 bus feeder inside of the region dictated by the red dotted line, whereas the modified CMPLDWG would be used outside of

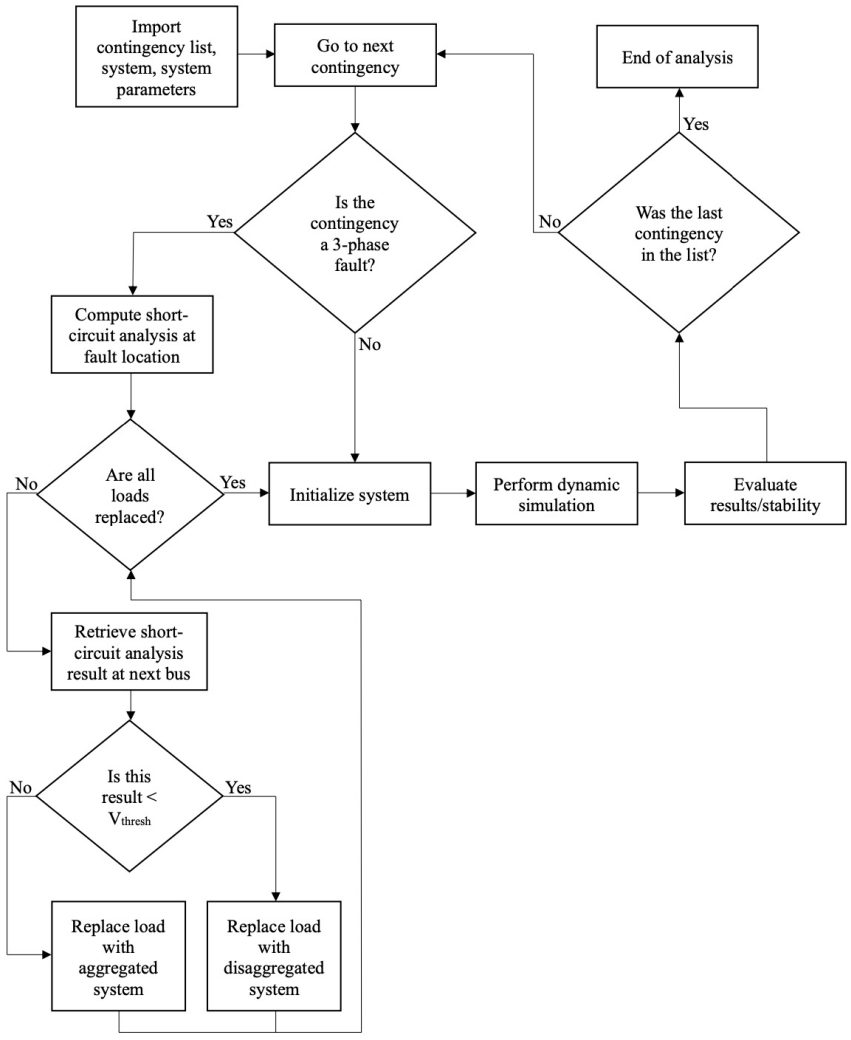


Figure 5.2: Flowchart of proposed algorithm for dynamic contingency analysis with selective system building

it. Selection of the feeder used inside of the high impact region is for example only; the interface used to implement the proposed method allows for straightforward further testing of different feeder models (both inside and outside the high impact region), however the simple 9 bus feeder is used as a proof of concept in this test system.

With the predetermined parameters for motor load penetration and DER penetration, the power rating of both devices can be set. These parameters of the system can be easily be changed by the user, without any sacrifice from the perspective of the proposed method. For example, a bulk power system with 100% DER penetration can be studied as well as a power system with 0% DER penetration, without any extra training or offline wait time of the system builder when switching between the two. Therefore, the proposed method allows for changes in the state and composition of the system across varying times of year, times of day, and general load patterns.

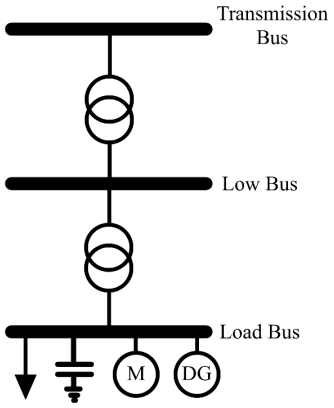


Figure 5.3: Composite load model (CMPLDWG) oneline [2]

After each customized, multi-fidelity system is built, the dynamic simulation can be performed. Following each dynamic simulation, the system is then set up for the next contingency in the total list of contingencies. Because of this, the system is reinitialized with the new multi-fidelity system prior to each subsequent contingency, eliminating issues when switching distribution system models during a dynamic simulation.

A key point to reiterate here is that the system building is entirely automated. In other words, it is done without intervention or input from a user. For each selectively built system, the process is done in an automated manner as short-circuit analysis and the predetermined thresholds declare the multi-fidelity regions themselves. Additionally, the changes from each selectively modeled system in a list of contingencies are also done in an automated manner, as short-circuit analysis is directly adaptable to all three-phase fault contingencies. For example, in the two multi-fidelity systems shown in Fig. 5.4, the construction of each system and the changes between the systems is automated, performed in an accurate, fast way without any necessary input from a user.

5.4 Three-Phase Fault on Three-Hundred Bus Transmission System with 50% DER Penetration

The IEEE 300 Bus Test System (seen previously in Fig. D.1 is a reasonably large test system to demonstrate advantages of the proposed method, so it is utilized in this study. Here, a total of 41 dynamic loads replace standard transmission level loads for dynamic analysis. It is at these locations where either an aggregated or disaggregated feeder will take the place of the previous transmission level load, according to results from short-circuit analysis.

For demonstration in this simulation, parameters for dynamic devices and device load percentage were selected based on published guidelines. From [2], the single-phase induction motor is set to consume 30% of the total load (with respect to active power) at the bus in which it is placed at. As mentioned previously, this load composition is highly dependent on time of year, time of day, geographical location, and many other factors; these parameters are used simply for demonstration purposes. Note that the proposed method is able to adapt to varying parameterization of these

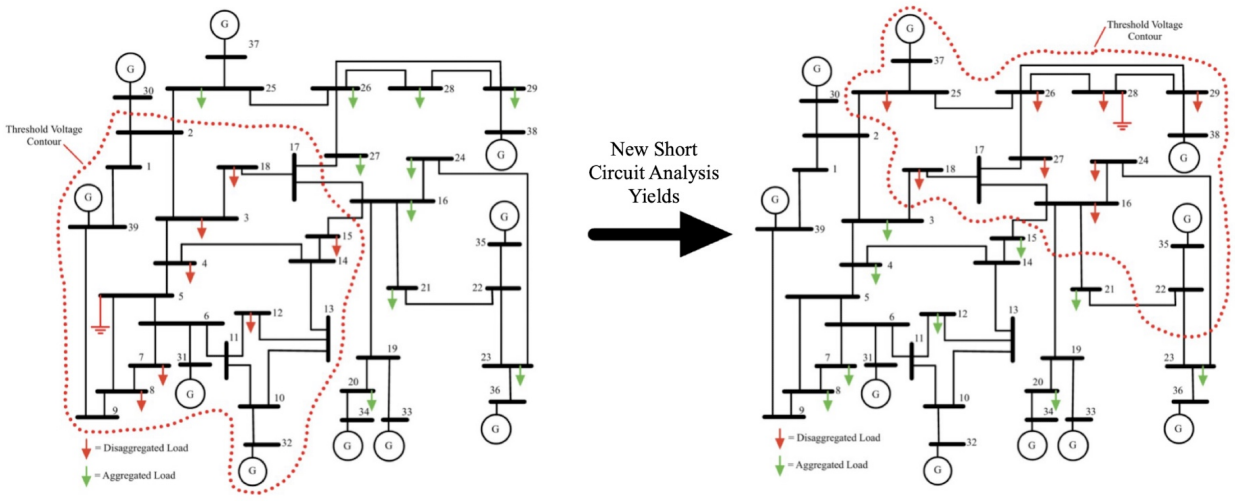


Figure 5.4: Areas of aggregated vs. disaggregated modeling areas for separate contingencies, and switching between them

dynamic devices, as the distribution feeder models are set to exactly match the user's settings (nothing is pretrained). For DERs, this particular study will look at a scenario of 50% penetration (50% of the load will be served locally by it's DER; this is how it's power reference is set). This is done to demonstrate the effects these resources have, while still being applicable to many different DER penetration scenarios.

Several intrinsic parameters to these devices can be found in Appendix C. A couple key settings to note are as follows; the stalling voltage of single-phase induction motors is set to 0.55 pu, and the stalling timer is set to 0.033 seconds. With these parameters, the motor will enter a stalled state if the voltage falls below 0.55 pu for a duration greater than 0.033 seconds; otherwise, it will remain in a non-stalled state. Seen soon in the results, stalling of induction motors cause a unique phenomenon termed fault induced delayed voltage recovery (FIDVR) [49]. This behavior is characterized by the excessive current consumption of these induction motors in a stalled state, which can lead to severe under-voltage lasting for several seconds after a fault. During this prolonged period of voltage sag, several dynamic events may become triggered, such as voltage-ride-through protocols, extreme Volt/VAR control, and several others. All of the single-phase induction motor parameters used in this study can be found in tabular format in C.1 in Appendix C.1.

Additionally, using the guidelines set by [53], the parameters which characterize the unique voltage-ride-through behaviors of DERs discussed in Appendix A Section A.3.6 are selected as follows; $Vrfrac = 0.5$, $Vh0 = 1.2\ pu$, $Vh1 = 1.12\ pu$, $Vl0 = 0.45\ pu$, $Vl1 = 0.6\ pu$, and $Tvl0 = Tvl1 = Tvh0 = Tvh1 = 0.16\ sec$. The full table of DER model parameters used in this test can be found in C.2 and C.3 located in Appendix C.2.

The first contingency examined is a three-phase to ground fault located at Bus 45. The fault is applied for 0.07 seconds prior to being cleared. During this disturbance, several bus voltages fall significantly, exciting dynamic load behaviors such as motor stalling and DER tripping/ride through behaviors. Three separate simulations are conducted, one with all feeders modeled in

a disaggregated manner, another with all feeders modeled in an aggregated manner, and another using the multi-fidelity modeling approach (the proposed method). Ideally, the proposed method follows the fully disaggregated simulation in terms of accuracy, while at the same time following the fully aggregated simulation in terms of simulation runtime.

Shown in Fig. 5.5 is the corresponding contour of 0.8 pu as dictated by short-circuit analysis in anticipation of the dynamic simulation (a full system visual can be found in Fig. D.2 located in Appendix D.2). When using the multi-fidelity simulation, all dynamic loads inside this contour are modeled as disaggregated feeders using Fig. 4.2, whereas the dynamic loads outside the contour are modeled in aggregation using Fig. 5.3. In contrast, the fully disaggregation simulation and fully aggregated simulations mentioned below use the disaggregated feeder in Fig. 4.2 and the aggregated feeder in Fig. 5.3 for all dynamic loads regardless of proximity to the fault bus, respectively.

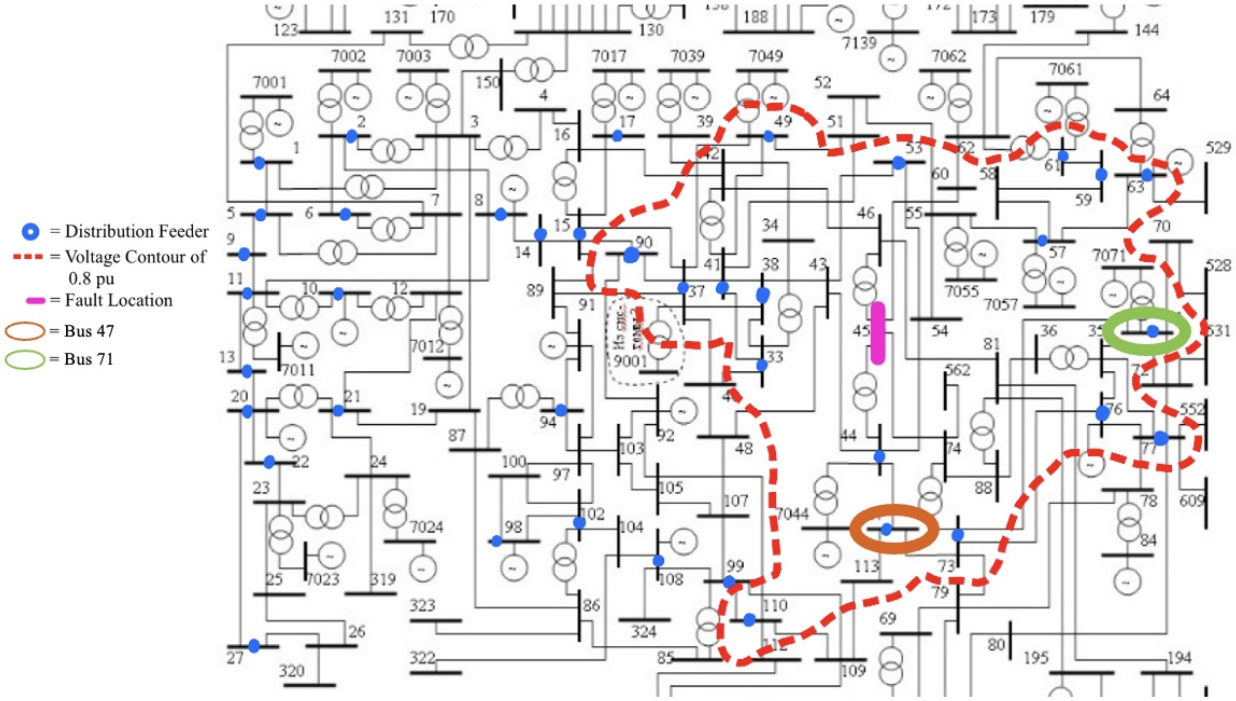


Figure 5.5: A zoomed-in plot of the impact zones found through short-circuit analysis due to a fault at Bus 45

Differences in Voltage and DER Behavior at Bus 47 Due to a Fault at Bus 45

One of the main differences that can arise between a fully disaggregated simulation and aggregated simulation are the dynamic responses of DERs. In the aggregated feeder simulation, a single DER is used to represent all of the DERs below a bus in the transmission system, shown in Fig. 5.3. In contrast, the disaggregated simulation uses the feeder previously introduced in Fig. 4.2 to incorporate seven separate DERs, one placed at each load bus. In this manner, voltage drops along

a feeder line are encapsulated in the model, which cause significant dynamic behaviors.

Shown below are the status of the DERs in the feeder underneath Bus 47 during the fault at Bus 45. In the aggregated modeling approach, the sole DER model enters a partially tripped state at a time of roughly 0.67 seconds, seen in Fig. 5.6(a), where "Full Trip" is the boolean variable indicating a complete trip, and "Frac Trip" is the boolean variable indicating a fractional trip. This is because the voltage falls below $Vl1$ for a time greater than $Tvl1$ seconds; thus, only 50% of the remaining model returns online upon voltage recovery (due to $Vrfrac = 0.5$), seen in Fig. 5.6(b). The model does not fully trip as, in this modeling approach, the voltage does not fall below $Vl0$ for a time greater than $Tvl0$ seconds.

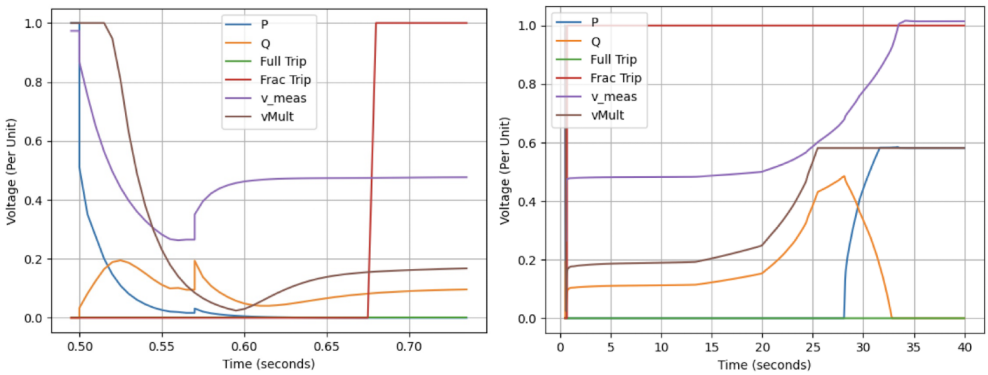


Figure 5.6: Select internal states of the single DER underneath Bus 47 in the aggregated modeling approach immediately after (a) and many seconds (b) after the fault

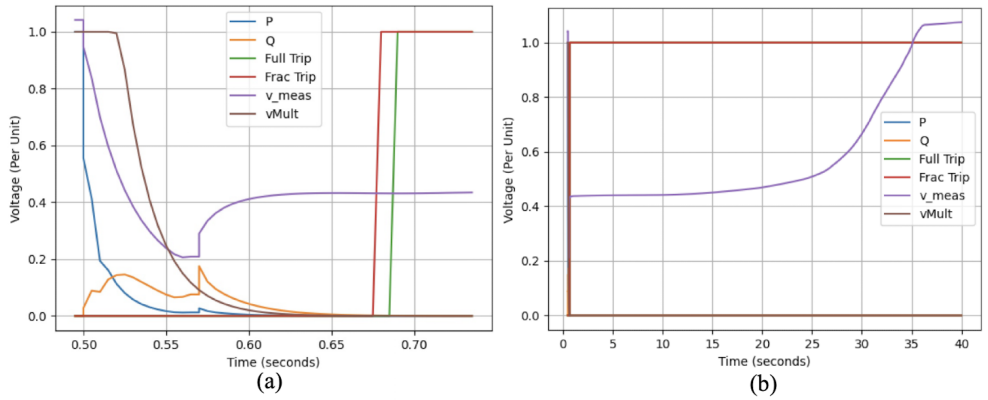


Figure 5.7: Select internal states of the DER at Bus 6 on the feeder underneath Bus 47 in the disaggregated and multi-fidelity approach immediately (a) and several seconds (b) after the fault

This behavior is properly mirrored for some of the DERs along the disaggregated feeder in the disaggregated simulation, mainly the ones further upstream to the transmission level. However, the voltage drops low enough towards the end of the feeder in this approach to fully trip those models (the voltage drops below $Vl0$ for longer than $Tvl0$). This can be seen in Fig. 5.7 where "Full Trip" goes to 1 at a time of roughly 0.68 seconds. With this, these models remain tripped upon voltage recovery, causing significant differences between the disaggregated and aggregated simulations.

Due to this misrepresentation, the power output of the aggregated DER (which, in theory, models the combined behavior of all the DERs in the disaggregated feeder) severely overexaggerates the actual power output of the DERs in the disaggregated feeder in terms of both active and reactive power. Due to the DERs on the end of the feeders tripping completely (underneath Bus 47, the DERs located on Bus 6, Bus 7, and Bus 8 in the disaggregated feeder all completely trip, with the rest partially tripping), a distinct difference is found after the fault is cleared as these DERs cannot support the voltage recovery of the system. Found in Fig. 5.8 and Fig. 5.9 are the total output differences between the three separate simulation methods' DER power outputs (note that the multi-fidelity simulation utilizes the disaggregated feeder at Bus 47 as it is located within the high impact region). The multi-fidelity approach appropriately demonstrates the same DER behavior of the fully disaggregated approach since it also utilizes a disaggregated feeder at this bus, however the same cannot be said about the aggregated approach.

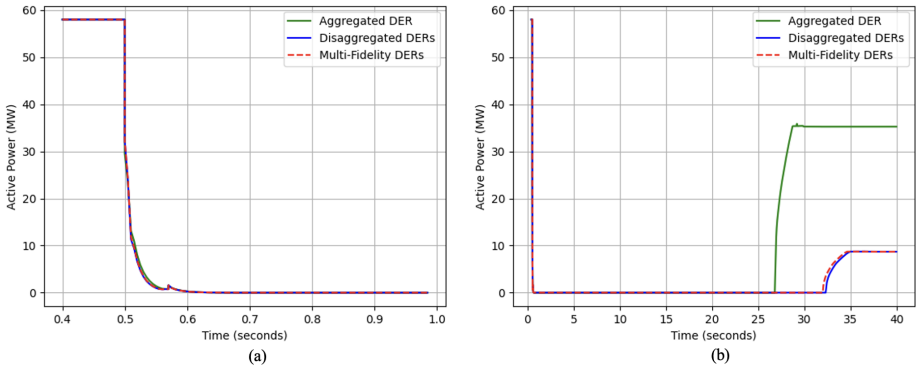


Figure 5.8: Active power from the single DER underneath Bus 47 compared to the combined active power from all DERs in the disaggregated feeder underneath Bus 47

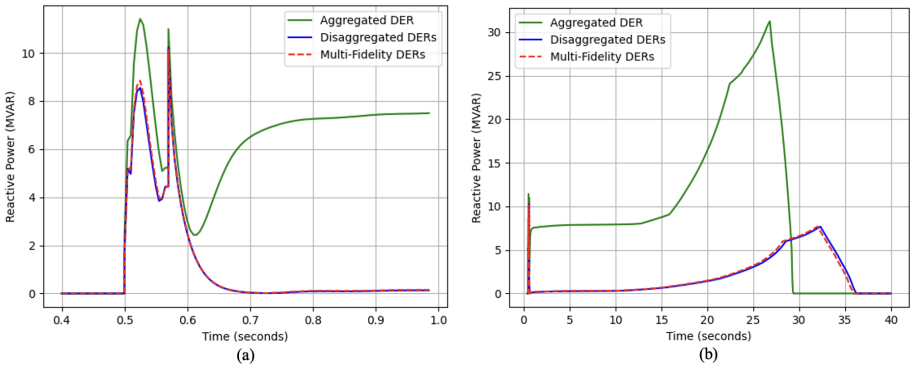


Figure 5.9: Reactive power from the single DER underneath Bus 47 compared to the combined active power from all DERs in the disaggregated feeder underneath Bus 47

The outcome of this misrepresentation of DER dynamic tripping protocols becomes evident at the transmission level, shown via the voltage at Bus 47 displayed in Fig. 5.10. The aggregated approach recovers from it's lower post-fault voltage faster than the disaggregated approach, because with the DERs tripped at the end of the feeder in the disaggregated approach, they cannot provide active and reactive power injection to aid in voltage recovery (Figs. 5.8 and 5.9). This is not

the case when modeled in the aggregated approach, allowing for faster voltage recovery. Note that the multi-fidelity simulation correctly tracks the disaggregated simulation, highlighting the effectiveness of the proposed method in encapsulating dynamic events like this.

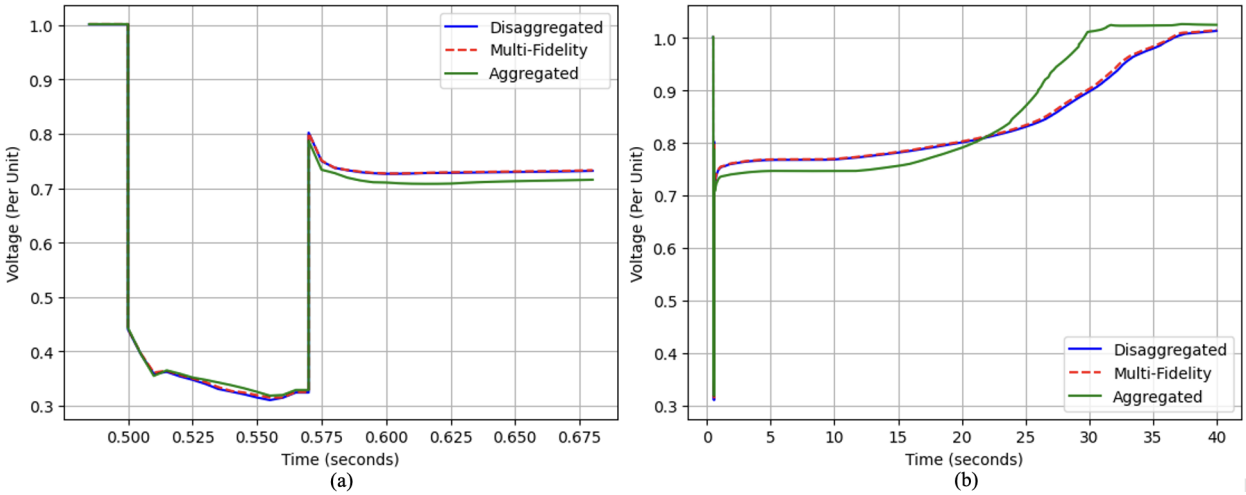


Figure 5.10: The immediate (a) and prolonged (b) voltage responses for the three separate simulation methods at Bus 47 due to a three-phase fault located at Bus 45

Differences in Voltage and DER Behavior at Bus 71 Due to a Fault at Bus 45

A more extreme example can be found by examining Bus 71 in the test system, circled in green in Fig. 5.5. This dynamic load bus is located slightly farther away from the fault than Bus 47, and experiences intense variation between the aggregated and disaggregated modeling approaches. Mainly, a similar phenomenon occurs where the DER models in the disaggregated feeder trip, however the DER model in the aggregated feeder does not. Particularly, differences in motor stalling dynamics cause significant voltage differences during the fault period between the disaggregated and aggregated simulations, triggering corresponding significant differences in DER fault-ride-through behaviors/tripping. The effect of this is seen in Figs. 5.11 and 5.12, where the total power output from the aggregated DER is compared to the combined output of all DERs in the disaggregated feeder underneath Bus 71.

Seen here, once again, the multi-fidelity simulation has its DER's combined power output track the disaggregated simulation's DER combined power output, demonstrating the effectiveness of this method. This is accomplished because the multi-fidelity simulation uses a disaggregated feeder at Bus 71, as it is inside of the high impact region. However, the aggregated modeling approach does not show the DER entering a tripped state of any kind, severely misrepresenting it's true dynamics (here, the disaggregated simulation is considered to be true).

Similarly to the voltage at Bus 47, the voltage at the transmission level (Bus 71) in the aggregated simulation is allowed to return to pre-fault voltage levels much faster than the disaggregated and multi-fidelity simulation, seen in Fig. 5.13. Additionally, the induction motor stalling is less severe,

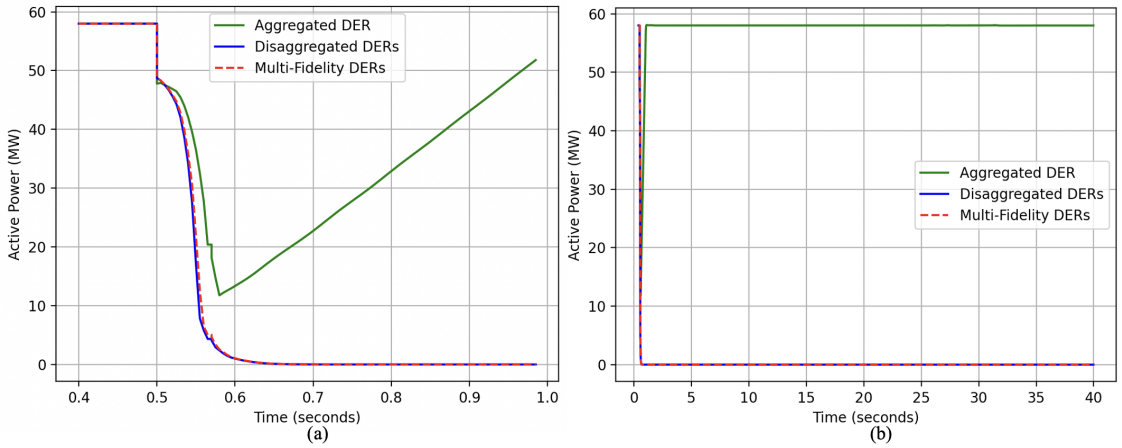


Figure 5.11: Active power from the single DER underneath Bus 71 compared to the combined active power from all DERs in the disaggregated feeder underneath Bus 71

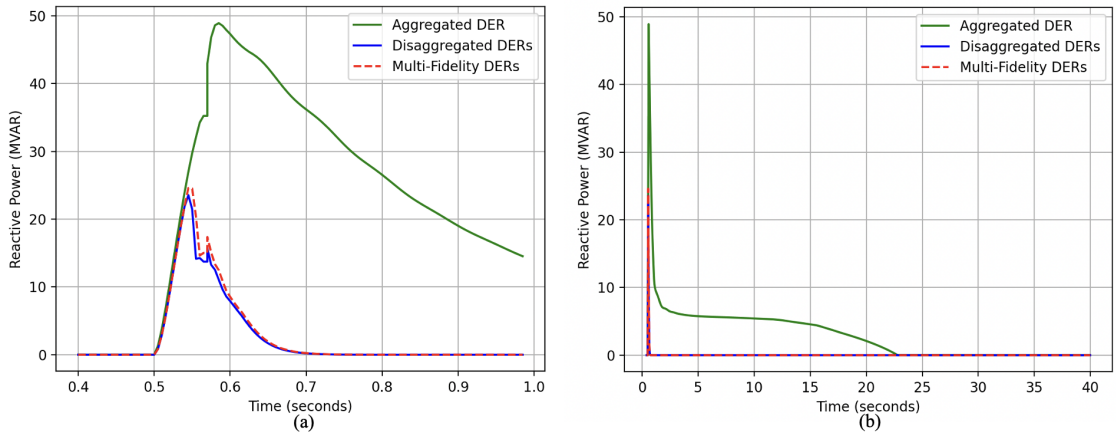


Figure 5.12: Reactive power from the single DER underneath Bus 71 compared to the combined active power from all DERs in the disaggregated feeder underneath Bus 71

as the voltage does not dip as low as the disaggregated simulation seen in Fig. 5.13a. This leads to severe differences between the simulations, as the magnitude of per unit voltage difference seen in the aggregated simulation compared to the disaggregated reaches a maximum of 0.115. In contrast, the per unit voltage difference when comparing the multi-fidelity approach and the disaggregated modeling approach is only a maximum of 0.0092.

Full System Differences in Voltage and Simulation Time due to a Fault at Bus 45

Overall, the differences from each simulation method across all buses are gathered for a better understanding of the performance of the multi-fidelity approach in addition to the buses previously examined. For this study, the differences of the multi-fidelity approach are compared to the fully disaggregated modeling approach via root-mean-squared-error (RMSE) and maximum voltage difference (the greatest difference between the two simulations that occurs over the course of

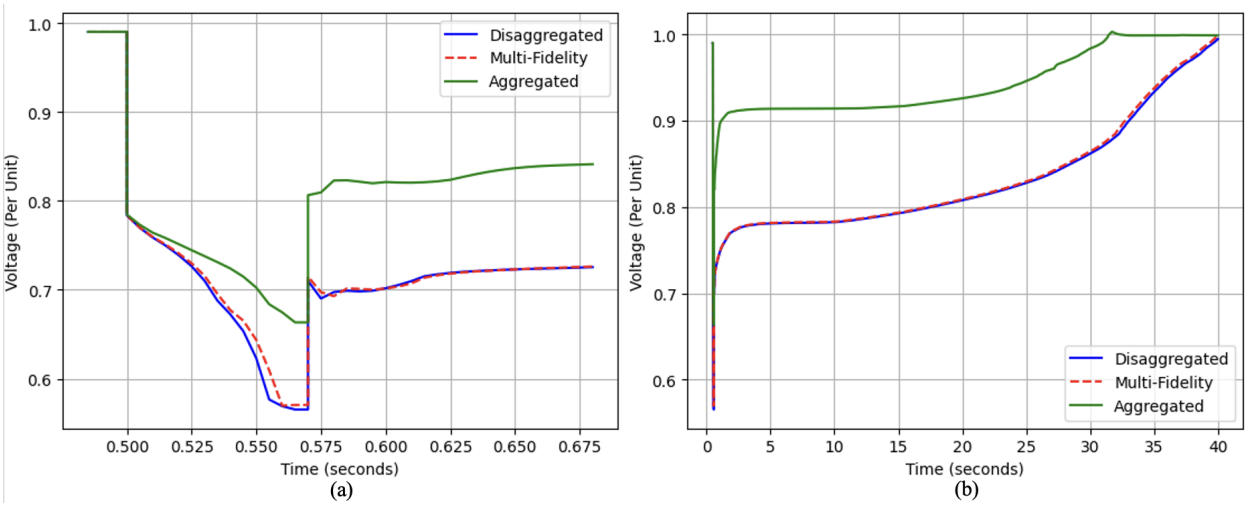


Figure 5.13: The prolonged voltage response (b) and the immediate response (a) for the three separate simulation methods at Bus 71 due to a three-phase fault located at Bus 45

the simulation). The RMSE and maximum voltage difference for the aggregated simulation are also computed for comparison. In addition, the percent increase in simulation runtime from the aggregated simulation to both the multi-fidelity and disaggregated simulations are displayed. Ideally, the multi-fidelity modeling approach adopts the same runtime as the aggregated modeling approach (alluding to similar computational complexity), while adopting the same simulation accuracy as the fully disaggregated approach (a RMSE and maximum voltage difference of close to zero, as the disaggregated approach is considered as the ”true” simulation due to using the most detail). The results of this analysis are described below in terms of simulation runtime first, displayed in Fig. 5.14. Note that the proposed method's simulation (labeled ”Multi-Fidelity”), shows a significant decrease in simulation runtime when compared to the fully disaggregated simulation, reducing the introduced simulation runtime of the disaggregated simulation by over a factor of 4. This is due to the number of feeders that are modeled in an aggregated manner in the multi-fidelity modeling approach (outside of the high impact region).

This improvement in simulation runtime is accomplished while reducing the average RMSE introduced by the aggregated simulation by over a factor of 10, seen in Fig. 5.15(a). Furthermore, the maximum voltage difference that occurs in the simulation across all buses is reduced by well over a factor of 5, seen in Fig. 5.15(b). From this, the accuracy of the proposed multi-fidelity feeder modeling approach is demonstrated across the system for it's retained computational complexity compared to the aggregated approach, and it's retained simulation accuracy compared to the disaggregated approach.

Effects of Varying the Disaggregation/Aggregation Voltage Threshold

As every decision in engineering has it's tradeoffs, selection of a low voltage threshold that delineates between high impact and low regions (use of disaggregated feeder models and aggregated feeder

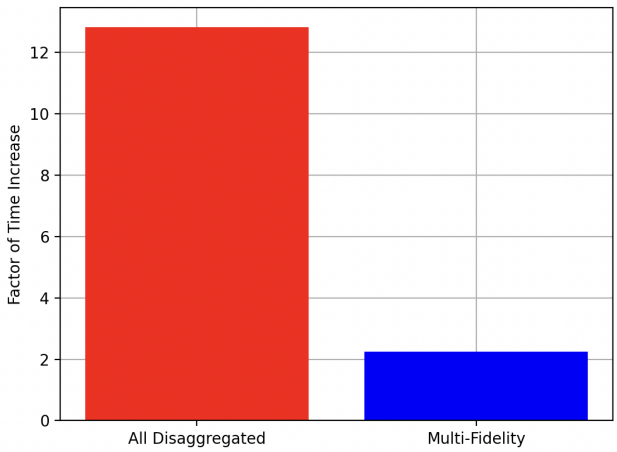


Figure 5.14: Simulation time increase found when compared to the aggregated modeling approach to the disaggregated approach and the multi-fidelity approach

models, respectively) can cause the proposed method to misrepresent the true dynamic behavior of the system. This would be due to an excess of aggregated feeder modeling where voltages fall greatly during a contingency. However, a lower threshold will reduce computational complexity by reducing the total number of buses in the simulation (the number of disaggregated feeders would shrink across the system). Therefore, there exists a tradeoff between simulation accuracy and simulation runtime, based off this voltage threshold parameter for the multi-fidelity approach. This tradeoff also works in the opposite way, where representing the majority of the dynamic behavior of the system can be accomplished with a higher voltage threshold, however, at the expense of computational complexity. Therefore, it should be understood how simulation inaccuracy can turn from minimal to substantial subject to varying voltage thresholds.

As the voltage threshold moves, there may be very complex interactions between dynamic devices that occur. While some of these may be slightly random in a sense, there are a couple different known behaviors that may be caused as the voltage threshold moves. For example, as the threshold moves past parameters such as the stalling voltage of the single-phase induction motor, the $Vl0$ parameter from the DER_A model, the $Vl1$ parameter from the DER_A model, and the point at which the Volt/VAR control stops from DERs (set to be 0.12 pu below the initialized terminal voltage of the DER_A model), these dynamic devices will be represented in an aggregated feeder as opposed to a disaggregated feeder (or vice versa). As seen before with the voltage drop along a feeder causing differing DER tripping behaviors and induction motor stalling characteristics, errors will most likely occur as the devices become modeled in an aggregated manner (as the voltage threshold moves from a value close to 1.0 to a value closer to 0.0 pu).

Therefore, varying voltage thresholds are now tested in the multi-fidelity modeling approach, using the same test system as before. Thresholds of 0.0 pu (fully aggregated), 0.2 pu, 0.4 pu, 0.5 pu, 0.6 pu, 0.7 pu, 0.8 pu, 0.9 pu, and 1.0 pu (fully disaggregated) are analyzed to attempt to show how moving across these parameters affects the outcome of the multi-fidelity simulation method. Once again, results from the multi-fidelity approach which deviate little from the aggregated approach in terms of simulation runtime are ideal (the threshold of 0.0 pu), whereas results which deviate

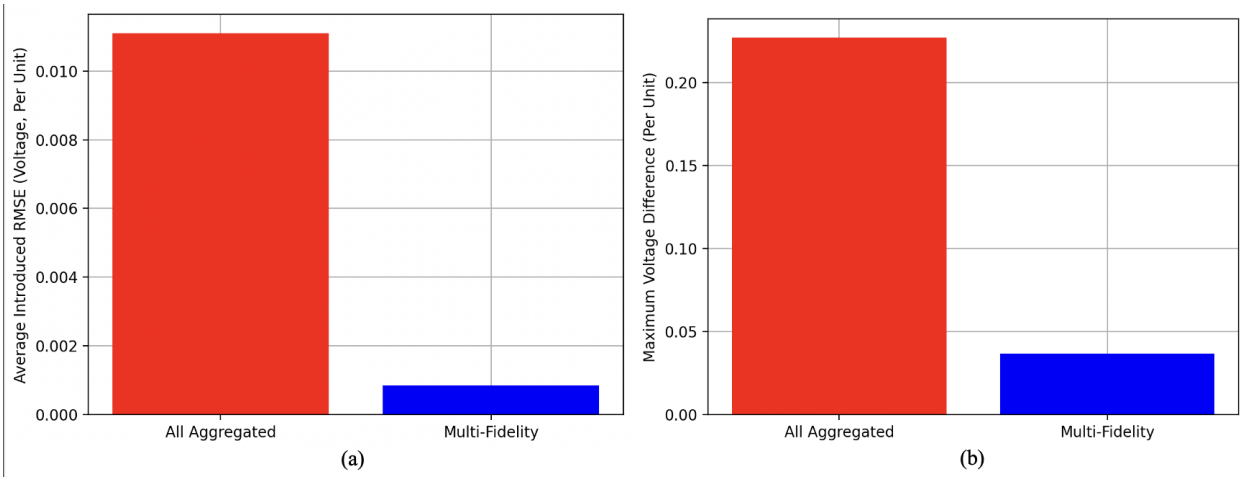


Figure 5.15: Error introduced when comparing the disaggregated modeling approach to the aggregated approach and the multi-fidelity approach, in terms of average RMSE (a) and maximum voltage difference (b)

little from the disaggregated approach in terms of simulation accuracy are ideal (the threshold of 1.0 pu). The results of such sensitivity analysis are displayed below in Fig. 5.16.

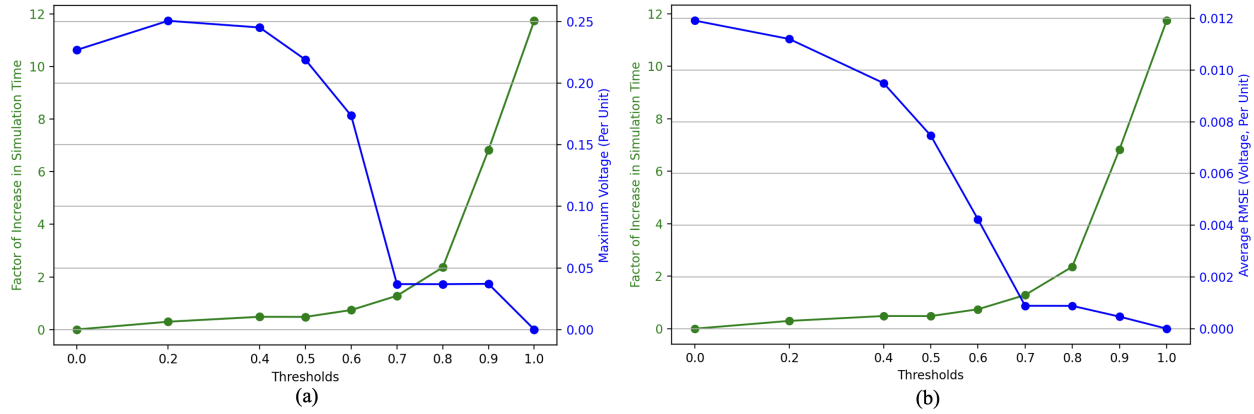


Figure 5.16: Sensitivity analysis associated with adjusting the threshold delineating between areas of disaggregation and aggregation for the multi-fidelity modeling approach

The fully aggregated approach has the fastest runtime, which is expected. As the voltage threshold moves from 0 (an all aggregated scenario) to about 0.4/0.5, there are only slight improvements in RMSE and the maximum voltage difference. This is because considering a threshold of 0.4 pu does not encapsulate many buses into the high impact region (a total of 3 out of a possible 40 load buses are modeled in disaggregation). As it is still a small number of added buses into the simulation, the runtime does not increase by much as well from the aggregated to the multi-fidelity approach.

In general, the increase in simulation runtime grows somewhat exponentially as the threshold increases. As the threshold moves towards 1.0, a greater and greater amount of buses are included in the high impact region, explaining the behavior displayed in Fig. 5.16. While the increase in

simulation time steadily increases with an increasing voltage threshold, there is a sharp distinction that occurs in terms of introduced error beginning as the threshold moves from 0.6 pu to 0.7 pu. Most likely this occurs as, for this particular test system, all DER_A models are parameterized with $Vl1 = 0.6\ pu$ (where voltage tripping begins). Thus, with an increase in the voltage threshold from 0.6 pu to 0.7 pu, the modeling of DERs that will begin to trip utilize a disaggregated feeder, allowing for the unique dynamics to be encapsulated.

Lastly, as seen in Fig. 5.16, there is a negligible difference in the maximum RMSE as the threshold moves from 0.7 pu to 1.0 pu. However, a somewhat considerable increase in simulation time does occur as a byproduct of this same change. This leads to the conclusion that the previously used voltage threshold of 0.8 pu was conservative; it sacrificed additional simulation runtime to ensure simulation accuracy. Note that an added bonus of the proposed method is this ability to natural increase simulation accuracy at the expense of simulation complexity if needed, as well as vice versa if desired. Therefore, many different use cases can exist for various kinds of studies by simply adjusting this threshold. For example, modeling a system where the user knows the majority of DERs are legacy (typically no fault-ride-through protocols), the user may decide to lower the voltage threshold because the tripping of DERs may not occur in the same manner as seen in this study. The proposed method easily allows for a change like this, removing any user intervention that would be otherwise necessary for construction of a multi-fidelity system.

5.5 Contingency List Using Three-Hundred Bus Transmission System with 50% DER Penetration

While the results from the single fault scenario above demonstrate the proposed method's performance, it should be verified that the approach works effectively for faults throughout large systems. For this testing, a 30 second simulation is conducted for varying faults found in places spread out across the IEEE 300 Bus System (reference Fig. D.3 in Appendix D.3 for a visual of their locations). Note that the majority of dynamically modeled loads are clustered in the center of the system; the effects of this system set up appear in the results.

First, the fault at Bus 38 is simulated. This bus is located in the center of the system, triggering many dynamic responses from the neighboring dynamic feeders in a similar manner to what was seen with the fault at Bus 45. The comparison of the proposed method (labeled "Multi-Fidelity") in respect to a simulation with all aggregated feeders, and another with all disaggregated feeders, shows again the excellent performance of the proposed method. Seen in Fig. 5.17, the trend when moving from the aggregated modeling approach to the multi-fidelity modeling approach is apparent in terms of error, reducing the average RMSE by over a factor of 6 and the maximum voltage difference by over a factor of 2 (with respect to the disaggregated simulation). At the same time, the simulation runtime is decreased by nearly a factor of 7, displayed in Fig. 5.18. Thus, the simulation runtime for the proposed method is much closer to the aggregated simulation compared to the disaggregated simulation, while also having substantially lowered maximum voltage difference and average RMSE across the system.

Next, the fault at Bus 246 is simulated. In contrast to the previous fault bus, Bus 246 is far away from the majority of the dynamic feeder locations. Because of this, all of the feeders are modeled

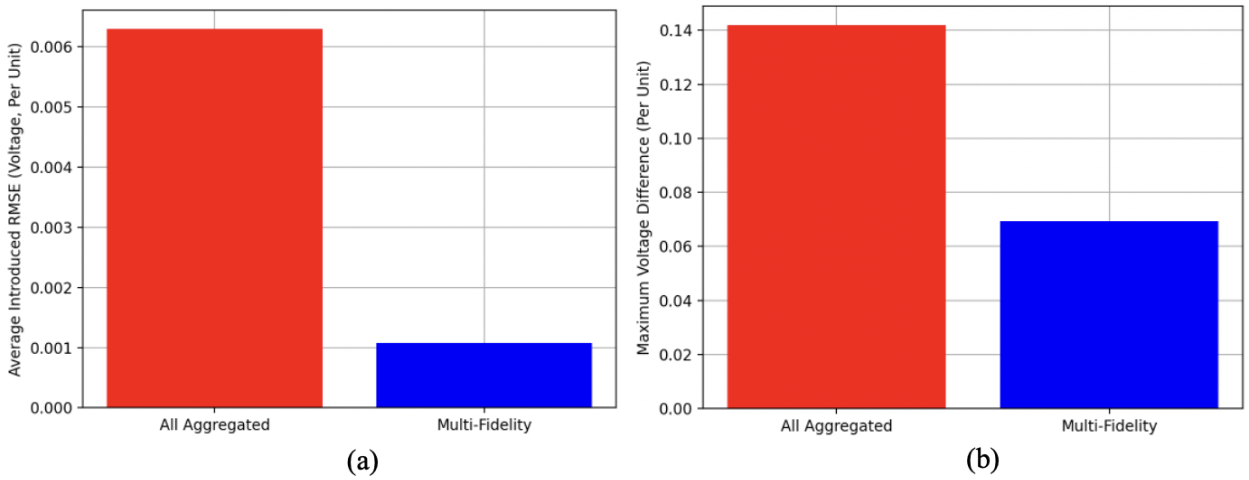


Figure 5.17: Error introduced when comparing the disaggregated modeling approach to the aggregated approach and the multi-fidelity approach in terms of average RMSE (a), and maximum voltage difference (b) due to a fault at Bus 38

in an aggregated manner in the proposed method as they fall outside of the high impact zone. Thus, the simulation ends up being the same for both the aggregated simulation and proposed method in Fig. 5.19, which is optimal as both solutions offer low voltage differences compared to the disaggregated simulation. This is key takeaway of the proposed method, as it can automatically adapt to become a fully aggregated simulation based on the fault location, encompassing negligible error in respect to the disaggregated simulation, while entirely removing the over 1200% increase in simulation runtime.

Five other fault locations are considered for analysis, however results do not offer much additional insight to the above fault locations. Thus, the statistics for these contingencies can be found in Tables D.1, D.2, D.3, D.4, and D.5, all located in Appendix D.4.

When running all of these contingencies in succession, the performance of the multi-fidelity modeling approach should be examined for its added computational cost as if it were a true contingency analysis. As the process of system building and performing short circuit analysis for each fault contingency injects an extra step in the usual contingency analysis process as shown in Fig. 5.2, it must not add in considerable computational effort. Otherwise, the whole goal of the customized feeder approach would be undermined.

On average across all of the above scenarios, it was found that the entire process of short-circuit analysis and system construction took 0.117 seconds. In the scheme of the disaggregated simulation lasting over 1.5 minutes (for the 30 second simulation time held in this analysis), this is a highly negligible amount of additional computational effort, thus demonstrating the effectiveness of the proposed method.

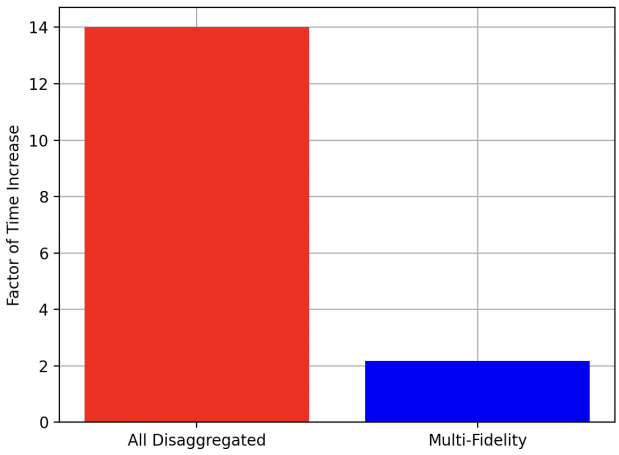


Figure 5.18: Simulation runtime increase when comparing the aggregated modeling approach to the disaggregated approach and the multi-fidelity approach due to a fault at Bus 38

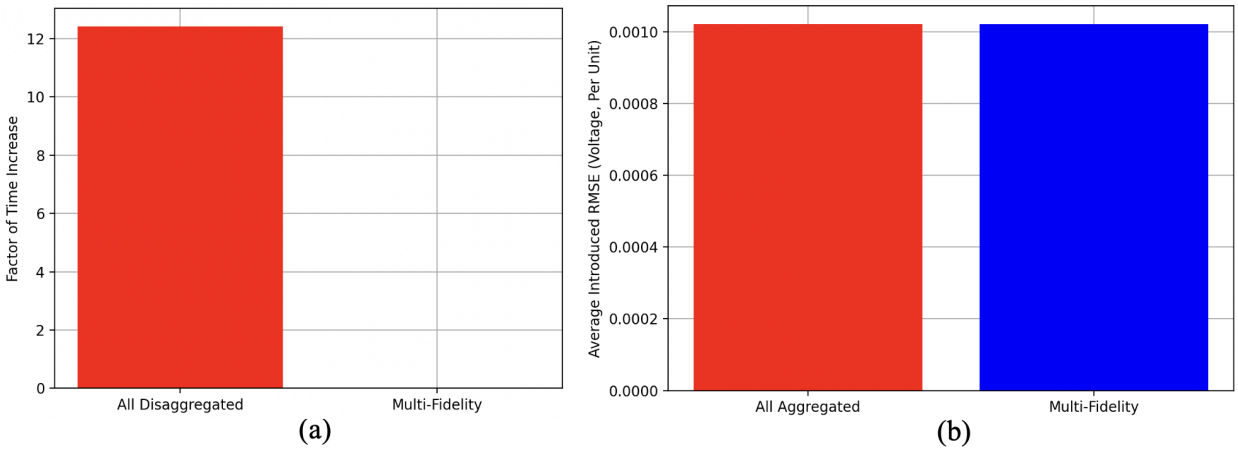


Figure 5.19: Error introduced when comparing the disaggregated modeling approach to the aggregated approach and the multi-fidelity approach (b), and simulation runtime increase when comparing the aggregated modeling approach to the disaggregated approach and the multi-fidelity approach (a) due to a fault at Bus 246

6. Conclusions and Future Work

This project addressed critical challenges arising from high penetrations of DERs in T&D systems. Current simulation practices often rely on model-fidelity-agnostic tools that are computationally inefficient and require manual, ad-hoc model reduction. Our work advances systematic, automated, and AI-enhanced solutions to make large-scale T&D dynamic studies feasible on conventional computing platforms.

Key outcomes include:

- **Aggregate DER reactive-power capability curves:** We developed a TSO–DSO framework that quantifies and coordinates aggregated DER VAR support, showing that sensitivity-based dispatch improves voltage control while reducing communication burden and reactive losses.
- **Data-driven reduced-order distribution modeling:** We demonstrated that delay-embedded DMD/Koopman techniques can identify interpretable reduced-order models under partial observability, enabling accurate transient stability assessments of DER-rich feeders.
- **AI and automation tools:** We built a fine-tuned LLM assistant for PSCAD EMT scripting that reduces hallucinations compared to general-purpose models, and a mobile–cloud tool ("GridScout") that streamlines field-to-model updates for OpenDSS-based distribution models.
- **Multi-fidelity T&D dynamic modeling and simulation:** We developed a contingency-aware simulation workflow that combines short-circuit screening with adaptive model selection. High-impact zones identified via short-circuit analysis are modeled in disaggregated detail, while low-impact areas remain aggregated. In Chapter 5, case studies on an integrated T&D system comprising the IEEE 300-bus transmission system with 50% DER penetration feeders showed that:

  1. The proposed multi-fidelity method reduced runtime by more than a factor of four compared to fully disaggregated simulations.
  2. Average RMSE in voltage trajectories was reduced by more than 10× and maximum bus voltage errors by more than 5× relative to a fully aggregated model.
  3. The method automatically adapts: for contingencies far from DER-rich feeders, results converge to those of an aggregated model, avoiding unnecessary computation.
  4. End-to-end system building and short-circuit screening added only 0.117 seconds of overhead, negligible compared to the 1.5 minutes required for a 30-second disaggregated dynamic simulation.

  Together, these results demonstrate that the multi-fidelity approach preserves accuracy where it matters, while cutting computational burden to make dynamic contingency analysis more practical.

Future Work

Several directions emerge from this research:

1. **Scalability:** Extend multi-fidelity and AI-accelerated co-simulation to larger, more realistic utility-scale T&D networks with diverse DER portfolios.
2. **Integration:** Embed reduced-order distribution models and aggregated DER capability curves into production-grade planning and operational tools used by ISOs and utilities.
3. **Tool enhancement:** Broaden the PSCAD assistant's scope to cover more device models and simulation workflows, and expand the GridScout tool to support additional data sources and automated validation.
4. **Field validation:** Collaborate with industry partners to validate proposed workflows on real-world feeders, quantify operational benefits, and refine algorithms based on practical constraints.

In summary, this work lays a foundation for practical, scalable, and intelligent T&D modeling and simulation, helping utilities and system operators harness DER flexibility while managing complexity and maintaining reliability.

Appendices

A. Implementation of Advanced Distributed Energy Resource Dynamic Model (DER_A)

Distributed energy resources (DERs) shift the generation of power from centralized resources to decentralized resources, coupling transmission and distribution systems. Given this coupling, their effects at the transmission level are a phenomenon that is growing along with their proliferation. Additionally, several new standards such as FERC Order 2222 [54] and IEEE Std. 1547-2020 [1] further increase the necessity of bulk power system studies/simulations with detailed, disaggregated DER models involved, as communication and interaction of transmission systems with distribution systems will naturally increase. However, DERs have highly active dynamic characteristics. Their addition into power markets and system studies does not come without corresponding complexity cost.

As their dynamics are closely tied to their terminal voltage, modeling DERs in aggregation may misrepresent their true dynamic behavior [55]. This is because voltage can vary highly along different locations in a distribution feeder, and as dynamic are coupled to terminal voltage, a DERs true location along a feeder is a crucial detail to model. Some unique dynamic behaviors tied to terminal voltage includes newfound grid control protocols, such as voltage-based reactive power injection (Volt/VAR control), mandatory voltage ride through behaviors, device tripping, and much more. The majority of DERs implemented now include these grid controls, and regulations also mandate them such as IEEE 1547. Therefore, the accommodation of these effects must be found in a DER simulation model.

A.1 Background of Distributed Energy Resource Models

In a dynamic contingency analysis setting, simulations are generally conducted in the phasor domain as opposed to an EMT simulation. Where EMT simulations record physical sinusoids of the system, a phasor domain simulation computes time evolving phasors at each timestep. While EMT simulations can model unique effects and are crucial in some scenarios, for the purpose of dynamic contingency analysis, a phasor-based solution suffices as the system computational complexity is not nearly as intense. Therefore, it is the modeling method of choice when it comes to utilities.

The DER_A model [53] is a phasor-domain dynamic model, meant to act as an aggregation of several DERs. This could be a suburban area with many rooftop solar systems, an area with several smaller generation sources, among many others. The DER_A model is a widely used model in power system studies, for the numerous dynamic effects it incorporates. A.1 outlines other typical DER models that are currently employed by utilities, along with the behaviors they encompass. Notice the added dynamic effects the DER_A encompasses. Because of this, the use of the DER_A model is becoming growing in necessity and therefore is a commonly used model in practice.

Table A.1: Varying DER Models

Behavior	**Controlled Current Source**	**PVD1 [51]**	**DER_A [53]**
Volt/VAR Control	No	Unidirectional	Yes
Power Factor Control	No	No	Yes
Active Power Recovery	No	No	Yes
Droop Control	No	Unidirectional	Yes
Tripping and Reconnection	Yes	Yes	Yes
Timers for Tripping	No	No	Yes
Network Interface	Current Injection	Current Injection	Voltage Source

The DER_A model provides the dynamic characteristics that system planners and operators need for modern power systems by accommodating all of the unique controls listed in A.1. Therefore, for detailed DER modeling and studies, it must be utilized.

The simulation tool used throughout this thesis is InterPSS, as previously mentioned. This tool did not have the DER_A model for studies (only the PVD1), yet it must be used in the final application in order to provide an accurate proof of concept of the proposed method. Otherwise, the unique dynamic effects of modern DERs would not be accounted for, obsoleting any results gathered. For this reason, a model has been constructed in InterPSS. This chapter outlines the process of constructing this model for use in InterPSS, from translation of block diagrams into code and how the DER_A model communicates with the dynamic simulation solver that InterPSS utilizes.

A.2 Power System Dynamic Modeling Algorithm

As mentioned in the introduction, a common method of dynamically simulating a power system is via the partitioned approach. This consists of two equations; one differential equation and another algebraic equation. First, the algebraic (network) equation is solved iteratively, using current injections from all devices in the system. Then, the differential equation is solved through a method of numerical integration, in order to proceed to the next timestep. This process repeats until the total length of time determined in the dynamic simulation is reached.

The manifestation of the partitioned approach into actual software will naturally vary from simulation tool to simulation tool. In terms of the code used by the simulation engine, these differences may simply how the system solver interacts with it's models. Also, they could differ in respect to methods of numerical integration. However, the overall algorithm to solve the partitioned set of equations above is generally equivalent across simulation platforms. The utilized numerical integration method in InterPSS is the Modified Euler's Method; here, there are two distinct stages to compute the numerical integration. In the general case of a first order transfer function, the mathematics are as follows. In the first step (predictor step), the next value of the output, $y_{pred}[n]$, is computed using the previous output, $y_{out}[n-1]$, the current input $y_{in}[n]$, the time constant τ,

and the time step size h as follows.

$$y_{pred}[n] = y_{out}[n-1] + h\frac{y_{out}[n-1] - y_{in}[n]}{\tau} \tag{A.1}$$

Now that a new value of the function has been computed, it can be seen that the derivative used in the previous step, $\frac{y_{out}[n-1]-y_{in}[n]}{\tau}$, uses the value of y from the previous time step. Now that a new value of y is computed, this derivative is now better represented by using this updated value, $y_{pred}[n]$. Therefore, the Modified Euler's Method employs a corrector step, which now uses the average of these two slopes to better estimate the current value of y. The more accurate next value of the output, $y_{out}[n]$, is computed using the previous output, $y_{out}[n-1]$, the predictor step's output, $y_{pred}[n]$, the current input $y_{in}[n]$, the time constant τ, and time step size h as follows.

$$y[n] = y_{out}[n-1] + \frac{h}{2}(\frac{y_{out}[n-1] - y_{in}[n]}{\tau} + \frac{y_{pred}[n] - y_{in}[n]}{\tau}) \tag{A.2}$$

These are the two stages in the Modified Euler's Method, to give an accurate value of $y[n]$. For eventual implementation into InterPSS, the predictor step is slightly adjusted via substituting the value of $y_{out}[n-1]$ from Equation A.2 in for $y_{out}[n-1]$ from Equation A.1, as the previous value of y is not known between successive steps. However, the previous derivative from A.1 is stored internally in the model for use. Therefore, the predictor step becomes:

$$y[n] = y_{pred}[n] + \frac{h}{2}(\frac{y_{pred}[n] - y_{in}[n]}{\tau} - \frac{y_{out}[n-1] - y_{in}[n]}{\tau}) \tag{A.3}$$

Lastly, InterPSS does not compute Equation A.1 and immediately compute A.3. The network solution instead converges based off the results of Equation A.1 in between, which means the input y_{in} changes between Equation A.1 and Equation A.3. Therefore, the final equation used for the corrector step uses the y_{in} value found after the network solution converges due to the predictor step in order to compute the new derivative. The final equation used in shown below, where the updated input from the predictor step's network solution is denoted as $y_{in,pred}[n]$.

$$y[n] = y_{pred}[n] + \frac{h}{2}(\frac{y_{pred}[n] - y_{in,pred}[n]}{\tau} - \frac{y_{out}[n-1] - y_{in}[n]}{\tau}) \tag{A.4}$$

The general process for solving each time step in a dynamic simulation is shown in A.1. The process utilized in InterPSS is used as the reference for this algorithm.

Notice the partitioned nature of the algorithm, solving the network solution and integration steps separately. This is realized through separate functions, or in an object-oriented sense, methods, that perform each task outlined above. The following is how the DER_A model was constructed to interact with InterPSS, subject to the protocol outlined in A.1.

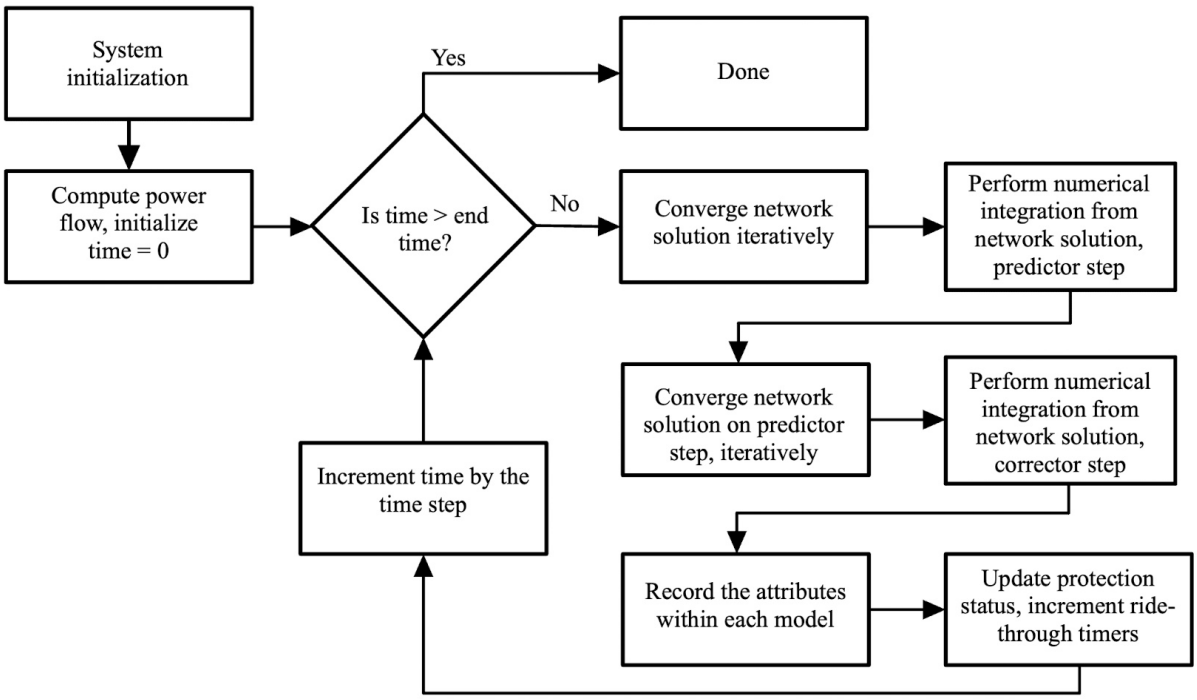


Figure A.1: The algorithm used by InterPSS for dynamic simulation

A.3 DER_A Model Subsystems

There are several subsystems that comprise the DER_A model. The majority of these subsystems are responsible for implementing the roles mentioned in A.1, along with several others. Overall, the DER_A model takes the terminal voltage, V_term, and terminal frequency, f_term, as input, and calculates an output phasor voltage to be placed behind an impedance, X_e. The overall system for the DER_A can be split up into the following subsystems; Volt/VAR Control, Frequency/Watt (Freq/Watt, or Droop) Control, Reference Reactive Current Generator, Reference Active Current Generator, Active and Reactive Current Generator, as well as Voltage and Frequency Logic. A.2 displays a visual these subsystems interacting to comprise the whole model. Note that all variables here, and later, use underscores as opposed to subscripts; this is to stay consistent with the code implementation that is shown throughout this section. Additionally, this model uses parameters from the Park/Clarke transform introduced in the introduction. However, note that the use of subscript p in the model coincides with the direct axis, d. The use of the subscript p is used for the clearer interpretation of active power, commonly referred to as P. Also, for numerical integration, the given code performs the predictor step if a binary variable `flag` is 0, and performs the corrector step if `flag` is 1. This binary variable is given to the model from the simulation solver, which will be covered later.

The values of V_term and f_term are the terminal voltage and frequency, respectively. These values are retrieved from the bus at which the DER model is attached to; in A.2, this would be the bus directly beside the overall distribution system. The values of V_meas and f_meas are

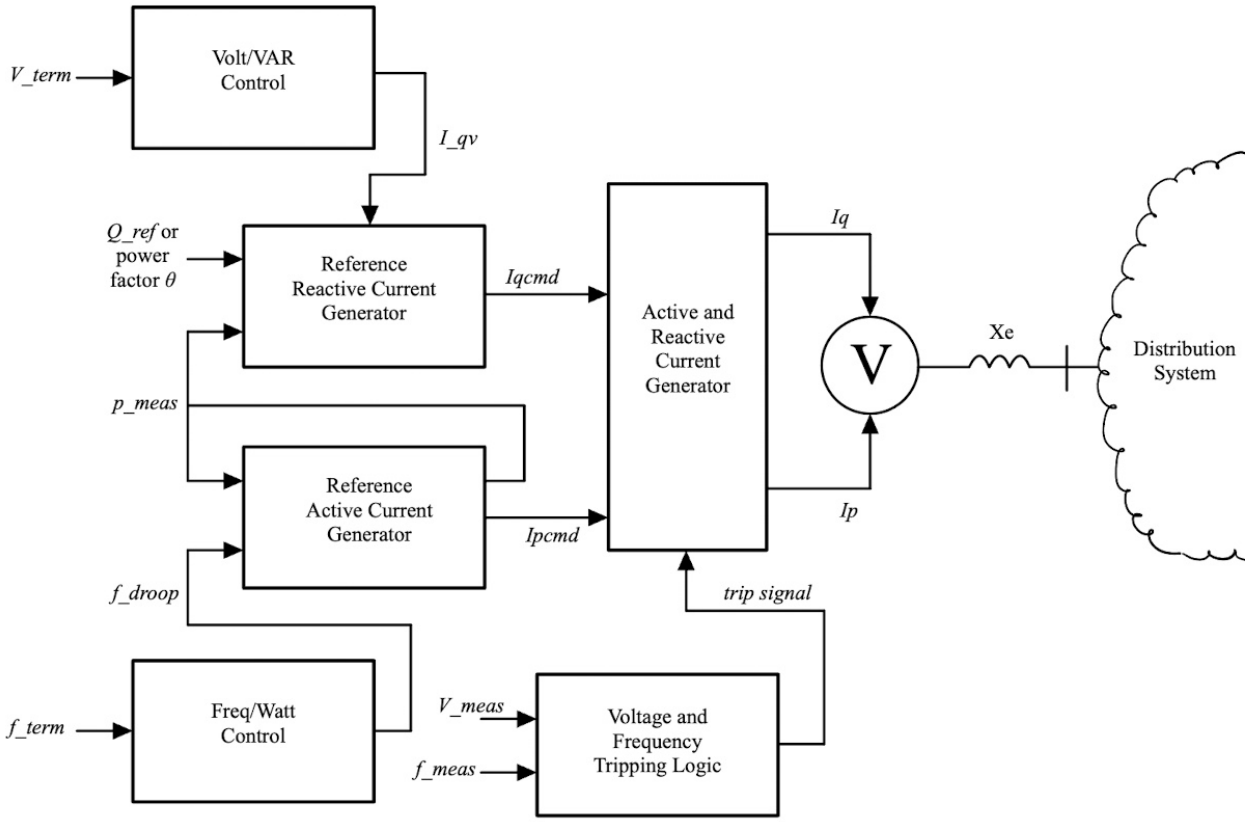


Figure A.2: The subsystems of the DER_A model

internal states within the Volt/VAR Control subsystem and the Freq/Watt subsystem, respective filtered terminal values. Note that in this chapter, droop control and Freq/Watt Control are used interchangeably, both referring to the subsystem labeled "Freq/Watt Control" in A.2 in which active power is adjusted based on system frequency.

A.3.1 Voltage-Based Adjustable Reactive Power Control

A widespread grid control technique for DERs is to inject or absorb reactive power, Q, based on its terminal voltage. This technique is commonly referred to as Volt/VAR Control. In this control scheme, a linear relationship between the injected/absorbed Q and terminal voltage is constructed in a similar manner as A.3.

The origin of A.3 would be $(1, 0)$, where the x-value is the per unit terminal voltage, and the y-value is the adjusted reactive power injection. The threshold Vh would typically be a value such as 1.1 pu, meaning at this voltage, the DER would absorb $Qmax$ VARs of reactive power. The threshold of Vl would typically be a value of 0.90 pu, meaning at this voltage, the DER would inject $Qmax$ VARs of reactive power. Note that A.3 uses the notation of negative power to be power that is injected into the system, and positive power to be power that is absorbed from the system.

The block diagram used to encapsulate Volt/VAR Control is shown below in A.4. With the input

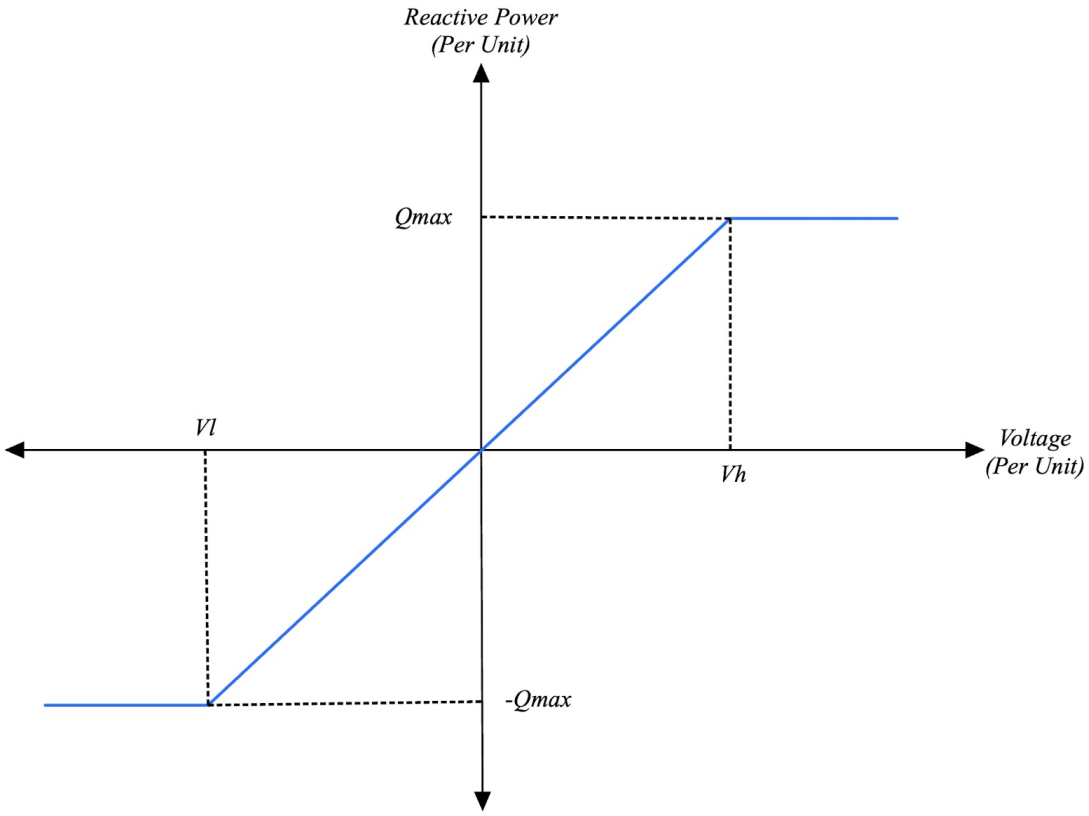


Figure A.3: Generic Volt/VAR curve used in DERs

V_term (the terminal voltage) and a constant V_ref (reference or desired voltage), an output I_qv is computed. This I_qv is the amount of reactive current for the model to inject, based solely due to terminal voltage (not including the reference reactive power). First, the difference between the terminal voltage and the reference voltage is computed. This error is passed through a deadband with parameters $dbd1$ and $dbd2$, where the output of this deadband, V_err is defined by the piecewise function in Equation A.5. Code implementation of this deadband (and all future deadbands) can be found in Appendix B.1.

$$V\_err = \begin{cases} 0, & dbd1 < (V\_ref - V\_meas) < dbd2 \\ V\_ref - V\_meas - dbd1, & (V\_ref - V\_meas) < dbd1 \\ V\_ref - V\_meas - dbd2, & (V\_ref - V\_meas) > dbd2 \end{cases} \tag{A.5}$$

The signal V_err is then passed through a proportional control block, which is specified by a gain of Kqv. Finally, this output is bounded by the maximum value of $Iqh1$ and the minimum value of $Iql1$. In this manner, the output, I_qv is computed as a function of the difference between the terminal voltage and the desired reference voltage. The code implementation of this block diagram can be found in Appendix B.2.

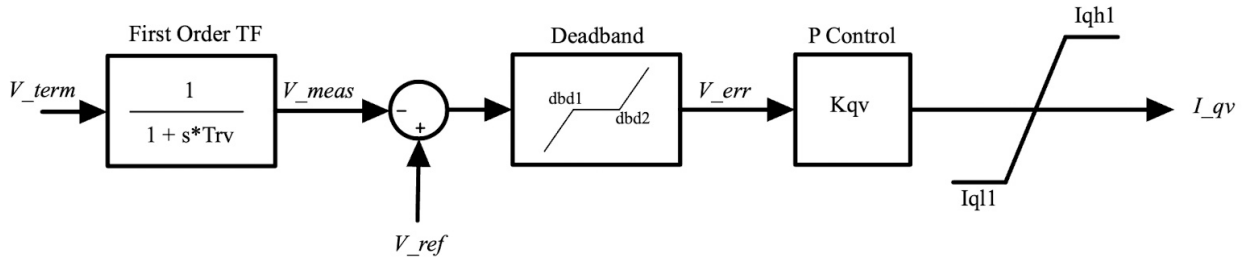


Figure A.4: Block Diagram of Volt/VAR Control

A.3.2 Frequency-Based Adjustable Active Power Control (Droop Control)

A behavior already implemented in conventional generators is droop control, where, based on the system frequency, the output active power, P, is adjusted in an attempt to balance power generation and consumption. In the DER_A model, this is accomplished in a similar manner, seen in A.5.

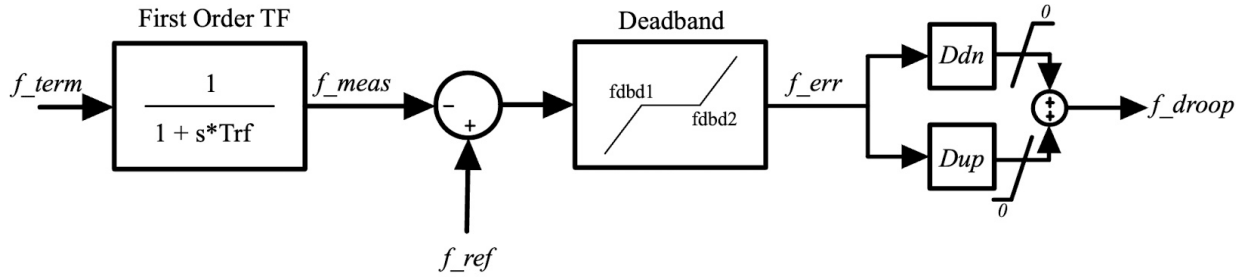


Figure A.5: Block diagram of droop control

Here, the frequency measured at the DER's bus is taken as input, f_term, and an error signal is formed, f_err. This error is passed through a deadband, which functions in the same way as the piecewise function in Equation A.5, except with parameters $fdbd1$ and $fdbd2$. Then, a proportional gain is used to calculate the adjusted P, f_droop, from the frequency error.. The up and down droop constants, Dup and Ddn respectively, can be selectively customized to the model. Although, the down droop is limited by zero if the measured frequency is larger than the reference, and similarly the up droop is limited by zero if the measured frequency is smaller than the reference. In this manner, the output signal from the droop control is only influenced by the down droop gain or the up droop gain, never both. The code implementation of this subsystem is found in Appendix B.3.

A.3.3 Active Current Injection Control

Based on the desired active power injection of the DER, controls need to be put in place to ensure the appropriate active current, Ip is injected. Additionally, the signal from the droop control needs to be factored in, such that the active power injection can change based off the value f_droop from before. Also, the model should attempt to bring the system back to f_ref, which is possible with an integral controller. In the DER_A model, this is accomplished via the block diagram shown in

A.6.

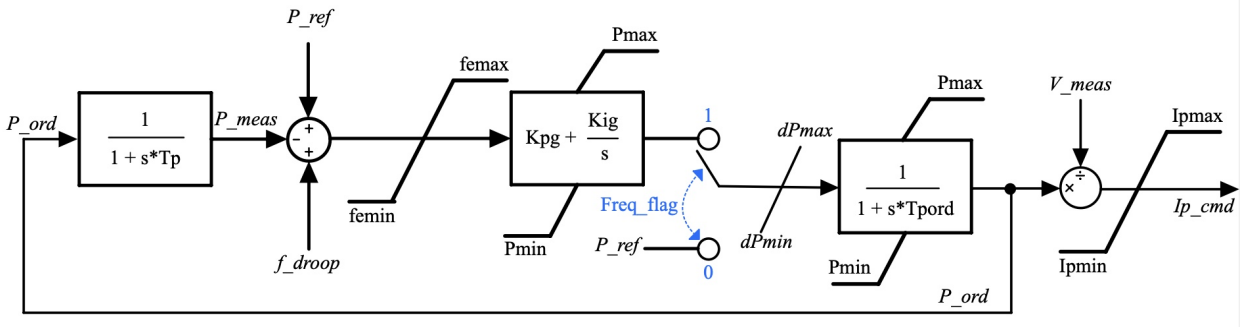


Figure A.6: Block diagram for control of active current injection

This control scheme accomplishes several things. To start, it forms an error signal between the filtered ordered power, P_meas, and the reference power, P_ref, adjusted by the droop control signal, f_droop. This error signal is bounded between the parameters $femax$ and $femin$. Then, the bounded error signal is passed through a proportional-integral (PI) controller, giving a corresponding power output signal which is bounded between $Pmax$ and $Pmin$. The rate of change of this output signal is also bounded between $dPmax$ and $dPmin$. Lastly, this desired power output is filtered and bounded once again between $Pmax$ and $Pmin$, yielding the ordered power, P_ord. The final commanded active power current injection, Ip_cmd, is computed via $\frac{P\_ord}{V\_meas}$, which is also bounded by $Ipmax$ and $Ipmin$.

Finally, the binary parameter $Freq\_flag$ controls whether the model operates with the influence of droop control and reference power error, or solely off reference power. When $Freq\_flag$ is set to 0, the reference power, P_ref, is passed directly through for use to calculate Ip_cmd. When $Freq\_flag$ is set to 1, the error signal formed by $P\_ref - P\_meas + f\_droop$ is passed through for use to calculate Ip_cmd. Through this behavior, the influence of the droop control can be switched on or off by adjusting the parameter $Freq\_flag$. The code implementation of the overall subsystem is found in Appendix B.4.

A.3.4 Reactive Current Injection Control

The Volt/VAR control scheme, seen before, injects reactive power based on terminal voltage. To implement this into a model where it is possible for a nonzero amount of reactive power to be desired at nominal voltage, the following block diagram is used in A.7.

Here, the parameter Pf_flag is a binary value, where a reference reactive power, Q_ref, is passed for calculation when $Pf\_flag = 0$. When $Pf\_flag = 1$, the model is in a constant power factor mode. The power factor angle, denoted as θ in A.7, is used to calculate the necessary reactive power based on the active power injected by the model, through $Q = P \tan\theta$. Regardless of Pf_flag, this value of reactive power is divided by the filtered voltage, V_meas, to retrieve a value for reactive current. This value is then passed through a filter. Subsequently, this is added to the output from the Volt/VAR Controls, I_qv. Finally, this total is bounded from $Iqmin$ to $Iqmax$, yielding the desired reactive current injection, Iq_cmd. The code implementation of this block diagram is shown in the

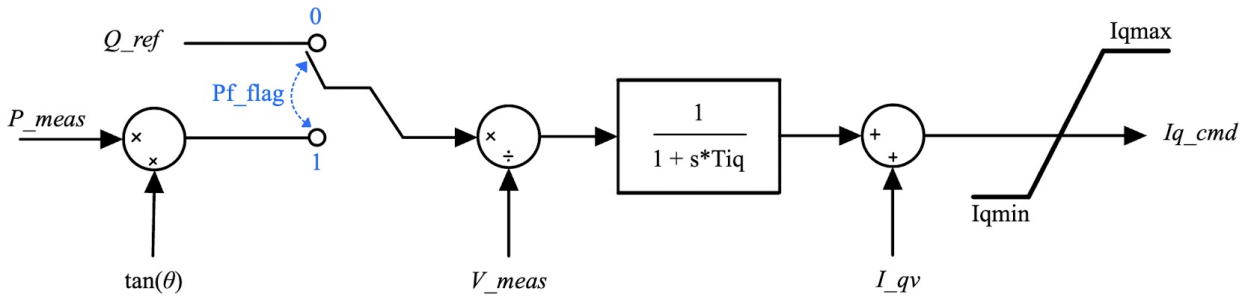


Figure A.7: Block diagram for control of reactive current injection

listing in the Appendix B.5.

A.3.5 Voltage Source Calculation

Through the above subsystems, the desired active power portion of current, $Ipcmd$ and the desired reactive power portion of current, $Iqcmd$, are generated. From these two values, an equivalent internal voltage is calculated to interface with the rest of the system.

First, the values of reactive and active current commands are adjusted based on the voltage and frequency tripping status, $vMult$ and f_relay. These values are then filtered to give Ip and Iq. The output Ip also has a bidirectional ramp rate limit applied, specified by $rrpwr$. With these two values, the internal voltage is computed as follows:

$$V_{int} = (V\_term, d - Iq * Xe) + j(V\_term, q - Ip * Xe) \tag{A.6}$$

Here, Xe is a parameter representing the model internal impedance. V_term, d and V_term, q are the components of the terminal voltage after the Park Transform (previously, V_term is the vector sum of these two values) . This final process is outlined in the block diagram shown in A.8, where the bolded **V** represents V_{int}.

The tripping signals $vMult$ and f_relay are values between 0 and 1, indicating the model has tripped if either is a 0. While f_relay is a binary variable (0 for a tripped model, 1 for an non-tripped model), $vMult$ allows for fractional tripping. This means that it can range anywhere between 0 and 1, dependent upon the present circumstance and previous terminal conditions. The code implementation of this final subsystem is shown in Appendix B.6.

A.3.6 Voltage and Frequency Tripping Protocols

The DER_A model has a unique method for modeling scenarios where a fraction of units have tripped during some contingency, but not all. This behavior is displayed in A.9, for the under-voltage scenario. Note that this behavior is reflected in the same manner for an over-voltage scenario, except with parameters $Vh0$ and $Vh1$, along with the maximum voltage value $Vmax$.

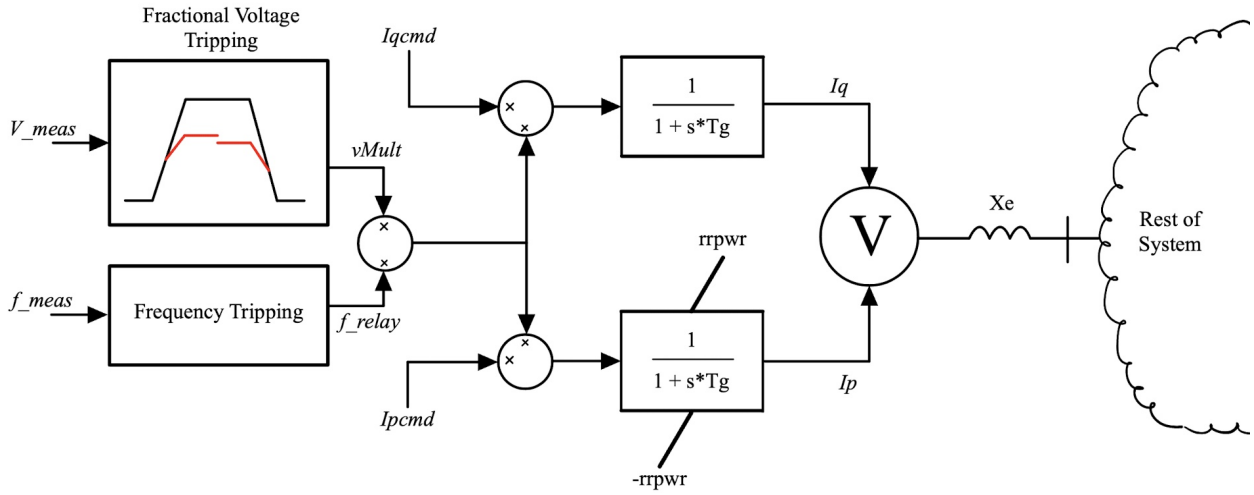


Figure A.8: Block diagram for the interface between the DER_A model and the rest of the system

The procedure is as follows; from initialization, the tripping signal tracks on the black curve (the fraction of units that are online are 1, or 100%). If the filtered terminal voltage (V_meas) drops below $Vl1$ for a duration greater than the parameter $tvl1$, then the tripping signal will track along the red curve upon voltage recovery. During the period of time where V_meas stays under $Vl1$, $Vmin$ is being assigned to V_meas. The moment the timer expires, $Vmin$ is permanently assigned to that value of V_meas, and the device begins tracking along the red curve. The fraction of devices that recover from this point is indicated by the parameter $Vrfrac$. In other words, if the voltage falls below $Vl1$ for greater than $tvl1$ seconds, then $Vmin$ is assigned to V_meas at that instant and only $Vrfrac$ of the currently tripped models recover upon voltage recovery. Thus, the flat red portion of A.9 is dynamically moving throughout the simulation based on the drop in voltage. Also, if V_meas drops below $Vl0$ for a duration greater than the parameter $tvl0$, then the device will have completely tripped; there will be no reconnection upon voltage recovery. This exact same behavior is also reflected for over-voltages, simply mirrored. Final code implementation of this protocol can be found in Appendix B.7.

A.3.7 Maximum Current Values in P and Q Priority

The values of $Ipmax$, $Iqmax$, $Ipmin$, and $Iqmin$ are not static throughout the simulation. These values change based on if the model is operating with P (active power) priority, or Q (reactive power) priority. For each time step, these values in P priority are:

$$Ipmax = Imax$$
$$Iqmax = \sqrt{Imax^2 - Ipcmd^2}$$
$$Iqmin = -Iqmax$$

Through these equations, the active power component of current is prioritized by limiting Iq based

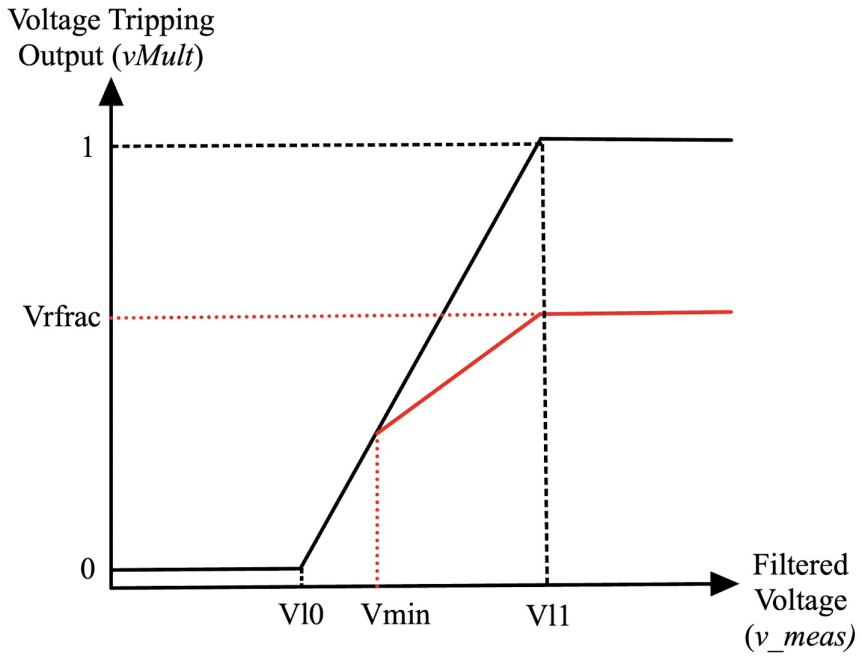


Figure A.9: Behavior of voltage tripping protocol in the DER_A model

off of $Ipcmd$. Similarly, in Q priority, the maximum and minimum values are:

$$Iqmax = Imax$$
$$Ipmax = \sqrt{Imax^2 - Iqcmd^2}$$
$$Iqmin = -Iqmax$$

The model is switched between these two modes via the parameter $PQFlag$, a binary variable where 0 indicates Q priority, and 1 indicates P priority.

A.4 Implementation of DER_A Model into the InterPSS Dynamic Simulation Algorithm

While the above block diagrams can carry out the functions of the DER_A model, it must properly communicate with the power system solver to encapsulate the correct dynamic behaviors. The following sections outline how various methods were written for the InterPSS dynamic simulation solver to interact with.

A.4.1 Implementation of `getOutputObject()` Method

The main method used by InterPSS for communication between the system and it's models is `getOutputObject()`. This method retrieves the current injection from a model, for use in the iterative network solution routine. When this method is called in a model, its should return the

norton equivalent current injection into the system, based off the updated terminal conditions from the last iteration in the network solution. It should be noted that the internal states of the model should not change during each call of `getOutputObject()`, as the next time step has not yet occured. In this manner, the model and the system can be solved iteratively until convergence.

One caveat of the implementation into InterPSS is that this method asks for the norton equivalent current of the model, not the internal voltage. This is contrary to A.8, where the DER_A interfaces with the system as a voltage source behind an impedance. To mitigate this discrepancy, the equivalent voltage source is created, and subsequently the norton current is calculated from it for use in the model. As the thevenin equivalent of the model (the internal voltage) can be directly translated into the norton equivalent via,

$$I_{nort} = \frac{V_{thev}}{jX_e} \tag{A.7}$$

the corresponding norton equivalent can be returned to the system solver without a change in the model characteristics. The only sacrifice this brings are convergence drawbacks, which could be pronounced if the power injection from these devices is large. Regardless, for the sake of implementation into InterPSS for use in the final study, using the equivalent norton current source suffices.

The purpose of the `getOutputObject()` method is to provide the norton current source to the system solver. The norton current source is computed by using the most recent values of Ip and Iq from A.8, by first finding the thevenin equivalent or internal voltage. As such, this method can be scripted as shown below.

```
public Object getOutputObject() {

    // compute internal voltage, shown in the final subsystem code implementation
       (Portion after calculating Ip and Iq in Appendix A.6)
    // *** NOTE *** computing the internal voltage does not compute a new value
       of Ip and Iq. The values of Ip and Iq are calculated ONLY through the
       nextStep() method. nextStep() computes this.Ip and this.Iq - the system
       will converge to these values by adjusting the terminal voltage as shown
       below, using this method.

    // compute norton equivalent from this internal voltage
    Complex nortCurSource = getInternalVoltage()/(new Complex(0,this.Xe));
    setNortonCurSource(nortCurSource);

    // return the norton equivalent current source as the object
    return getNortonCurSource();
}
```

During each iteration in the network solution, the above code retrieves the positive sequence

bus voltage (at which the DER is connected), and computes the internal voltage values Ed and Eq. These two values represent the real and imaginary parts of the internal voltage, respectively. Subsequently, the angle of the voltage phasor at the parent bus is used to convert the internal values from the dq domain, into the system rx domain. From the system reference frame internal voltage, the corresponding norton equivalent can be calculated. This result of this is returned. This method allows for system convergence by retrieving the bus voltage and angle from the previous iteration, and updating it's current injection accordingly.

A.4.2 Implementation of `nextStep()` Method

In after each network solution, the method used to proceed to the next time step is `nextStep()`. This method is responsible for computing the set of differential equations in the system. When this method is called, the internal states of the model should be updated through numerial integration. Here, InterPSS converges the network solution at both the predictor and correcter steps. First, the internal model states are computed using the predictor step from Equation A.1 only. The network solution converges based on the corresponding values of Ip and Iq from the model. Subsequently, the internal model states are updated using the corrector step of Equation A.4 and the updated terminal conditions from the network solution of the predictor step. Here, the next time step occurs.

Implementation of this technique requires the knowledge of whether the model should update the internal states via the predictor step or the corrector step. This is accomplished via the method parameter `flag`; a binary variable indicating whether the model should compute the predictor step (`flag = 0`), or whether the model should compute the corrector step (`flag = 1`). Additionally, computing Equations A.1 and A.4 require the step size, `dt`. Both `flag` and `dt` are passed to `nextStep()` as parameters.

As the internal states of the model are being updated, the block diagrams found in A.6, A.5, A.7, A.4 are being computed during `nextStep()`. This can be seen in the below code implementation, along with the numerical integration.

```
public boolean nextStep(double dt, int flag) {

    // retrieve the terminal voltage and frequency
    this.vt = this.getDStabBus().getVoltageMag();
    this.freqPU = this.getDStabBus().getFreq();

    // perform volt/VAR subsystem code (Appendix A.2)
    // perform freq/Watt subsystem code (Appendix A.3)
    // perform active current reference subsystem code (Appendix A.4)
    // perform reactive current reference subsystem code (Appendix A.5)
    // perform Ip and Iq calculation (Up through Ip and Iq calculation in
       Appendix A.6)
    // *** NOTE *** This step computes the values up until the internal voltage
       computation in Figure 4.8. It does NOT update the internal voltage.
       getOutputObject() will update the internal voltage
```

```
    return true; // signify computation of Ip and Iq is completed
}
```

A.4.3 Implementation of `updateAttributes()` Method

After both the network solution and internal states have been solved via `getOutputObject()` and `nextStep()`, that individual time step has found a solution point. Therefore, the status of the model in terms of its attributes (tripped status, power injection, etc.) can be updated. This is accomplished through the method `updateAttributes()`. When this method is called by the solver, the internal attributes of the model are computed and stored for analysis.

For the prupose of the DER_A model, the only values that should be updated here are the power injection of the model and the values of Ip and Iq. This is accomplished in the following code implementation.

```
public boolean updateAttributes() {
    setPosSeqIpq(new Complex(this.Ip, this.Iq)); // update the current state of
        Ip and Iq
    setPosSeqGenPQ(getPosSeqIpq().multiply(this.vt)); // update the current state
        of the output P and Q
    return true;
}
```

A.4.4 Implementation of `afterStep()` Method

Finally, with all the previous methods called (the network solution has been solved, the next time step derivatives have been computed, and all the model's attributes updated), the internal timers in the models are updated for use in the protection settings. This is done via the `afterStep()` method. When this method is called, the protection schemes in the corresponding model are updated, to see if the model has tripped or not (or otherwise update the status of the protections accordingly). With this method called, the solver has completed the process for the individual time step, and we perform the same sequence of method calls for the next time step.

The voltage tripping scheme of this model encompasses fractional model tripping, to represent if the model is serving as an aggregated model. This behavior was examined in Section A.3.6, where only a fraction of the previous power output of the device following an event could remain upon voltage recovery. The code to implement this tripping scheme can be found in Appendix B.7.

The frequency tripping logic is simple; if the terminal frequency drops below the parameter $fltrp$ for a duration of tfl seconds, the entire model is tripped. In addition, if the terminal frequency drops below the parameter $fhtrp$ for a duration of tfh seconds, the entire model is tripped. If none of these are true, nothing happens. The code to implement this logic can be found in Appendix

B.8.

Additionally, the maximum and minimum limits for Ip and Iq must be updated here for use in the next time step. The logic for this process was outlined in Chapter A.3.6. These maximum values depend on a binary variable, `PQFlag`, as well as the previously computed values of $Ipcmd$ or $Iqcmd$. If `PQFlag = 0`, the maximum value of $Iqcmd$ is set to the maximum current output of the device, $Imax$. The maximum value of $Ipcmd$ is then set via $Ipcmd = \sqrt{Imax^2 - Iqcmd^2}$. Likewise, if `PQFlag = 1`, the maximum value of $Ipcmd$ is set to the maximum current output of the device, $Imax$. The maximum value of $Iqcmd$ is then set via $Iqcmd = \sqrt{Imax^2 - Ipcmd^2}$. The code implementation of this scheme can be found in Appendix B.9.

Lastly, the value of the maximum power ramp rate, $rrpwr$, is updated based on the current sign of Ip. This is because $rrpwr$ represents an absolute value rate limit. Therefore, if Ip is positive, $rrpwr$ limits a rise in a positive direction; however, any magnitude of drop in Ip is not influenced by this parameter. This behavior is reflected when Ip is negative as well.

Overall, the method is implemented as follows. The functions used to carry out these protection schemes can be found in Appendix B.

```
public boolean afterStep(double dt) {
    incrementCurrSimuTime(dt); // increments the internal simulation time
    voltageTripLogic(); // Appendix A.7
    freqTripLogic(); // Appendix A.8
    updateIdIqMax(); // Appendix A.9
    update_rrpwr(this.Ip); // Appendix A.10
}
```

Verification of Constructed Model

Now that the model has been scripted, it must be verified for correctness prior to implementation in any studies. To accomplish this, the terminal conditions are adjusted dynamically in a standalone case. The above methods in the InterPSS model are called in the exact same manner as the actual dynamic solver, allowing for proper testing. The internal states and the output active and reactive power are analyzed for correctness in several test cases.

A.2 outlines the various tests conducted on the constructed DER_A model. Scenarios of over-voltage, under-voltage, over-frequency, and under-frequency are simulated to verify ride-through behaviors, Volt/VAR control, and Frequency/Watt control. Here, the reference power is 50 MW on a 100 MVA base, and thus the power injection is 0.5 pu at steady state. The max power output $Pmax$ is set to 1.25 times this value, so seen in the testing results is a maximum power of 0.625 pu. This setup is consistent through all tests.

Table A.2: Varying Tests Conducted on the DER_A Model

Test ID	Test Type	Scenario	Goal of Test
1.1a	Over-Voltage	Terminal voltage set to 1.2 pu for a duration of 0.07 seconds	Volt/VAR Control, model should not trip
1.1b	Under-Voltage	Terminal voltage set to 0.8 pu for a duration of 0.07 seconds	Volt/VAR Control, model should not trip
1.2a	Over-Frequency	Terminal frequency is set to 1.03 pu for a duration of 0.07 seconds	Frequency/Watt Control, model should not trip
1.2b	Under-Frequency	Terminal frequency is set to 0.975 pu for a duration of 0.07 seconds	Frequency/Watt Control, model should not trip
2.1a	Over-Voltage	Terminal voltage is set to 1.25 pu for a duration of 0.225 seconds	Volt/VAR Control, model should trip entirely
2.1b	Under-Voltage	Terminal voltage is set to 0.3 pu for a duration of 0.225 seconds	Volt/VAR Control, model should trip entirely
2.2a	Over-Voltage	Terminal voltage is set to 1.19 pu for a duration of 0.225 seconds	Volt/VAR Control, model should trip partially
2.2b	Under-Voltage	Terminal voltage is set to 0.48 pu for a duration of 0.225 seconds	Volt/VAR Control, model should trip partially
2.3a	Over-Frequency	Terminal frequency is set to 1.03 pu for a duration of 0.225 seconds	Frequency/Watt Control, model should trip entirely
2.3b	Under-Frequency	Terminal frequency is set to 0.96 pu for a duration of 0.225 seconds	Frequency/Watt Control, model should trip entirely

A.4.5 Test 1.1a Plots

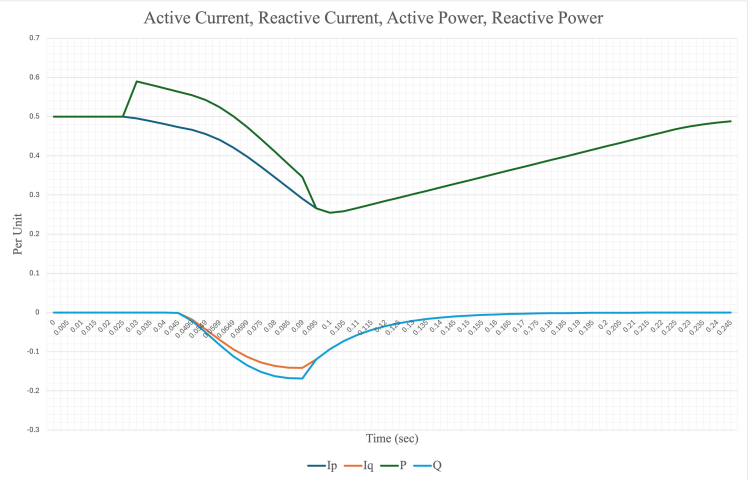


Figure A.10: Active and Reactive Currents, along with Active and Reactive Power outputs from the DER_A model during an over-voltage scenario

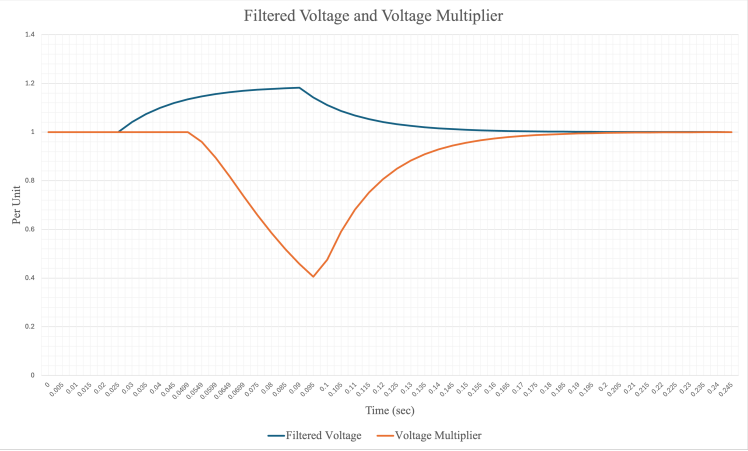


Figure A.11: Filtered (measured) voltage and the voltage multiplier (fraction of unit tripped) of the DER_A model during an over-voltage scenario

A.4.6 Test 1.1b Plots

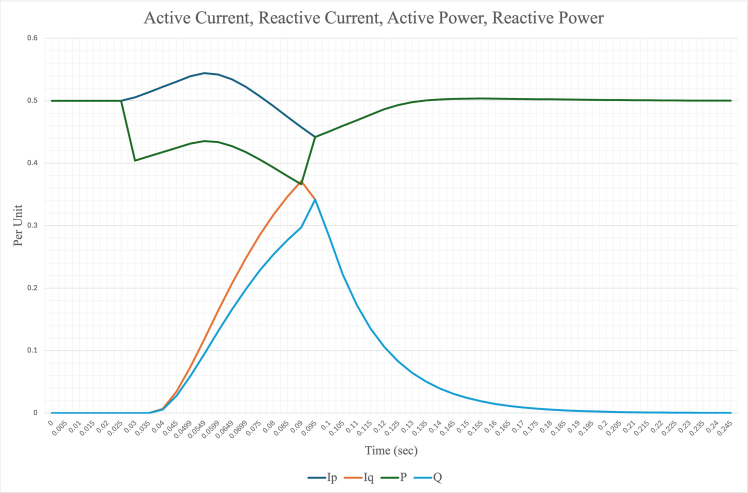


Figure A.12: Active and Reactive Currents, along with Active and Reactive Power outputs from the DER_A model during an under-voltage scenario

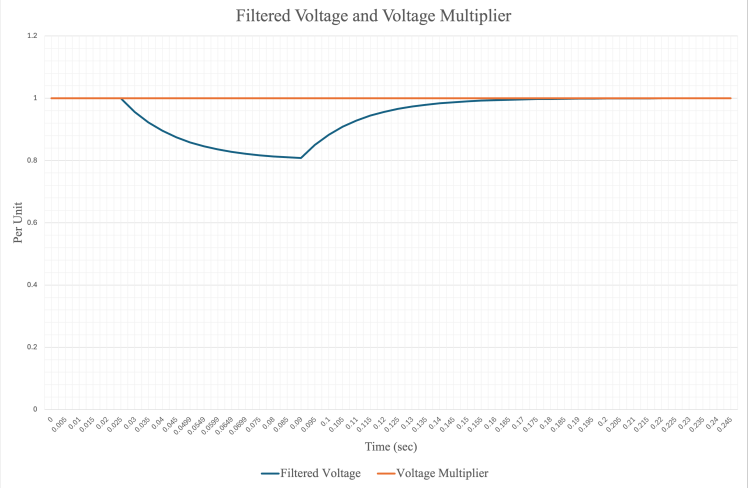


Figure A.13: Filtered (measured) voltage and the voltage multiplier (fraction of unit tripped) of the DER_A model during an under-voltage scenario

A.4.7 Test 1.2a Plots

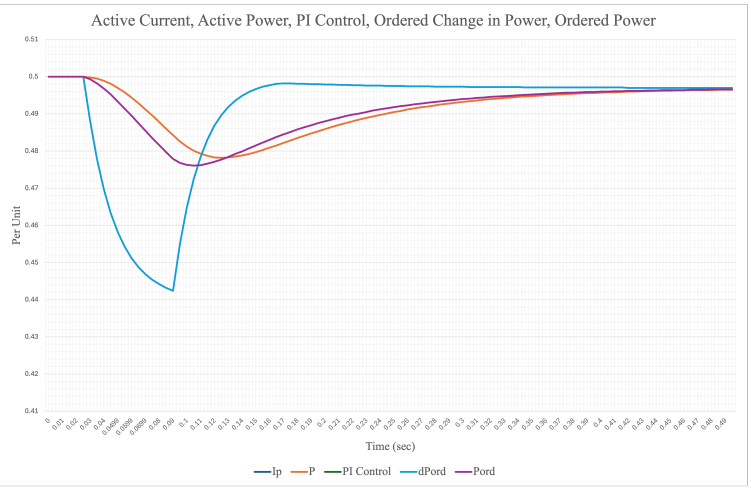


Figure A.14: DER_A model states of Active Current and Power, PI Control, Ordered Change in Power, and Ordered Power during an over-frequency scenario

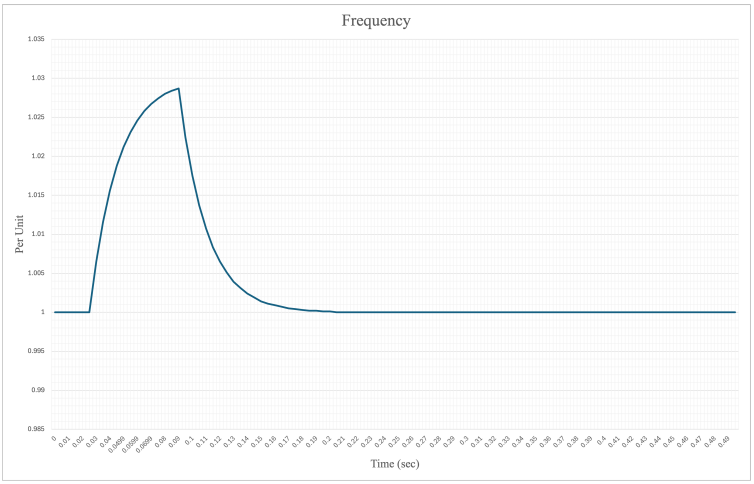


Figure A.15: DER_A model terminal frequency during an over-frequency scenario

A.4.8 Test 1.2b Plots

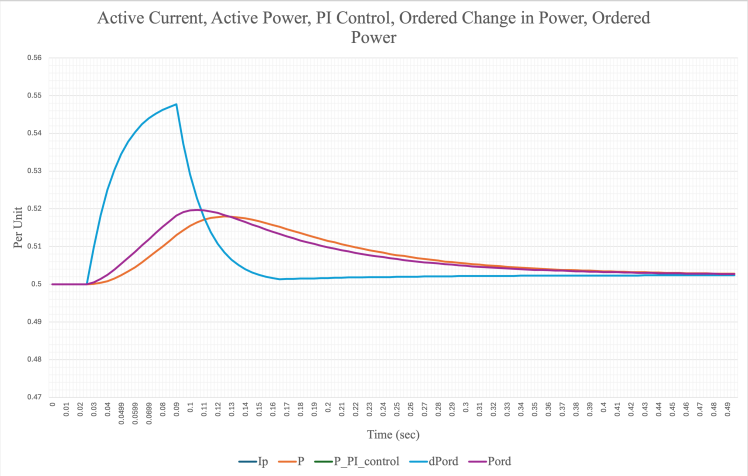


Figure A.16: DER_A model states of Active Current and Power, PI Control, Ordered Change in Power, and Ordered Power during an under-frequency scenario

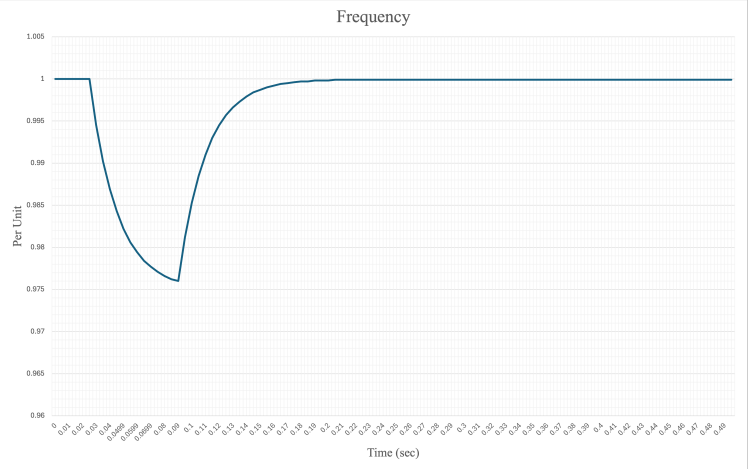


Figure A.17: DER_A model terminal frequency during an under-frequency scenario

A.4.9 Test 2.1a Plots

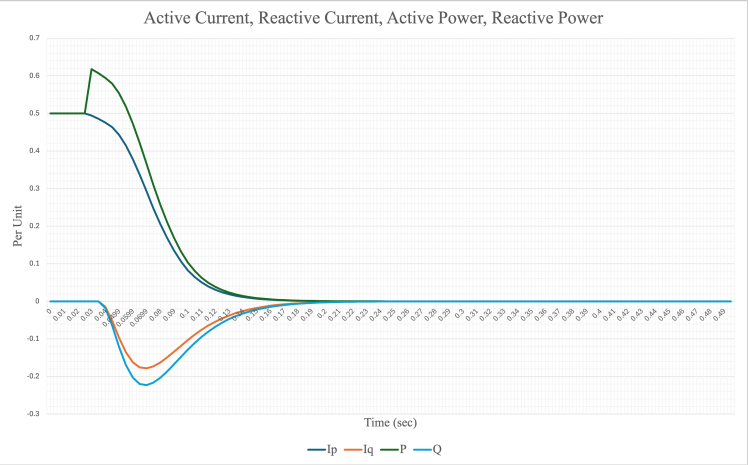


Figure A.18: Active and Reactive Currents, along with Active and Reactive Power outputs from the DER_A model during an over-voltage scenario which trips the model

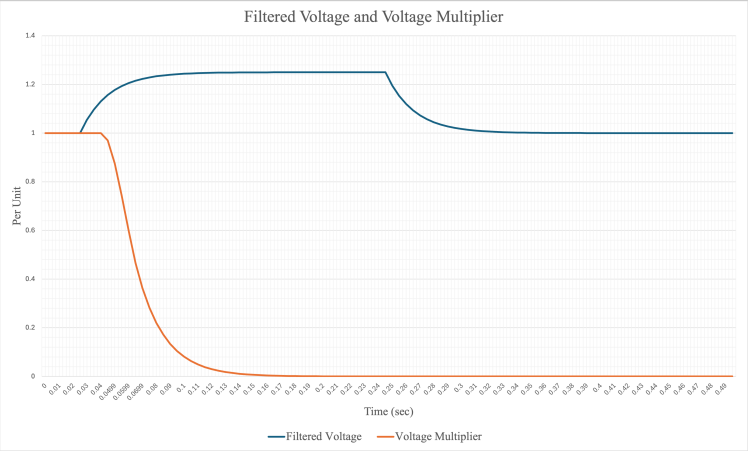


Figure A.19: Filtered (measured) voltage and the voltage multiplier (fraction of unit tripped) of the DER_A model during an over-voltage scenario which trips the model

A.4.10 Test 2.1b Plots

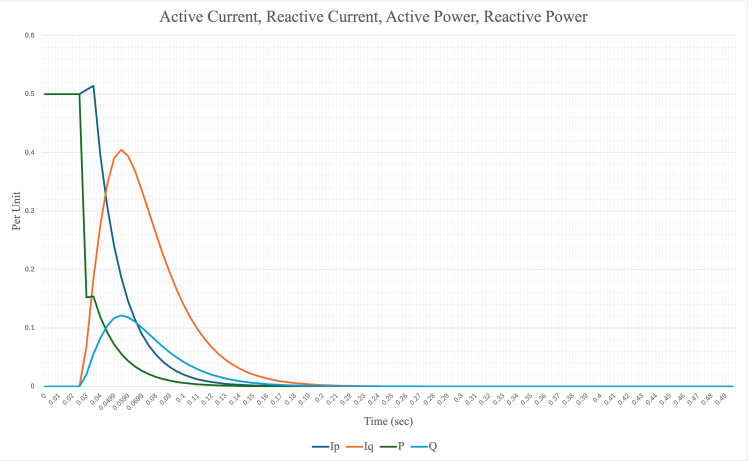


Figure A.20: Active and Reactive Currents, along with Active and Reactive Power outputs from the DER_A model during an under-voltage scenario which trips the model

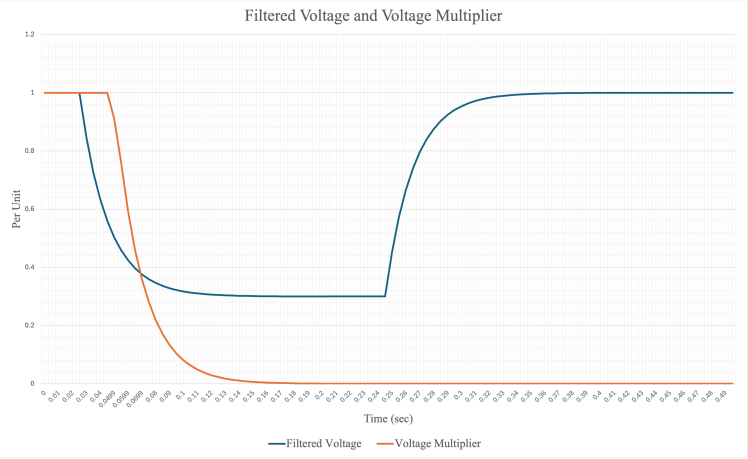


Figure A.21: Filtered (measured) voltage and the voltage multiplier (fraction of unit tripped) of the DER_A model during an under-voltage scenario which trips the model

A.4.11 Test 2.2a Plots

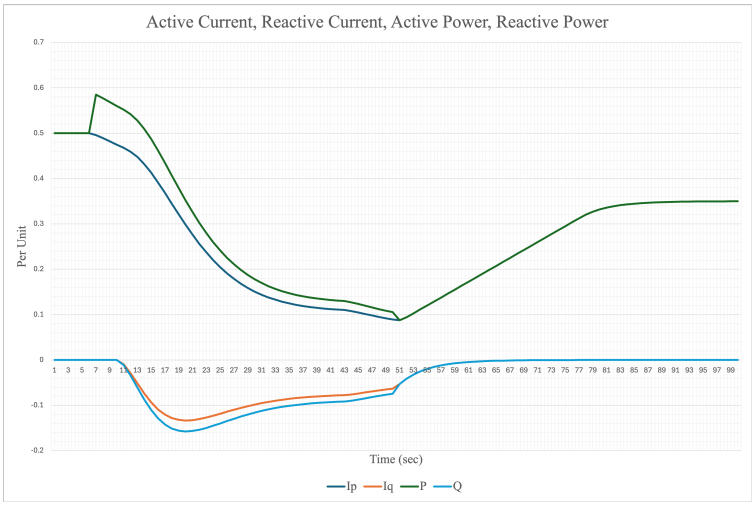


Figure A.22: Active and Reactive Currents, along with Active and Reactive Power outputs from the DER_A model during an over-voltage scenario which partially trips the model

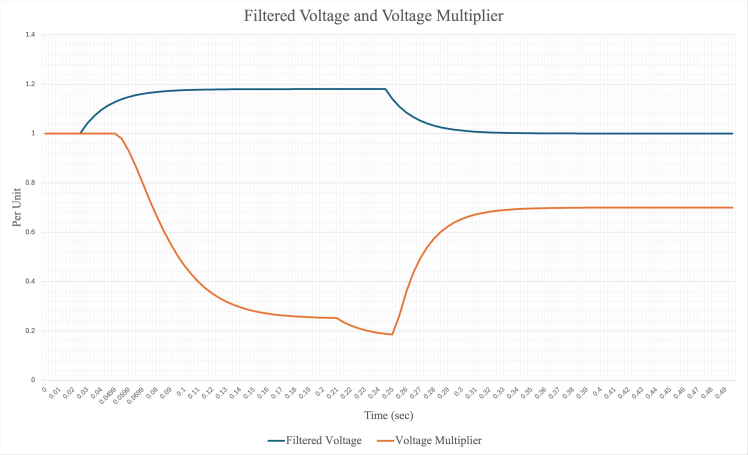


Figure A.23: Filtered (measured) voltage and the voltage multiplier (fraction of unit tripped) of the DER_A model during an over-voltage scenario which partially trips the model

A.4.12 Test 2.2b Plots

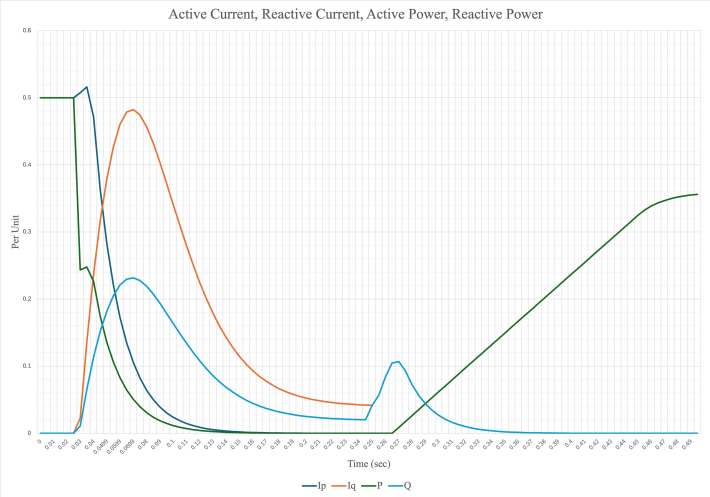


Figure A.24: Active and Reactive Currents, along with Active and Reactive Power outputs from the DER_A model during an under-voltage scenario which partially trips the model

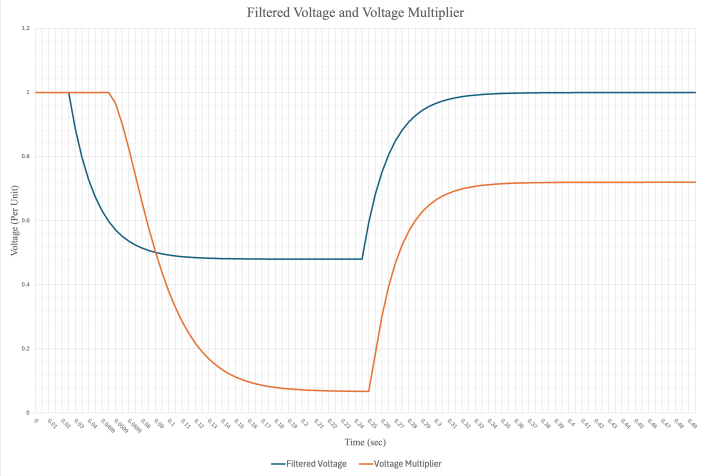


Figure A.25: Filtered (measured) voltage and the voltage multiplier (fraction of unit tripped) of the DER_A model during an under-voltage scenario which partially trips the model

A.4.13 Test 2.3a Plots

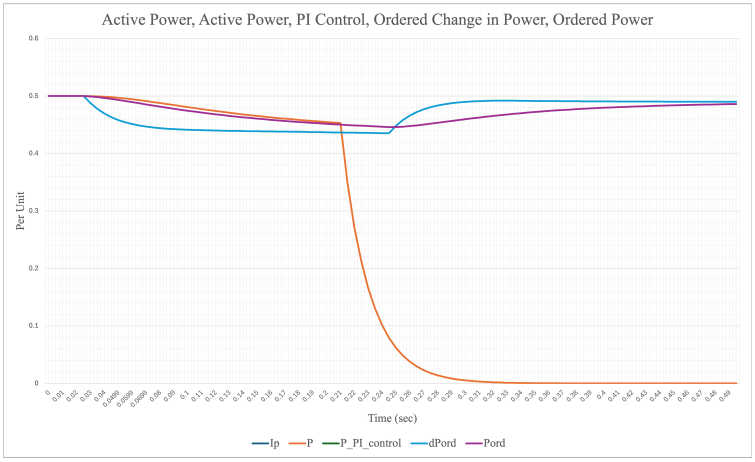


Figure A.26: DER_A model states of Active Current and Power, PI Control, Ordered Change in Power, and Ordered Power during an over-frequency scenario which trips the model

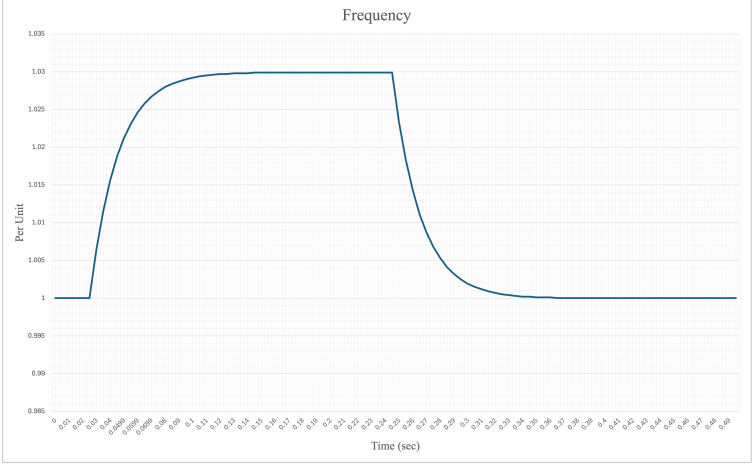


Figure A.27: DER_A model terminal frequency during an over-frequency scenario which trips the model

A.4.14 Test 2.3b Plots

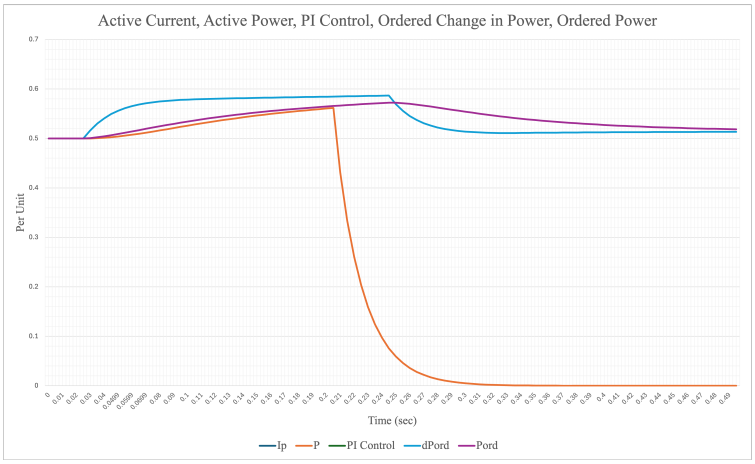


Figure A.28: DER_A model states of Active Current and Power, PI Control, Ordered Change in Power, and Ordered Power during an under-frequency scenario which trips the model

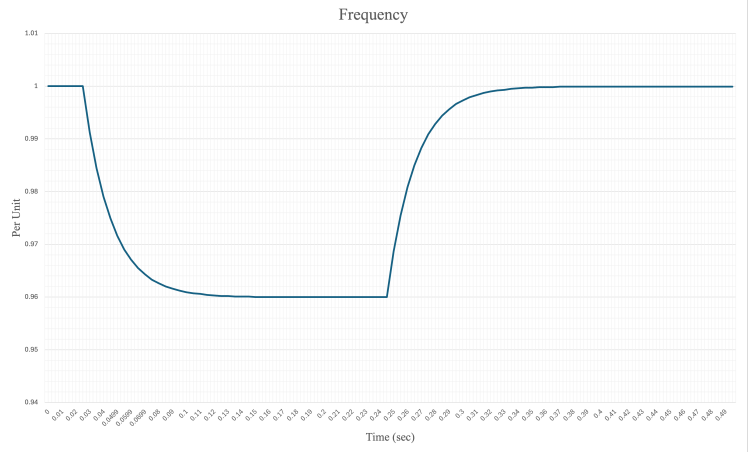


Figure A.29: DER_A model terminal frequency during an under-frequency scenario which trips the model

A.4.15 Test 1.1a Discussion

Seen in A.10 and A.11, the filtered (measured) voltage rises to a maximum value of roughly 1.18 pu, decreasing the voltage multiplier down to 0.4. This should expected, as Vh1 is set to 1.12 pu and Vh0 is set to 1.2 pu, meaning there is a linear tripping pattern from 1.12 pu (whole device is online) and 1.2 pu (whole device is tripped). At 1.18 pu, it would then be expected the voltage multiplier to fall to roughly 0.25. While it does not fall this low, results are consistent with expectations as the voltage multiplier filters its output, so it has not reach steady state yet prior to the measured voltage recovering.

A.4.16 Test 1.1b Discussion

Seen in A.12 and A.13, the filtered (measured) voltage falls to a minimum value of roughly 0.8 pu, which does not decrease the voltage multiplier from 1. This should expected, as Vl1 is set to 0.62 pu and Vl0 is set to 0.47 pu, meaning there is no device tripping if voltage remains above 0.62 pu. Additionally, the reactive current injection and reactive power injection of A.12 show the unique Volt/VAR characteristics, as reactive power spikes to 0.35 during the voltage sag.

A.4.17 Test 1.2a Discussion

Seen in A.14 and A.15, the measured frequency reaches a maximum value of roughly 1.0275 pu (60 Hertz is nominal). This triggers a decrease in active power output, however it does not stay above $fhtrp$ for longer than thl, which are set to 1.02 pu and 0.16 seconds, respectively. Therefore, it returns to steady state following the frequency return to 1 pu.

A.4.18 Test 1.2b Discussion

Similarly as Test 1.2a, A.16 and A.17 show the measured frequency reaches a minimum value of roughly 0.976 pu (60 Hertz is nominal). This triggers a increase in active power output, however it does not stay below $fltrp$ for longer than tfl, which are set to 0.975 pu and 0.16 seconds, respectively. Therefore, it returns to steady state following the frequency return to 1 pu.

A.4.19 Test 2.1a Discussion

Seen in A.18 and A.19, the filtered (measured) voltage rises above $Vh0$ (set to 1.2 pu) for longer than $tvh0$ (set to 0.16 seconds), so the model remains tripped upon voltage recovery. It can also be seen that the model absorbs reactive power prior to tripping, which is expected in an under-voltage scenario.

A.4.20 Test 2.1b Discussion

Similarly as Test 2.1a, A.20 and A.21 show the filtered (measured) voltage falls below $Vl0$ (set to 0.47 pu) for longer than $tvl0$ (set to 0.16 seconds), so the model remains tripped upon voltage recovery. It can also be seen that the model injects reactive power prior to tripping, which is expected in an under-voltage scenario.

A.4.21 Test 2.2a Discussion

Seen in A.22 and A.23, the filtered (measured) voltage rises above $Vh1$ (set to 1.12 pu) for longer than $tvh1$ (set to 0.16 seconds). However, it also stays above $Vh0$ during this timeframe. Therefore, upon voltage recovery, it can be seen that only roughly 70% of the model reconnects (30% of the model is fully tripped). This behavior is shown in A.9, and is consistent with expectations as $Vrfrac$ is set to 0.7. Once again, the model absorbs reactive power during the over-voltage period, which is anticipated

A.4.22 Test 2.2b Discussion

Similarly as Test 2.2a, A.24 and A.25, the filtered (measured) voltage falls below $Vl1$ (set to 0.62 pu) for longer than $tvh1$ (set to 0.16 seconds). However, it also stays above $Vl0$ during this timeframe (set to 0.47 pu). Therefore, upon voltage recovery, it can be seen that only roughly 70% of the model reconnects (30% of the model is fully tripped). This behavior is shown in A.9, and is consistent with expectations as $Vrfrac$ is set to 0.7. Additionally, it can be seen that the model injects reactive power during the under-voltage period, which should be expected from the Volt/VAR Control. Lastly, seen in A.24, the ramping up of Ip is linear. This is due to the ramp rate parameter, $rrpwr$, found in A.8.

A.4.23 Test 2.3a Discussion

Seen in A.26 and A.27, the measured frequency rises above $fhtrp$ (set to 1.02 pu) for longer than tfh (set to 0.16 seconds), so the model remains tripped upon frequency recovery. It can also be seen that the model reduces it's active power output prior to tripping, due to the Freq/Watt controls.

A.4.24 Test 2.3b Discussion

Similarly as Test 2.3a, A.28 and A.29, the measured frequency falls below $fltrp$ (set to 0.975 pu) for longer than tfl (set to 0.16 seconds), so the model remains tripped upon frequency recovery. It can also be seen that the model increases it's active power output prior to tripping, due to the Freq/Watt controls.

B. DER_A Functions and Code Implementation

B.1 Deadband Code Implementation

```
private double deadband(double inputVal, double deadband_low, double
    deadband_high) {
     double outputVal = 0;
     if (inputVal < deadband_low) {
         outputVal = inputVal - deadband_low;
     } else if (inputVal > deadband_high) {
         outputVal = inputVal - deadband_high;
     }
     return outputVal;
 }
```

B.2 Volt/VAR Control Code Implementation

```
// compute the filtered voltage
if (flag == 0) { // predictor
    this.dv_dt = (this.v_term - this.v_meas) / this.Trv;
    this.v_meas = this.v_meas + this.dv_dt * this.dt;
} else { // corrector
    double d_dt_2 = (this.v_term - this.v_meas) / this.Trv;
    this.v_meas = this.v_meas + (0.5 * (d_dt_2 - this.dv_dt)) * this.dt;
}

// compute Iqv from difference between reference and measured
double Iqv = deadband((this.Vref - this.v_meas), this.dbd1, this.dbd2) *
    this.Kqv;

// bound Iqv by Iqh1 and Iqh2
if (Iqv > this.Iqh1) {
    Iqv = this.Iqh1;
} else if (Iqv < this.Iql1) {
    Iqv = this.Iql1;
}
```

B.3 Droop Control Code Implementation

```
// compute the filtered frequency
if (flag == 0) { // predictor
    this.df_dt = (this.f_term - this.f_meas) / this.Trf;
    this.f_meas = this.f_meas + this.df_dt * this.dt;
} else { // corrector
    double d_dt_2 = (this.f_term - this.f_meas) / this.Trf;
```

```
    this.f_meas = this.f_meas + (0.5 * (d_dt_2 - this.df_dt)) * this.dt;
}

// compute droop based on the filtered frequency
double f_err = deadband((this.f_ref - this.f_meas), this.fdbd1, this.fdbd2);
double f_droop = (f_err * this.Ddn) + (f_err * this.Dup);
if ((f_err * this.Ddn) > 0) {
    f_droop = f_err * this.Dup;
} else if ((f_err * this.Dup) < 0) {
    f_droop = f_err * this.Ddn;
}
```

B.4 Active Current Control Code Implementation

```
// compute the filtered ordered power
if (flag == 0) { // predictor
    this.dp_dt = (this.Pord - this.p_meas ) / this.Tp;
    this.p_meas = this.p_meas + this.dp_dt * this.dt;
} else { // corrector
    double d_dt_2 = (this.Pord - this.p_meas) / this.Tp;
    this.p_meas = this.p_meas + (0.5 * (d_dt_2 - this.dp_dt)) * this.dt;
}

// compute error signal including droop
this.f_error = droop - this.p_meas + this.Pref;
if (this.f_error > this.femax) {
    this.f_error = this.femax;
} else if (this.f_error < this.femin) {
    this.f_error = this.femin;
}

// feedback loop calculation
if (flag == 0) { // predictor
     this.dPI_dt = (this.power_PI - this.power_integral) / (this.Kpg / this.Kig);
     this.power_integral = this.power_integral + this.dPI_dt * this.dt;
 } else if (flag == 1) { // corector
     double d_dt_2 = (this.power_PI - this.power_integral) / (this.Kpg /
         this.Kig);
     this.power_integral = this.power_integral + (0.5 * (d_dt_2 - this.dPI_dt)) *
         this.dt;
 }
 // feedforward calculation based off feedback
 this.power_PI = (this.f_error * this.Kpg) + this.power_integral;
 if (this.power_PI > this.Pmax) {
     this.power_PI = this.Pmax;
 } else if (this.power_PI < this.Pmin) {
```

```
    this.power_PI = this.Pmin;
}

// Bound between Pmin and Pmax
this.power_PI = (this.f_error * this.Kpg) + this.power_integral;
if (this.power_PI > this.Pmax) {
    this.power_PI = this.Pmax;
} else if (this.power_PI < this.Pmin) {
    this.power_PI = this.Pmin;
}

// implement the rate limiter based on the FreqFlag
double inp = 0;
if (this.FreqFlag == 0) {
    inp = this.Pref;
} else {
    inp = this.power_PI;
}
this.dPord = rate_limiter(inp, this.dPord, this.dPmax, this.dPmin, this.dt);

// find the filtered value of ordered power
if (flag == 0) { // predictor
    this.dPord_dt = (this.dPord - this.Pord) / this.TPord;
    this.Pord = this.Pord + this.dPord_dt * this.dt;
} else { // corrector
    double d_dt_2 = (this.dPord - this.Pord) / this.TPord;
    this.Pord = this.Pord + (0.5 * (d_dt_2 - this.dPord_dt)) * this.dt;
}

// Bound between Pmin and Pmax
if (this.Pord > this.Pmax) {
    this.Pord = this.Pmax;
} else if (this.Pord < this.Pmin) {
    this.Pord = this.Pmin;
}

// compute Ip command based off ordered power and filtered voltage
this.Ipcmd = this.Pord / this.v_meas;
if (this.Ipcmd > this.Ipmax) {
    this.Ipcmd = this.Ipmax;
} else if (this.Ipcmd < this.Ipmin) {
    this.Ipcmd = this.Ipmin;
}
```

B.5 Reactive Current Control Implementation

```
// compute active power inject from either PF or reference Q
double q_PF = Math.tan(this.thetaPF) * this.p_meas;
if (PfFlag == 0) {
    q_PF = this.Qref;
}
this.QVInput = q_PF / this.v_meas;

if (flag == 0) { // predictor
    this.dvv_dt = (this.QVInput - this.reactCurrRef) / this.Tiq;
    this.reactCurrRef = this.reactCurrRef + this.dvv_dt * this.dt;
} else { // corrector
    double d_dt_2 = (this.QVInput - this.reactCurrRef) / this.Tiq);
    this.reactCurrRef = this.reactCurrRef + (0.5 * (d_dt_2 - this.dvv_dt)) *
        this.dt;
}

// compute Iq command with signal from volt/var control
this.Iqcmd = Iqv + this.reactCurrRef;
// bound from Iqmin to Iqmax
if (this.Iqcmd > this.Iqmax) {
    this.Iqcmd = this.Iqmax;
} else if (this.Iqcmd < this.Iqmin) {
    this.Iqcmd = this.Iqmin;
}
```

B.6 Voltage Source Calculation

```
// adjust Ip and Iq based on freq. and volt. tripping
double IpcmdAdj = this.Ipcmd * (this.vMult * this.f_relay);
double IqcmdAdj = this.Iqcmd * (this.vMult * this.f_relay);

// compute Ip and Iq from Ipcmd and Iqcmd
if (flag == 0) { // predictor
    this.dip_dt = (IpcmdAdj - this.Ip) / this.tg;
    this.Ip = this.Ip + this.dip_dt * this.dt;

    this.diq_dt = (IqcmdAdj - this.Iq) / this.tg;
    this.Iq = this.Iq + this.diq_dt * this.dt;
} else { // corrector
    double dIp_dt_2 = (IpcmdAdj - this.Ip) / this.tg;
    this.Ip = this.Ip + (0.5 * (dIp_dt_2 - this.dip_dt)) * this.dt;

    double dIq_dt_2 = (IqcmdAdj - this.Iq) / this.tg;
    this.Iq = this.Iq + (0.5 * (dIq_dt_2 - this.diq_dt)) * this.dt;
}
```

```
// apply ramp rates to Ip, and set the updated value of Ip and Iq
this.Ip = rate_limiter(this.Ip, Ip_prev, this.Rup, this.Rdown, this.dt);

// calculate system internal voltage in dq axis
double Eq = getPosSeqVt().getImaginary() - (this.Ip * this.Xe);
double Ed = getPosSeqVt().getReal() - (this.Iq * this.Xe);

// get voltage angle of parent bus
double vtAng = this.getDStabBus().getVoltageAng();

// transform to system axis (Park to Clarke transform)
double Er = Ed*Math.cos(vtAng) - Eq*Math.sin(vtAng);
double Ex = Ed*Math.sin(vtAng) + Eq*Math.cos(vtAng);

// set the internal voltage attribute
setInternalVoltage(new Complex(Er, Ex));
```

B.7 Fractional Voltage Tripping Code Implementation

```
private void voltageTripLogic() {
    double vlMult = 1;
    double vhMult = 1;


    if (this.v_meas >= this.Vl1) {
        this.activeTimerVl1 = false;
    } else if (!activeTimerVl1) {
        this.activeTimerVl1 = true;
        this.timeBelowVl1 = getCurrSimuTime();
    }

    if (this.v_meas >= this.Vl0) {
        this.activeTimerVl0 = false;
    } else if (!activeTimerVl0) {
        this.activeTimerVl0 = true;
        this.timeBelowVl0 = getCurrSimuTime();
    }

    if (this.v_meas <= this.Vh1) {
        this.activeTimerVh1 = false;
    } else if (!activeTimerVh1) {
        this.activeTimerVh1 = true;
        this.timeAboveVh1 = getCurrSimuTime();
    }

    if (this.v_meas <= this.Vh0) {
```

```
    this.activeTimerVh0 = false;
} else if (!activeTimerVh0) {
    this.activeTimerVh0 = true;
    this.timeAboveVh0 = getCurrSimuTime();
}

if (!this.activeFracLow && this.activeTimerVl1 && ((getCurrSimuTime() -
    this.timeBelowVl1) >= this.Tvl1)) {
    this.activeFracLow = true;
}
if (!this.activeFracHigh && this.activeTimerVh1 && ((getCurrSimuTime() -
    this.timeAboveVh1) >= this.Tvh1)) {
    this.activeFracHigh = true;
}

if (!this.activeTripLow && this.activeTimerVl0 && ((getCurrSimuTime() -
    this.timeBelowVl0) >= this.Tvl0)) {
    this.activeTripLow = true;
}
if (!this.activeTripHigh && this.activeTimerVh0 && ((getCurrSimuTime() -
    this.timeAboveVh0) >= this.Tvh0)) {
    this.activeTripHigh = true;
}

if ((this.Vmin > this.v_meas) && this.activeFracLow) {
    this.Vmin = this.v_meas;
    if (this.Vmin < this.Vl0) {
        this.Vmin = this.Vl0;
    }
}
if ((this.Vmax < this.v_meas) && this.activeFracHigh) {
    this.Vmax = this.v_meas;
    if (this.Vmax < this.Vh0) {
        this.Vmax = this.Vh0;
    }
}

if ((this.v_meas <= this.Vl0) || this.activeTripLow) {
    vlMult = 0;
} else if ((this.v_meas <= this.Vl1) && (this.v_meas > this.Vmin) &&
    (this.activeFracLow)) {
    vlMult = ((this.Vmin - this.Vl0) + this.Vrfrac * (this.v_meas -
        this.Vmin))/ (this.Vl1 - this.Vl0);
} else if (this.v_meas <= this.Vl1) {
    vlMult = (this.v_meas - this.Vl0) / (this.Vl1 - this.Vl0);
} else if (!this.activeFracLow) {
    vlMult = 1;
```

```
    } else {
        vlMult = ((this.Vmin - this.Vl0) + this.Vrfrac * (this.Vl1 - this.Vmin))
            / (this.Vl1 - this.Vl0);
    }

    if ((this.v_meas >= this.Vh0) || this.activeTripHigh) {
        vhMult = 0;
    } else if ((this.v_meas >= this.Vh1) && (this.v_meas < this.Vmax) &&
        (this.activeFracHigh)) {
        vhMult = ((this.Vmax - this.Vh0) + this.Vrfrac * (this.v_meas -
            this.Vmax))/ (this.Vh1 - this.Vh0);
    } else if (this.v_meas >= this.Vh1) {
        vhMult = (this.v_meas - this.Vh0) / (this.Vh1 - this.Vh0);
    } else if (!this.activeFracHigh) {
        vhMult = 1;
    } else {
        vhMult = ((this.Vmax - this.Vh0) + this.Vrfrac * (this.Vh1 - this.Vmax))
            / (this.Vh1 - this.Vh0);
    }

    double updVMult = vhMult * vlMult;
    if (this.VtripFlag == 1) {
        this.vMult = firstOrderTF(updVMult, this.vMult, this.Tv, this.dt);
    } else {
        this.vMult = firstOrderTF(1, this.vMult, this.Tv, this.dt);
    }
}
```

B.8 Frequency Tripping Code Implementation

```
private void freqTripLogic() {
    if (this.FtripFlag == 0) { // turn off frequency relay
        this.f_relay = 1;
    } else {
        if (this.f_relay == 0) { // if already tripped, stay tripped
            return;
        }

        double f_meas_Hz = 1 * 60;
        if (this.getParentGen().getParentBus().getVoltageMag() > this.Vpr) {
            f_meas_Hz = this.f_meas * 60;
        }

        if (f_meas_Hz >= this.fhtrp){
            if (!this.activeTimerFhtrp) {
                this.timeAboveFhtrp = getCurrSimuTime();
```

```
            }
            this.activeTimerFhtrp = true;
        } else {
            this.activeTimerFhtrp = false;
            this.timeAboveFhtrp = 0;
        }

        if (f_meas_Hz <= this.fltrp){
            if (!this.activeTimerFltrp) {
                this.timeBelowFltrp = getCurrSimuTime();
            }
            this.activeTimerFltrp = true;
        } else {
            this.activeTimerFltrp = false;
            this.timeBelowFltrp = 0;
        }

        if (this.activeTimerFhtrp && ((getCurrSimuTime() - this.timeAboveFhtrp) >
            this.tfh)) {
            this.f_relay = 0; // trip model
        } else if (this.activeTimerFltrp && ((getCurrSimuTime() -
            this.timeBelowFltrp) > this.tfl)) {
            this.f_relay = 0; // trip model
        } else {
            this.f_relay = 1;
        }
    }
}
```

B.9 Active and Reactive Power Priority Code Implementation

```
private void updateIdIqMax() {
    if (this.PQFlag == 0) {
        this.Iqmax = this.Imax;
        this.Ipmax = Math.sqrt((this.Imax*this.Imax) - (this.Iqcmd*this.Iqcmd));
    } else {
        this.Ipmax = this.Imax;
        this.Iqmax = Math.sqrt((this.Imax*this.Imax) - (this.Ipcmd*this.Ipcmd));
    }
}
```

B.10 Ramp Rate Updating Code Implementation

```
// the ramp rate is only applied in the current direction of Ip
private void update_rrpwr(double Ip) {
```

```
    if (Ip >= 0) {
        this.Rup = this.rrpwr;
    } else {
        this.Rup = 10e9;
    }
    if (Ip <= 0) {
        this.Rdown = -1*this.rrpwr;
    } else {
        this.Rdown = -10e9;
    }
}
```

C. Final Proposed Method Test System Model Parameterization

C.1 Single-Phase Induction Motor Parameterization

C.2 DER_A Model Parameterization

Note that the many of the parameters below were used in reference to [53]. Some values have been adjusted slightly for the sake of example, although critical ones follow this guideline.

Table C.1: Single-Phase AC Induction Motor Parameters

Parameter	**Setting**	**Notes**
Vstall	0.55	Voltage at which stalling may occur
Rstall	0.1	Resistance during stalled state
Xstall	0.1	Reactance during stalled state
Tstall	0.033	If the voltage falls below $Vstall$ for longer than $Tstall$, device jumps to a stalled state
Frst	0.2	Fraction of device that leaves stalled state upon voltage recovery
Vrst	0.95	Voltage at which device can leave stalled state
Fuvr	0.1	Fraction of device using undervoltage relays
UVtr1	0.6	First under-voltage pickup level
Ttr1	0.02	Timer for first under-voltage pickup level
UVtr2	1	Second under-voltage pickup level
Ttr2	9999	Timer for second under-voltage pickup level
Vc1off	0.5	Voltage at which load fraction begins decreasing
Vc2off	0.4	Voltage at which load fraction goes to 0
Vc1on	0.6	Voltage at which load fraction begins increasing
Vc2on	0.5	Voltage at which load fraction goes to 1
Tth	15	Compressor heating time constant
Th1t	0.7	Compressor motors begin tripping
Th2t	1.9	Compressor motors end tripping

Table C.2: DER_A Model Parameters

Parameter	Setting	Notes	Parameter	Setting	Notes
Trv	0.02	Voltage measurement time constant	fltrp	58.5	Lower frequency tripping threshold
Trf	0.02	Frequency measurement time constant	fhtrp	61.2	Upper frequency tripping threshold
Tp	0.02	Ordered active power measurement time constant	tfl	0.16	Tripping timer for under-frequency
Tiq	0.02	Q control time constant	tfh	0.16	Tripping timer for over-frequency
Tpord	5	Power order time constant	tg	0.02	Current control time constant
Tv	0.02	Fractional voltage tripping time constant	rrpwr	2.0	Power rise ramp rate maximum
dbd1	-0.12	Lower deadband for voltage control	Xe	0.25	Internal Machine Impedance
dbd2	0.05	Upper deadband for voltage control	Vpr	0.3	Voltage where frequency tripping is diabled
fdbd1	-0.0006	Lower deadband for frequency control	Iqh1	1.0	Maximum reactive current injection, pu
fdbd2	0.0006	Upper deadband for frequency control	Iql1	-1.0	Minimum reactive current injection, pu
Kqv	5	Proportional voltage control gain	Pmax	1.2	Maximum active power
Kpg	0.1	Proportional active power control gain	Pmin	0.0	Minimum active power
Kig	10.0	Integral active power control gain	PfFlag	1	0 is constant Q injection, 1 is PF control

Table C.3: DER_A Model Parameters Cont.

Parameter	Setting	Notes	Parameter	Setting	Notes
Ddn	20	Down droop constant	FreqFlag	1	0 disables frequency control, 1 enables it
Dup	20	Up Droop Constant	PQFlag	0	0 is Q priority, 1 is P priority
femax	99	Upper bound for frequency error	TypeFlag	1	0 means model acts as a storage device, 1 is generator
femin	-99	Lower bound for frequency error	VTripFlag	1	0 disables voltage tripping, 1 enables it
dPmax	99	Power increase ramp rate	FTripFlag	1	0 disables frequency tripping, 1 enables it
dPmin	-99	Power decrease ramp rate	Tvl0	0.16	Tripping timer under $Vl0$
Imax	1.2	Maximum current	Tvl1	0.16	Tripping timer under $Vl1$
Vl0	0.45	Highest under-voltage where $Vmult$= 0	Tvh0	0.16	Tripping timer above $Vh0$
Vl1	0.6	Lowest under-voltage where $Vmult$= 1	Tvh1	0.16	Tripping timer above $Vh1$
Vh0	1.2	Lowest over-voltage where $Vmult = 0$	Vrfrac	0.5	Fraction of device that recovers after $Tvh1$ or $Tvl1$ expires
Vh1	1.12	Lowest over-voltage where $Vmult = 0$			

D. Select Test System Diagrams and Contingency Analysis Results

D.1 IEEE 300 Bus Test System Dynamic Load Locations

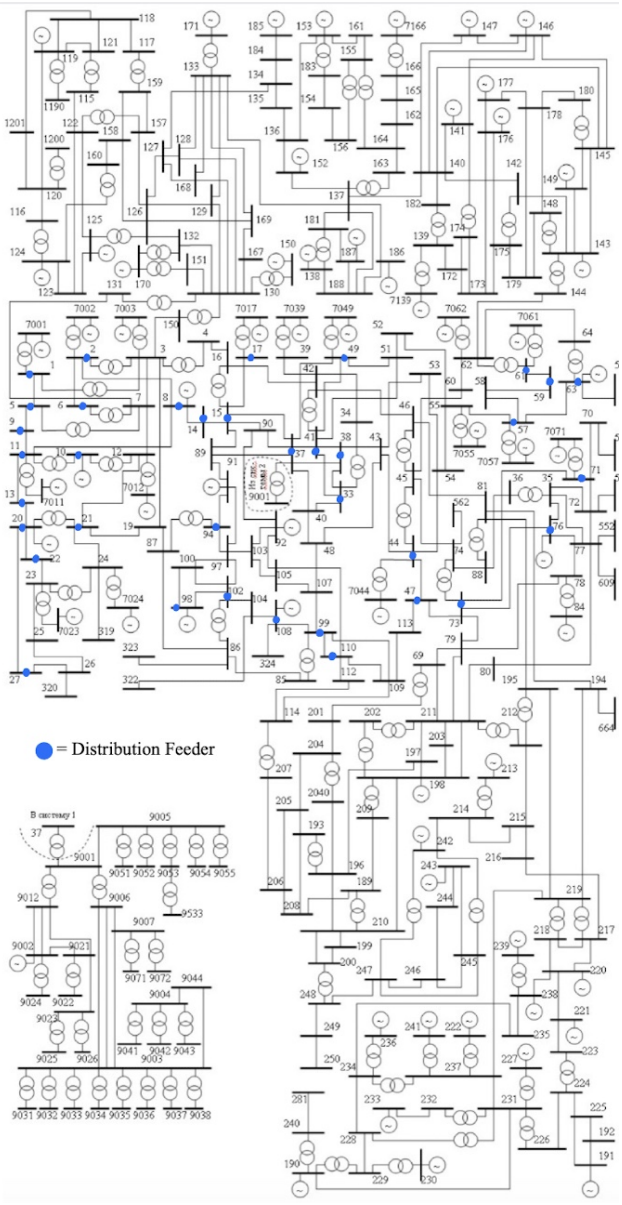


Figure D.1: The IEEE 300 Bus System. Nine bus distribution feeder locations are marked with blue dots. Image adopted from [3]

D.2 IEEE 300 Bus Test System Impact Zone Diagram

Table D.1: Statistics due to a Three-Phase Fault at Bus 76

Simulation	Increase in Runtime	Avg. RMSE	Max. RMSE	Max. Voltage Difference (pu)
All Aggregated	Baseline	0.00637	0.1123	0.1808
Multi-Fidelity	70%	0.00103	0.0365	0.0366
All Disaggregated	1182%	Baseline	Baseline	Baseline

Table D.2: Statistics due to a Three-Phase Fault at Bus 122

Simulation	Increase in Runtime	Avg. RMSE	Max. RMSE	Max. Voltage Difference (pu)
All Aggregated	Baseline	0.0010	0.0364	0.0366
Multi-Fidelity	47.9%	0.0010	0.0364	0.0366
All Disaggregated	1443%	Baseline	Baseline	Baseline

D.3 Contingency Analysis Locations Across IEEE 300 Bus Test System Impact

D.4 Contingency Analysis Statistics for Other Fault Locations

Table D.3: Statistics due to a Three-Phase Fault at Bus 4

Simulation	Increase in Runtime	Avg. RMSE	Max. RMSE	Max. Voltage Difference (pu)
All Aggregated	Baseline	0.00149	0.0370	0.09121
Multi-Fidelity	523.5%	0.00044	0.00475	0.0317
All Disaggregated	1380%	Baseline	Baseline	Baseline

Table D.4: Statistics due to a Three-Phase Fault at Bus 182

Simulation	**Increase in Runtime**	**Avg. RMSE**	**Max. RMSE**	**Max. Voltage Difference (pu)**
All Aggregated	Baseline	0.00102	0.0364	0.03664
Multi-Fidelity	0%	0.00102	0.0364	0.03664
All Disaggregated	1362%	Baseline	Baseline	Baseline

Table D.5: Statistics due to a Three-Phase Fault at Bus 323

Simulation	**Increase in Runtime**	**Avg. RMSE**	**Max. RMSE**	**Max. Voltage Difference (pu)**
All Aggregated	Baseline	0.00105	0.0364	0.036
Multi-Fidelity	76.2%	0.00094	0.0364	0.036
All Disaggregated	1520%	Baseline	Baseline	Baseline

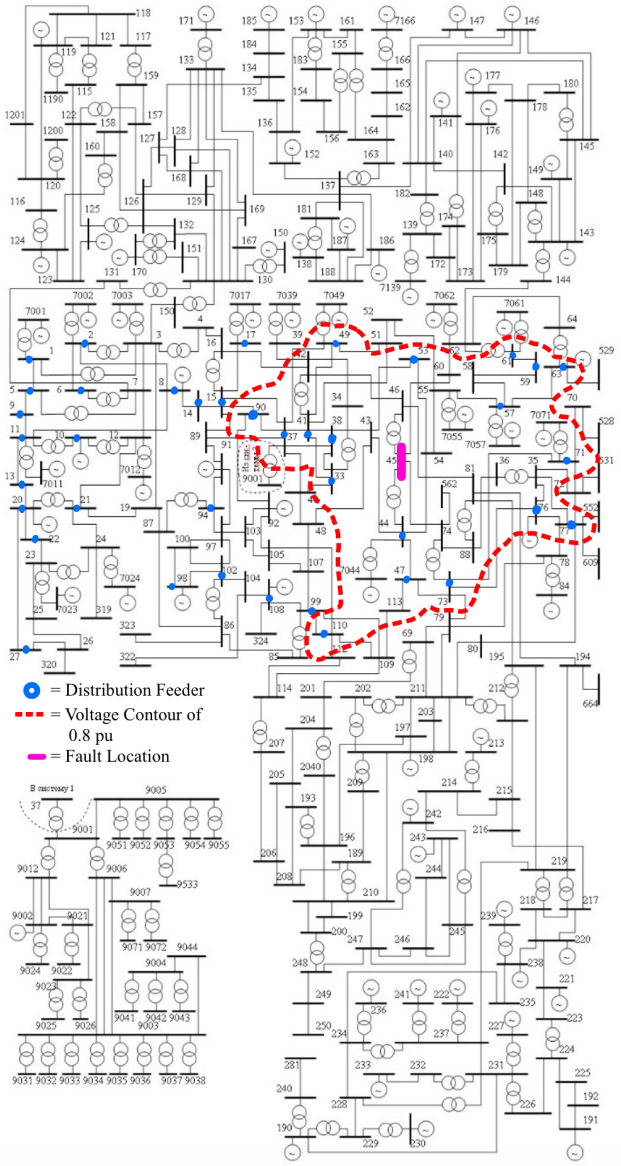


Figure D.2: High and low impact zone areas based on a fault located at Bus 45

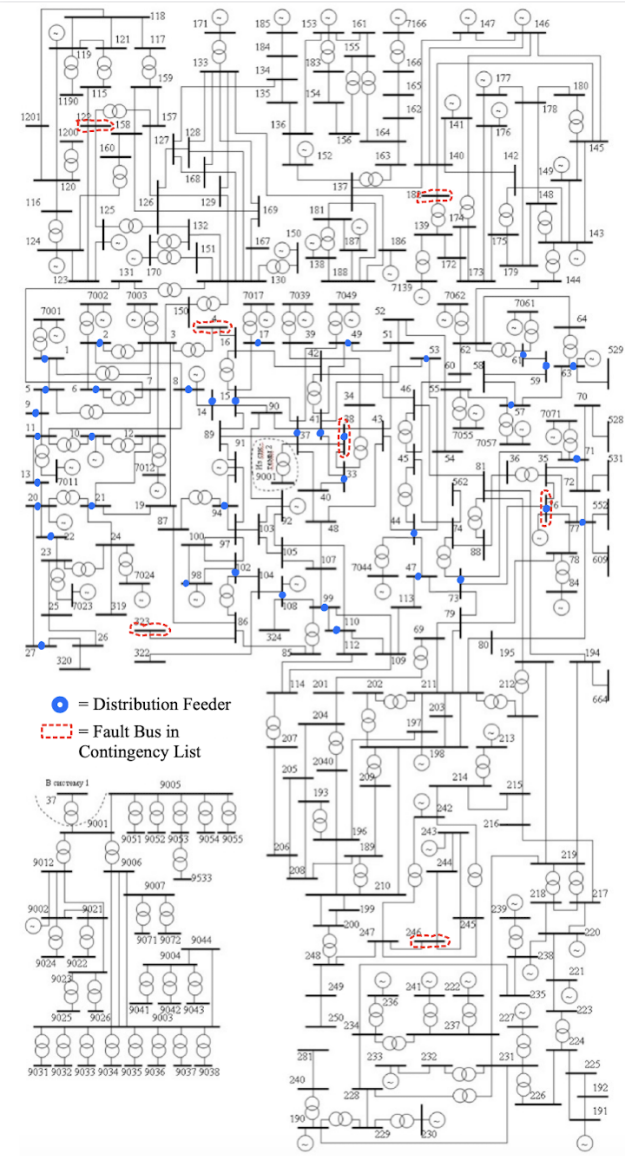


Figure D.3: The fault locations tested in the contingency analysis. All buses boxed in red are tested with a three-phase fault applied to each one

References

[1] B. Enayati, "Impact of IEEE 1547 standard on smart inverters and the applications in power systems."

[2] NERC, "Reliability guideline: Developing load model composition data," March 2017.

[3] A. R. Al-Roomi, "Power Flow Test Systems Repository," Halifax, Nova Scotia, Canada, 2015. [Online]. Available: https://al-roomi.org/power-flow

[4] B. Stott, "Power system dynamic response calculations," vol. 67, no. 2, pp. 219–241, conference Name: Proceedings of the IEEE. [Online]. Available: https://ieeexplore.ieee.org/document/1455502

[5] Q. Huang, R. Huang, R. Fan, J. Fuller, T. Hardy, Z. Huang, and V. Vittal, "A comparative study of interface techniques for transmission and distribution dynamic co-simulation," in *2018 IEEE Power & Energy Society General Meeting (PESGM)*, pp. 1–5, ISSN: 1944-9933. [Online]. Available: https://ieeexplore-ieee-org.mines.idm.oclc.org/abstract/document/8586046

[6] Q. Huang and V. Vittal, "Integrated transmission and distribution system power flow and dynamic simulation using mixed three-sequence/three-phase modeling," vol. 32, no. 5, pp. 3704–3714, conference Name: IEEE Transactions on Power Systems. [Online]. Available: https://ieeexplore.ieee.org/abstract/document/7782366

[7] M. Zhou and Q. Huang, "InterPSS: A new generation power system simulation engine." [Online]. Available: http://arxiv.org/abs/1711.10875

[8] A. Singhal, V. Ajjarapu, J. Fuller, and J. Hansen, "Real-time local volt/var control under external disturbances with high pv penetration," *IEEE Transactions on Smart Grid*, vol. 10, pp. 3849–3859, 7 2019.

[9] A. Singhal, A. K. Bharati, and V. Ajjarapu, "Deriving ders var-capability curve at tso-dso interface to provide grid services," *IEEE Transactions on Power Systems*, vol. 38, pp. 1818–1831, 3 2023.

[10] D. B. Arnold, M. Sankur, R. Dobbe, and K. Brady, *Optimal Dispatch of Reactive Power for Voltage Regulation and Balancing in Unbalanced Distribution Systems*. IEEE Power Energy Society General Meeting Conference 2016 in Boston, MA from July 17-21, 2016, 2016.

[11] A. Alkhonain, A. Singhal, A. K. Bharati, and V. Ajjarapu, "Sensitivity-aware reactive power dispatch of ders to support transmission grid during emergency," in *2023 North American Power Symposium (NAPS)*, 2023, pp. 1–6.

[12] North American Electric Reliability Corporation. (2021, September) May-June 2021 Odessa Disturbance.

[13] NERC Standard, "MOD-033-1, Steady state and dynamic system model validation."

[14] D. Ramasubramanian, I. Alvarez Fernandez, P. Mitra, A. Gaikwad, and J. Boemer, "The New Aggregated Distributed Energy Resources (der_a) Model for Transmission Planning Studies: 2019 Update," *Electric Power Research Institure (EPRI): Washington, DC, USA*, 2019.

[15] S. Nekkalapu, V. Vittal, J. Undrill, B. Keel, B. Gong, and K. Brown, "Synthesis of Load and Feeder Models Using Point on Wave Measurement Data," *IEEE Open Access Journal of Power and Energy*, vol. 8, pp. 198–210, 2021.

[16] S. Nekkalapu, V. Vittal, J. Undrill, B. Gong, and K. Brown, "Development of a Novel Positive Sequence Contactor Model Using Deep Neural Networks," *IEEE Transactions on Power Systems*, pp. 1–15, 2023.

[17] Federal Energy Regulatory Commission and others, "Distributed energy resources: Technical considerations for the bulk power system," Technical Report, 2018., Tech. Rep., 2022.

[18] NERC DER Task Force, "NERC Report on Distributed Energy Resources Task Force Report," 2017.

[19] D. Ramasubramanian, J. C. Boemer, P. Mitra, and A. Gaikwad, "Generic parameterization of the DER_A model."

[20] I. Alvarez Fernandez, D. Ramasubramanian, W. Sun, A. Gaikwad, J. C. Boemer, S. Kerr, and D. Haughton, "Impact analysis of DERs on bulk power system stability through the parameterization of aggregated DER_a model for real feeders," *Electric Power Systems Research*, vol. 189, p. 106822, 2020.

[21] N. Panigrahy, K. Gopalakrishnan, T. Ilamparithi, and M. Kashinath, "Real-time phasor-EMT hybrid simulation for modern power distribution grids," in *2016 IEEE International Conference on Power Electronics, Drives and Energy Systems (PEDES)*. IEEE, 2016, pp. 1–6.

[22] T. J. Member, S. Xinya, J. Willkomm, S. Schlegel, and D. Westermann, "Hybrids-simulation using EMT-and phasor-based model for converter dominated distribution grid," in *2018 IEEE PES Innovative Smart Grid Technologies Conference Europe (ISGT-Europe)*. IEEE, 2018, pp. 1–6.

[23] C. Zheng, S. Wang, Y. Liu, C. Liu, W. Xie, C. Fang, and S. Liu, "A Novel Equivalent Model of Active Distribution Networks Based on LSTM," *IEEE Transactions on Neural Networks and Learning Systems*, vol. 30, no. 9, pp. 2611–2624, 2019.

[24] J. Stiasny, G. S. Misyris, and S. Chatzivasileiadis, "Physics-Informed Neural Networks for Non-linear System Identification for Power System Dynamics," in *2021 IEEE Madrid PowerTech*, 2021, pp. 1–6.

[25] A. M. Azmy, I. Erlich, and P. Sowa, "Artificial neural network-based dynamic equivalents for distribution systems containing active sources," *IEE Proceedings-Generation, Transmission and Distribution*, vol. 151, no. 6, pp. 681–688, 2004.

[26] G. W. Chang, C.-I. Chen, and Y.-J. Liu, "A neural-network-based method of modeling electric arc furnace load for power engineering study," *IEEE Transactions on Power Systems*, vol. 25, no. 1, pp. 138–146, 2009.

[27] G. Biard and G. Al Nour, "Industry 4.0 Contribution to Asset Management in the Electrical Industry," *Sustainability*, vol. 13, no. 18, 2021.

[28] ARCGIS online. [Online]. Available: https://www.esri.com/en-us/arcgis/products/arcgis-online/overview

[29] GIMBA electric utility asset management software. [Online]. Available: https://gimba.io/electric-utility-asset-management-software/

[30] Mapping and Planning of Electricity Distribution Network. [Online]. Available: https://www.giscloud.com/blog/use-case-mapping-and-planning-of-electric-distribution-network/

[31] Introduction to OpenDSS. [Online]. Available: https://opendss.epri.com/IntroductiontoOpenDSS.html

[32] OpenGridMap. [Online]. Available: https://github.com/opengridmap

[33] CYME power engineering software solutions. [Online]. Available: https://www.eaton.com/us/en-us/digital/brightlayer/brightlayer-utilities-suite/cyme-power-engineering-software-solutions.html

[34] PowerFactory Applications. [Online]. Available: https://www.digsilent.de/en/powerfactory.html

[35] GridLab-D. [Online]. Available: https://www.gridlabd.org/

[36] Asset Tiger. [Online]. Available: https://www.assettiger.com/

[37] Asset Management System with QR Codes. [Online]. Available: https://www.smartsheet.com/marketplace/apps/asset-management-system-qr-codes

[38] Idaho National Laboratory Microgrid Integration. [Online]. Available: https://eps.inl.gov/SitePages/Microgrid%20Integration.aspx

[39] Flutter - Build apps for any screen. [Online]. Available: https://flutter.dev/

[40] Google Android. [Online]. Available: https://www.android.com/

[41] iPhone Operating System. [Online]. Available: https://en.wikipedia.org/wiki/IOS

[42] Apple. [Online]. Available: https://www.apple.com/

[43] MySQL Database. [Online]. Available: https://www.mysql.com/

[44] Amazon Web Services. [Online]. Available: https://aws.amazon.com/

[45] AWS SDK for Python. [Online]. Available: https://aws.amazon.com/sdk-for-python/

[46] List of HTTP status codes. [Online]. Available: https://en.wikipedia.org/wiki/List_of_HTTP_status_codes

[47] A. R. Ramapuram Matavalam, R. Venkatraman, and V. Ajjarapu, "Accurate representation of distribution system dynamics in bulk system studies by clusters of composite load models," in *2023 IEEE Industry Applications Society Annual Meeting (IAS)*, pp. 1–5, ISSN: 2576-702X. [Online]. Available: https://ieeexplore.ieee.org/document/10406803

[48] M. S. Salunke, R. S. Karnik, A. B. Raju, and V. N. Gaitonde, "Analysis of transmission system stability with distribution generation supplying induction motor loads," vol. 12, no. 1, p. 148, number: 1 Publisher: Multidisciplinary Digital Publishing Institute. [Online]. Available: https://www.mdpi.com/2227-7390/12/1/148

[49] Q. Huang and V. Vittal, "Application of electromagnetic transient-transient stability hybrid simulation to FIDVR study," vol. 31, no. 4, pp. 2634–2646, conference Name: IEEE Transactions on Power Systems. [Online]. Available: https://ieeexplore.ieee.org/document/7279209

[50] D. Ramasubramanian, P. Mitra, P. Dattaray, M. Bello, J. C. Boemer, and A. Gaikwad, "Analyzing impact of DER on FIDVR - comparison of EMT simulation of a combined transmission and distribution grid with aggregated positive sequence models," vol. 201, p. 107534. [Online]. Available: https://www.sciencedirect.com/science/article/pii/S0378779621005150

[51] WECC distributed and small PV plants generic model (PVD1). [Online]. Available: https://www.esig.energy/wiki-main-page/wecc-distributed-and-small-pv-plants-generic-model-pvd1/

[52] H. Jain, K. Rahimi, A. Tbaileh, R. P. Broadwater, A. K. Jain, and M. Dilek, "Integrated transmission & distribution system modeling and analysis: Need & advantages," in *2016 IEEE Power and Energy Society General Meeting (PESGM)*, pp. 1–5, ISSN: 1944-9933. [Online]. Available: https://ieeexplore.ieee.org/abstract/document/7741235?casa_token=YK4BZezwuLQAAAAA:dZyf0tMKo7RcyP5befjtJUZEu0YDvdyD4nMu-cjoIPFYX8cESBzmavftZzj4VYAk7_aGvZT3

[53] NERC, "Reliability guideline: Parameterization of the der_a model," September 2019.

[54] FERC opens wholesale markets to distributed resources: Landmark action breaks down barriers to emerging technologies, boosts competition | federal energy regulatory commission. [Online]. Available: https://www.ferc.gov/news-events/news/ferc-opens-wholesale-markets-distributed-resources-landmark-action-breaks-down

[55] Distributed energy resources-technical considerations for the bulk power system (docket nos. RM18-9-000, AD18-10-000) (washington, DC) (free web cast) | federal energy regulatory commission. [Online]. Available: https://www.ferc.gov/news-events/events/distributed-energy-resources-technical-considerations-bulk-power-system-docket